Black Hole-Neutron Star Mergers –Universal Evolution Picture Obtained by Seconds-long Numerical-Relativistic Neutrino-Radiation Magnetohydrodynamics Simulation–

Kota Hayashi

February 6, 2023

Abstract

Black hole-neutron star mergers are one of the main targets of ground-based gravitational wave detectors, and two events GW200105 and GW200115 were detected in 2020. Unlike the binary neutron star merger event GW170817, no electromagnetic counterparts were detected in these events because the binary parameters were in the range that the neutron star does not experience disruption by the tidal force of the companion black hole before the merger. However, depending on the parameters of the binary, the neutron star could be tidally disrupted, leading to mass ejections and the formation of the accretion disk around the remaining black hole. In such a case there is a high expectation for the electromagnetic counterparts to be detected. In the neutron-rich ejected matter, r-process nucleosynthesis synthesizes the heavy radioactive elements. Radioactive decay of such elements generates thermal energy and the ejecta shines as kilonovae. If the remaining system after the merger is a highly magnetized accretion disk surrounding a rapidly rotating black hole, the magnetically driven ultrarelativistic jet could be launched and drive short-hard gamma-ray bursts.

Black hole-neutron star mergers are expected to be a promising source for multi-messenger astronomy. In order to analyze the observational signals and extract scientific information on the merger events, creating the theoretical evolution model of the system is essential. Based on this motivation, we performed numerical-relativity simulations of seconds-long black hole-neutron star mergers incorporating neutrino-radiation transport and magnetohydrodynamics and obtained a self-consistent evolution picture of the inspiral, merger, and post-merger stages. In addition, we also performed simulations for various initial and computational setups and found that the obtained evolution picture is qualitatively universal irrespective of the setups.

The universal evolution processes of the black hole-neutron star merger and the subsequent black hole-accretion disk system are as follows: As the tidal force of the black hole exceeds the self-gravitating force of the neutron star, the neutron star is tidally disrupted; Then the dynamical mass ejection and the formation of the accretion disk take place within the timescale of $\sim 10\,$ms; The dynamical ejecta has an electron fraction lower than 0.1 and a velocity up to $\sim 0.4c$; Subsequently, the magnetic field in the accretion disk is amplified by the magnetic winding, Kelvin-Helmholtz instability, and magnetorotational instability, which induce the turbulent state and enhance the turbulent effective viscosity which results in the angular momentum transport; The combination of the above magnetohydrodynamics effects and magnetic buoyancy activate the MRI dynamo; The post-merger mass ejection driven by the magnetically-induced viscous heating sets in at ~ 300–$500\,$ms after the merger as the maximum temperature of the disk drops below $\sim 3\,$MeV and neutrino luminosity drops below $\sim 10^{51}$–$10^{51.5}\,$erg/s, and continues for several hundred ms; The post-merger ejecta has mildly-neutron rich properties with electron fraction ranging from 0.1 to 0.4 and a velocity lower than $0.1c$; If one end of the magnetic field line falls into the black hole by accretion and the other end ascends from the disk by magnetic buoyancy,

the magnetosphere along the black hole rotation axis is developed by the magnetic tower effect; The magnetosphere is collimated with an opening angle of $\lesssim 10^\circ$ by the funnel wall supported by the geometrically-thick accretion disk, and the strong Poynting flux with the typical maximum isotropic-equivalent luminosity of $\sim 3 \times 10^{49}$–$10^{50}\,\mathrm{erg/s}$ is generated; Then the Poynting flux starts to decrease after ~ 0.5–$2\,\mathrm{s}$. We found three possible mechanisms that terminate the strong Poynting-luminosity stage. One is the widening in the opening angle of the magnetosphere due to the post-merger mass ejection. Another is the polarity flip of the magnetic field in the magnetosphere, which is caused by the dynamo activity. The last is the tilt of the disk and the magnetosphere induced by the anisotropic post-merger ejection. Despite the difference in those mechanisms, what they have in common is that the evolution of the accretion disk determines the evolution of the magnetosphere and determines the timescale of the strong Poynting-luminosity stage.

Publication List

Published Paper Related to this Thesis

- Kota Hayashi, Sho Fujibayashi, Kenta Kiuchi, Koutarou Kyutoku, Yuichiro Sekiguchi, Masaru Shibata,
"General-relativistic neutrino-radiation magnetohydrodynamic simulation of seconds-long black hole-neutron star mergers",
Physical Review. D **106**, 023008 (2022)

Unpublished Paper Related to this Thesis

- Kota Hayashi, Kenta Kiuchi, Koutarou Kyutoku, Yuichiro Sekiguchi, Masaru Shibata,
"General-relativistic neutrino-radiation magnetohydrodynamics simulation of seconds-long black hole-neutron star mergers: Dependence on initial magnetic field strength, configuration, and neutron-star equation of state",
submitted to Physical Review D; arXiv:2211.07158 [astro-ph.HE]

Published Paper not Included in this Thesis

- Kota Hayashi, Kyohei Kawaguchi, Kenta Kiuchi, Koutarou Kyutoku and Masaru Shibata,
"Properties of the remnant disk and the dynamical ejecta produced in low-mass black hole-neutron star mergers",
Physical Review D **103**, 043007 (2021)
- Koutarou Kyutoku, Sho Fujibayashi, Kota Hayashi, Kyohei Kawaguchi, Kenta Kiuchi, Masaru Shibata, Masaomi Tanaka,
"On the Possibility of GW190425 Being a Black Hole-Neutron Star Binary Merger",
The Astrophysical Journal Letters, **890**, L4 (2020)
- Reetika Dudi, Ananya Adhikari, Bernd Brügman, Tim Dietrich, Kota Hayashi, Kyohei Kawaguchi, Kenta Kiuchi, Koutarou Kyutoku, Masaru Shibata, Wolfgang Tichy,
"Investigating GW190425 with numerical-relativity simulations",
Physical Review D, **106**, 084039 (2022)

Unpublished Paper not Included in this Thesis

- Kenta Kiuchi, Sho Fujibayashi, Kota Hayashi, Koutarou Kyutoku, Yuichiro Sekiguchi, and Masaru Shibata,

"Self-consistent picture of the mass ejection from a one second-long binary neutron star merger leaving a short-lived remnant in general-relativistic neutrino-radiation magnetohydrodynamic simulation",
submitted to Physical Review Letters; arXiv:2211.07637 [astro-ph.HE]

- Shinya Wanajo, Sho Fujibayashi, Kota Hayashi, Kenta Kiuchi, Yuichiro Sekiguchi, and Masaru Shibata,
"Actinide-boosting r Process in Black Hole–Neutron Star Merger Ejecta",
submitted to Physical Review Letters; arXiv:2212.04507 [astro-ph.HE]

Contents

Chapter 1

Introduction

The first direct detection of gravitational waves from a binary black hole merger, referred to as GW150914 [1], opened the era of gravitational-wave astronomy. To date, advanced LIGO and advanced Virgo have observed ~ 80 binary black hole merger events [2, 3]. Several neutron-star merger events have also been observed in addition to the binary black hole mergers. A remarkable event is GW170817 [4], the first binary neutron star merger event. Associated with this event, a wide variety of electromagnetic counterparts such as kilonova and short-hard gamma-ray burst were successfully observed [5, 6], and provided us with invaluable information for understanding the processes of the neutron-star merger and its post-merger evolution. The electromagnetic observations also opened the era of multi-messenger astronomy including gravitational-wave observation.

In the latest observational run (O3b), gravitational waves from black hole-neutron star binaries, referred to as GW200105 and GW200115 [7], were observed.[1] Figure 1.1 shows the probability distribution of the component masses. These events surely indicate that black hole-neutron star binaries exist in nature. Although no electromagnetic counterpart is observed for them, it is natural to expect that electromagnetic counterparts will be observed in future events, if the binary parameters are suitable for inducing tidal disruption of neutron stars. A number of numerical-relativity simulations for black hole-neutron star binaries predict that the neutron star could be disrupted by the tidal force of the companion black hole if the black-hole mass is relatively small and/or the black-hole spin is high (e.g., Refs. [8, 9]). The tidal disruption is accompanied by disk formation and mass ejection, which will result in the r-process nucleosynthesis for synthesizing heavy neutron-rich elements [10, 11]. Powered by thermal energy generated by the radioactive decay of synthesized heavy neutron-rich elements, the ejecta will shine with high luminosity as kilonovae [12, 13]. Kilonovae are expected to be a promising electromagnetic counterpart of gravitational-wave events to make follow-up observations. This is because the velocity of the ejecta is shown to be subrelativistic by numerical simulations, and the emission would be quasi-isotropic. The time scale of the emission is expected to be 1–10 days, and it may be suitable for making associations with detection. Also, most of its emission is expected to be around optical and near-infrared, and thus the existing optical telescopes could be used for the follow-up observation. If the remnant black hole is rapidly spinning and surrounded by a massive magnetized disk or torus, an ultra-relativistic jet could be launched and drive a short-hard gamma-ray burst [11, 14, 15]. The short-hard gamma-ray burst is the brightest transient in the universe with its typical maximum isotropic-equivalent luminosity of $\sim 10^{50}$–$10^{52}\,\mathrm{erg/s}$ in the gamma-ray and its time scale of $\lesssim 2\,\mathrm{s}$.

[1] We note that for the event GW200105, a probability of astrophysical origin is less than 0.5 and treated as a marginal candidate in Ref. [3].

The highly relativistic jet with Lorentz factor larger than ~ 30 and its collimation of $\sim 10^\circ$ is thought to power the short-hard gamma-ray burst. Ref. [16] proposed that the black hole-accretion disk system formed after the merger of the black hole-neutron star binary and the binary neutron star could be the progenitor.

The sensitivity of the gravitational-wave detectors is being improved for the forthcoming observational runs (O4 and O5) [17]. Also, large-scale telescopes such as JWST and Vera Rubin telescopes will be in operation during such runs [18, 19]. It is quite natural to expect simultaneous detection of gravitational waves and electromagnetic counterparts from black hole-neutron star mergers if the source is within a distance of several hundred Mpc from the earth. This implies that black hole-neutron star mergers are among the most promising sources for multi-messenger astronomy in the near future. In view of this situation, it is urgent to theoretically develop the entire evolution scenario from the merger to the post-merger stages, in order to predict observable signals and to make a reliable model for the interpretation of the forthcoming observational data.

In the last 16 years, a variety of numerical-relativity simulations for black hole-neutron star mergers have been performed [20–55]. By improving the input physics and grid resolution, the previous studies have extensively explored the process of the tidal disruption, accretion disk formation, dynamical mass ejection, gravitational-wave emission, and neutrino emission. However, most of the previous works have focused only on the evolution from the inspiral to early post-merger stages; the evolution was followed at longest for a few hundred ms after the merger. Hence, the long-term seconds-long evolution of the system has not been explored deeply. In order to compensate for this deficiency, i.e., to explore the entire post-merger evolution processes, many long-term numerical simulations for black hole-accretion disk systems have also been performed, including viscous hydrodynamics or magnetohydrodynamics effects [56–71]. These simulations have qualitatively clarified the evolution processes in the post-merger stage such as the post-merger mass ejection and jet launch. For example, it is now widely accepted that the post-merger mass ejection is likely to be driven by an effective viscous effect induced by the magnetohydrodynamics turbulence. The jet outflow is also likely to be powered by the Blandford-Znajek mechanism [72] by magnetic fields penetrating a rapidly spinning black hole. However, it is not clear whether the initial condition given in such simulations are appropriate for exploring the post-merger evolution of the black hole-neutron star merger. During the merger stage, the neutron-star matter is spread non-axisymmetrically around the remnant black hole, and the non-axisymmetric fall-back matter suppresses the system from being axisymmetric. Such non-axisymmetrical structure of the accretion disk could also have a significant effect on the magnetic field amplification and its structure. Therefore, the quantitative details of the post-merger process are yet to be discovered.

In order to acquire the full understanding of the black hole-neutron star mergers and associated mass ejection processes, we need to perform a self-consistent simulation starting from an inspiral stage throughout the post-merger stage. Specifically, the post-merger evolution has to be followed at least for a few seconds, because the post-merger mass ejection takes place spending the timescale of $\gtrsim 1\,\mathrm{s}$. Furthermore, to explore the generation mechanism of short-hard gamma-ray bursts, a simulation with the duration of $\gtrsim 1$ s is needed because their typical duration is $\sim 1\,\mathrm{s}$ with the longest duration of $\sim 2\,\mathrm{s}$ [14, 15]. Keeping in mind these timescales, in this thesis, we tackle this problem by performing numerical-relativity simulations of black hole-neutron star mergers incorporated with neutrino-radiation and magnetohydrodynamics for $\approx$ 1–6 s. We performed a total of eleven simulations in different setups. We adopt two different grid resolutions to find out the convergence of the simulation. We also adopt three different initial magnetic field

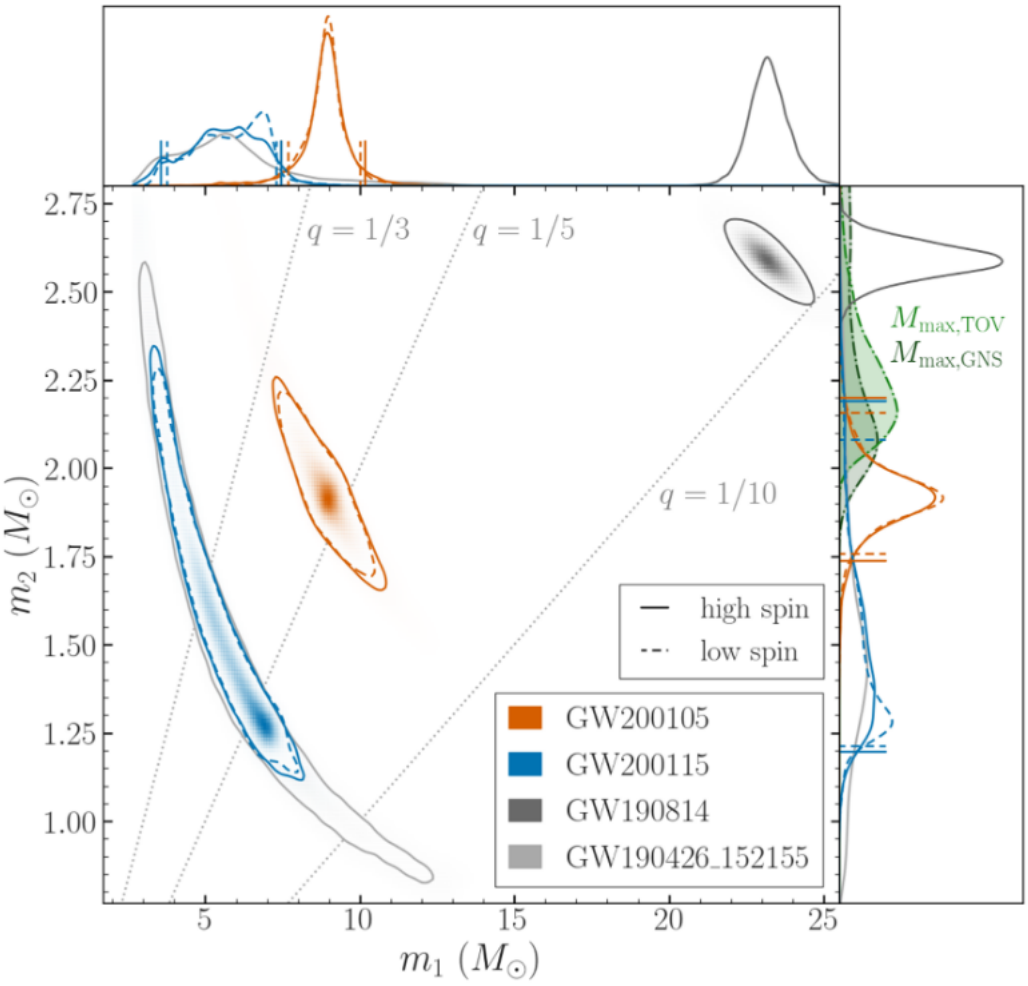

Figure 1.1: Probability distribution of the component masses for the gravitational wave events GW200105 (orange) and GW200115 (blue). The Colored shading and solid curves indicate the results with the high-spin prior, while the dashed curves represent those with the low-spin prior. The results for event GW190814 and the marginal candidate GW190426_152155 are also shown in gray. This figure is taken from Ref. [7]

amplitudes confined in the neutron star ranging over an order of magnitude, in order to clarify whether, at least qualitatively, the universal evolution picture is obtained. The dependence on the initial magnetic field configuration is explored by adopting the poloidal and toroidal magnetic fields in the neutron star. We also perform several simulations to find out the dependence on the binary parameters; We adopt two different mass ratios and two different equations of state. And finally, we investigate the influence of the presence or absence of equatorial symmetry on the evolution of the system.

The thesis is organized as follows. In Chapter 2, we review the evolution picture of the black hole-neutron star merger discovered by the previous studies. In Chapter 3, we describe the formulation and the computational method of the numerical-relativistic neutrino-radiation magnetohydrodynamics simulation. In Chapter 4, we show the result of the simulations that focused mainly on the dependence on binary mass-ratio and grid resolution. In Chapter 5, we show the result of the simulations that focused mainly on the dependence on initial magnetic field strength, configuration, neutron-star equation of state, and equatorial-plane symmetry. Finally, we summarize this thesis in Chapter 6. Throughout this thesis, we use the geometrical units in which $G = c = 1$, where G and c are the gravitational constant and the speed of light, respectively.

Chapter 2

Black hole-neutron star merger: A review

Black hole-neutron star binaries are one of the most promising targets of the ground-based gravitational-wave detectors, and indeed the gravitational wave events GW200105 and GW200115, whose sources are considered to be black hole-neutron star mergers, are detected [7]. Also, black hole-neutron star binaries could play a major role in elucidating several unsolved problems. First, the gravitational wave from binaries carries information about the neutron star such as its mass and radius. It can be used to constrain the equation of state (EOS) of the high-density neutron star matter. Second, the merger could be the origin of the heavy elements. During the merger and the post-merger stage, the system could eject neutron-rich matter, and r-process nucleosynthesis proceeds in the ejecta. The synthesized r-process heavy elements could be a fraction to explain the heavy element abundance of the solar system. Third, the black hole-accretion disk system formed after the merger could be the origin of the short-hard gamma-ray burst. If a short-hard gamma-ray burst is simultaneously detected with a gravitational wave event, its origin may be confirmed to be the merger. In addition, we may be able to model the central engine of the short-hard gamma-ray burst by modeling the merger and the post-merger evolution processes.

In the binary, a black hole and a neutron star are inspiraling around each other, and due to the gravitational wave emission, the binary loses energy and angular momentum. As a result, the orbiting radius decreases eventually leading to the merger. In this chapter, we review the previous studies on the black hole neutron star merger. We review the mass-shedding limit mainly based on the analytical approach, which can approximately estimate how the merger proceeds depending on the parameters of the binary [73]. And then, we review the various studies based on numerical simulations that focused on the merger and the post-merger stages.

2.1 Tidal disruption and merger stage

The fate of the black hole-neutron star binary is roughly divided into two cases. One case is the "plunge", in which almost all the neutron star matter falls into the black hole during the merger stage. In this case, there is no significant mass ejection or accretion disk formation. Therefore, the remaining system after the merger is only a stationary black hole. The electromagnetic counterparts are not expected in this case. The other case is the "tidal disruption", in which the neutron star is tidally disrupted by the black hole before the merger. In this case, there could be a mass ejection or an accretion disk

formation, and they could power electromagnetic counterparts such as kilonova/macronova and short-hard gamma-ray bursts during the post-merger stage.

During the late-inspiral stage to the merger stage of the black hole-neutron star merger, the neutron star could be disrupted by the tidal force of the black hole. This is the phenomenon called tidal disruption, which occurs when the tidal force of the black hole exceeds the self-gravitating force of the neutron star and the neutron star could not maintain its structure. The condition for the tidal disruption to occur depends on the mass ratio of the black hole and the neutron star, the black-hole spin, and the neutron-star compactness. Here we discuss the condition for the tidal disruption based on Ref. [73]. The mass-shedding limit is a necessary condition for the tidal disruption. It is the limit for the neutron star matter to be stripped away from its surface due to the tidal force of the black hole. Based on Newtonian gravity, it is written as

$$2\frac{M_{\rm BH}\left(c_R R_{\rm NS}\right)}{r^3} > \frac{M_{\rm NS}}{\left(c_R R_{\rm NS}\right)^2}, \tag{2.1}$$

where $M_{\rm BH}$, $M_{\rm NS}$, $R_{\rm NS}$, and r show the black hole mass, the neutron star mass, the neutron star radius, and the binary separation. $c_R \sim O(1)$ shows the contribution from the tidal deformation of the neutron star. This can be rewritten as a condition for orbital frequency as

$$\begin{aligned} M_{\rm tot}\Omega &= M_{\rm tot}\sqrt{\frac{M_{\rm tot}}{r^3}} \\ &> c_R^{-3/2}\mathcal{C}^{3/2}(1+Q)(1+Q^{-1})^{1/2}, \end{aligned} \tag{2.2}$$

where $M_{\rm tot} = M_{\rm BH} + M_{\rm NS}$ is the total mass of the system and $Q = M_{\rm BH}/M_{\rm NS}$ is the mass ratio. $\mathcal{C}$ is the compactness of the neutron star defined by $\mathcal{C} = M_{\rm NS}/R_{\rm NS}$. In order to have the matter remaining outside the remnant black hole after the merger, the neutron star has to be tidally disrupted outside the innermost stable circular orbit (ISCO) of the black hole. By considering this situation the condition is written as

$$M_{\rm tot}\Omega_{\rm ISCO} > c_R^{-3/2}\mathcal{C}^{3/2}(1+Q)(1+Q^{-1})^{1/2} \tag{2.3}$$

where $\Omega_{\rm ISCO}$ is the orbital angular frequency at the ISCO. $\Omega_{\rm ISCO}$ depends on the black-hole spin $\chi_{\rm BH}$, and as $\chi_{\rm BH}$ becomes large $\Omega_{\rm ISCO}$ can become large. This condition shows that the tidal disruption is likely to occur when

- the compactness of the neutron star $\mathcal{C}$ is small.
- the mass ratio of the binary Q is small.
- the black-hole spin $\chi_{\rm BH}$ is large.

Precise and realistic conditions are obtained only by numerical relativity simulations. Ref. [74] derived a fitting formula for $\Omega_{\rm ISCO}$ in the assumption of a non-spinning black hole, and a value of c_R for polytropic neutron-star EOS. Then they obtained the following condition:

$$0.270\mathcal{C}^{3/2}(1+Q)\left(1+Q^{-1}\right)^{1/2} < 0.0680\left[1-\frac{0.444}{Q^{0.25}}\left(1-3.54\mathcal{C}^{1/3}\right)\right]. \tag{2.4}$$

Also, the full numerical relativity simulations focusing on the inspiral stage to the merger stage were performed [20–26, 29–31, 35–37, 42, 51]. In these works, they found not

only whether the neutron star experiences the tidal disruption, but also the disk mass and the ejecta mass. In these simulations, they solved the time evolution of the gravitational field and hydrodynamics for various initial binary parameters. As a result, they found the qualitative conditions for the tidal disruption. The mass of the matter remaining outside the apparent horizon after the merger is used to determine whether the tidal disruption occurred or not. Figure 2.1 summarizes the conditions of the tidal disruption depending on the binary mass ratio, the neutron-star compactness, and the black-hole dimensionless spin parameter [8]. The qualitative dependence on those parameters is consistent with the analytical discussion on the mass-shedding limit and ISCO above.

They also evaluated the mass of the dynamical ejecta, which is the unbound matter dynamically ejected by the tidal force during the merger for the cases with tidal disruption. The dependence of the ejecta mass on binary parameters is consistent with the condition of tidal disruption. The mass of the dynamical ejecta is at most $\sim 0.1 M_\odot$ and its averaged velocity is subrelativistic with ~ 0.2–$0.3c$. The dynamical mass ejection is driven primarily by tidal force and its morphology is anisotropic; The dynamical ejecta concentrate around the orbital plane, and often have a crescent-like shape when its mass is large. We note, however, that for the binaries with the near-equal-mass regime, the dynamical ejecta mass decreases as the mass ratio Q decreases [49, 51].

Another important aspect of these numerical relativity simulations was to obtain gravitational waveforms. The waveforms obtained in the simulations are used to create templates that play an essential role in gravitational-wave detection. Figures. 2.2 and 2.3 show the gravitational waveforms and gravitational-wave spectra from black hole-neutron star mergers. The figures are taken from Ref. [30]. The models adopted in this example are $Q = 4$, $M_{\rm NS} = 1.35 M_\odot$, and $\chi_{\rm BH} = 0.75$. The neutron star is modeled by the EOS called 2H, H, HB, and B, where its radius is 15.53, 12.27, 11.61, and 10.96 km respectively. All the models show a similar chirp waveform during the inspiral stage. For the model with the largest compactness (labeled with B-Q4M135a75), tidal disruption does not occur. In this case, the neutron star is not tidally disrupted and swallowed by the black hole. Therefore, the quasi-normal modes of the remnant black hole are excited and ring-down gravitational waves are emitted. However, for the model with the smallest compactness (labeled with 2H-Q4M135a75), tidal disruption takes place. In this case, the chirp waveform is truncated at the disruption, and ring-down is not observed. This is because, as the neutron star is tidally disrupted, the neutron star matter spreads around the black hole and the system no longer behaves as a binary. After the tidal disruption, the matter forms the accretion disk around the remnant black hole, and the matter accretion onto the black hole proceeds, but the accretion is relatively axisymmetric and thus the quasi-normal modes of the remnant black hole are not excited. The existence of the tidal disruption can also be seen in the spectra of gravitational waves. The spectra in Fig. 2.3 show that the cutoff frequency becomes low as the compactness of the neutron star becomes small. The cutoff frequency in the spectra reflects the frequency at which the gravitational waveform is truncated and is thus related to the orbital frequency at which the tidal disruption occurs. Therefore the cutoff frequency has the information of the neutron-star EOS. If the cutoff frequency is observationally determined then we could impose a new constraint on the EOS.

In addition to the mass ratio, the neutron-star compactness, and the black-hole spin, Ref. [31, 37, 42] also performed numerical-relativity simulations for the case that the black-hole spin is not aligned with the orbital angular momentum of the binary and discussed the dependence on the misalignment. The orbital precessions are seen in these simulations and the tidal disruption is significantly affected by this misalignment. Qualitatively, the

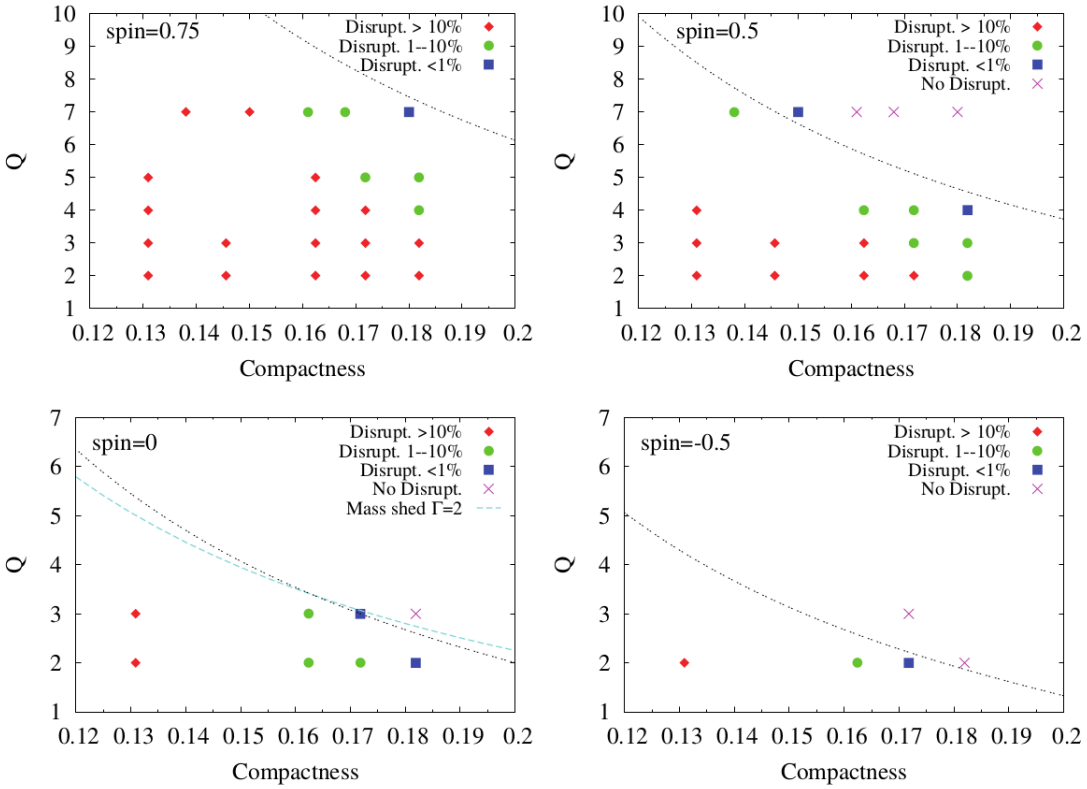

Figure 2.1: The condition of the tidal disruption on the plane of neutron star compact ness $\mathcal{C}$ and mass ratio Q for the black-hole spin 0.75 (top left panel), 0.5 (top right panel), 0.0 (bottom left panel), and -0.5 (bottom right panel), respectively. We note that the black-hole spin is aligned (positive value) or antialigned (negative value) with the orbital axis. The diamond, circle, and square show the models whose rest mass of the matter remaining outside the apparent horizon is > 10 %, 1–10 %, and < 1 % of the total rest mass before the merger. These models are the cases in which the tidal disruption occurs, while the models shown by crosses are the cases in which the tidal disruption does not occur and the remnant mass is less than 0.1 % of the total rest mass. This figure is taken from Ref. [8]

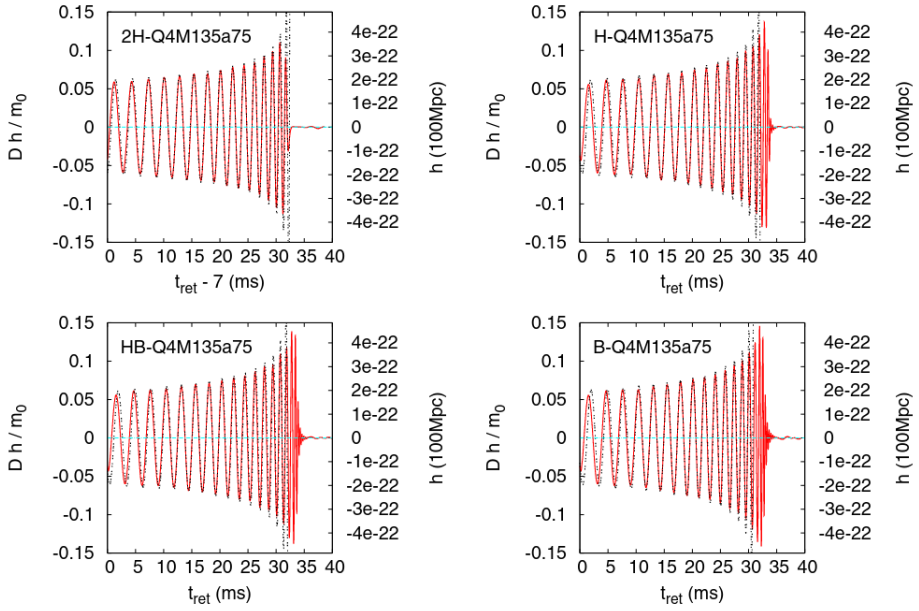

Figure 2.2: Gravitational waveforms for the model with binary parameter $Q = 4$, $M_{\rm NS} = 1.35 M_\odot$, and $\chi_{\rm BH} = 0.75$. The EOSs adopted are 2H, H, HB, and B, where a neutron star with 2H has the smallest compactness (the largest radius) while a neutron star with B has the largest compactness (the smallest radius). The waveforms are shown for an observer located along the axis of rotation and plotted as a function of a retarded time. This figure is taken from Ref. [30]

tidal disruption is suppressed and the rest mass of the matter remaining outside the black hole after the merger monotonically decreases as the misalignment angle increases.

2.2 Post-merger stage

The numerical-relativity simulations for the black hole-neutron star mergers mentioned in the previous section were done by solving the evolution of the gravitational field and hydrodynamics. Such simulations focused mainly on the inspiral to the merger stage. What they found in those simulations were gravitational waveforms, the mass and the spin of the remnant black hole, the disk mass, and the mass of the dynamical ejecta. However, such numerical simulations are not sufficient to understand the evolution of the system after the merger in the presence of tidal disruption. Magnetohydrodynamics, neutrino-radiation transport, and microphysics are other essential factors for the post-merger evolution. Various numerical-relativity simulations were done by improving such input physics step by step. Note, that the inspiral and the merger process do not significantly change even in the presence of improved physics for the realistic initial setup.

Some works took into account nuclear-theory-based neutron-star EOSs [28, 35, 36, 39, 40, 42–46, 48–50], neutrino cooling [39, 40, 44–46, 49, 50], and neutrino heating [45]. In these simulations they discovered that the hot accretion disk with its typical temperature of ~ 10 MeV is formed shortly after the tidal disruption and emits neutrinos with the peak total luminosity $\sim 10^{53}$ erg/s. Also, they found the chemical composition of the dynamical ejecta should be very neutron-rich because it is ejected mainly by the tidal force and does

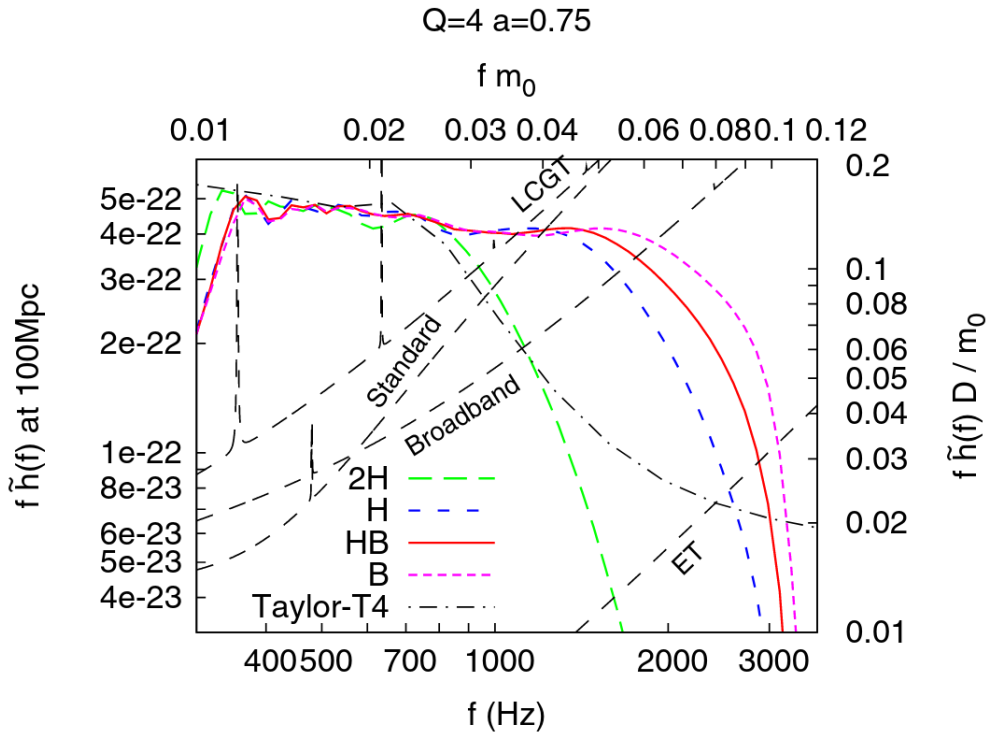

Figure 2.3: Gravitational-wave spectra for the model with binary parameter $Q = 4$, $M_{\rm NS} = 1.35 M_\odot$, and $\chi_{\rm BH} = 0.75$. The EOSs adopted are 2H, H, HB, and B. This figure is taken from Ref. [30]

not experience thermal processes, such as shock heating, significantly. Therefore, the chemical composition of the dynamical ejecta does not change from the neutrinoless *beta*-equilibrium value at zero temperature of the initial neutron star. We note that they did not find the neutrino-driven mass ejection from the remnant disk.

Other works took into account the effect of the magnetic field [27, 33, 34, 41, 43, 47]. Ref. [43] performed high-resolution numerical-relativity simulation for the merger of a black hole-magnetized neutron star binary. The poloidal magnetic field confined in the neutron star with its maximum field strength of 10^{15} G is assumed for the initial condition. The amplitude is chosen so that the wavelength of the fastest growing mode of the non-axisymmetric magnetorotational instability is sufficiently resolved for the remnant disk. Figure 2.4 shows the two-dimensional snapshots on the meridional plane. They showed that due to the magnetorotational instability [75, 76], the turbulent state is established in the accretion disk formed after the tidal disruption. Then, the turbulence viscosity drives the mass accretion and converts the accretion energy to thermal energy. As a result, thermally driven post-merger ejection is launched in the form of disk wind at ~ 10 ms after the merger. In addition, they found the Poynting luminosity driven by the Blandford-Znajek mechanism [72] is as high as $\sim 10^{50}$ erg/s on the apparent horizon. The luminosity is consistent with typical short-hard gamma-ray bursts, but the magnetic pressure could not completely dominate over the gas pressure and neither the aligned global magnetic field nor the jet-like collimated outflow was observed in this work.

On the other hand, Refs. [41, 47] showed that a mildly relativistic collimated outflow could be launched after the merger if the neutron star is endowed with a dipole magnetic field that extends from the interior to the exterior of the neutron star. The black hole with its dimensionless spin parameter larger than 0.5 was also required. In addition, the dipole magnetic field is needed to be aligned to the black-hole spin for the launch of the outflow. Figure 2.5 shows the three-dimensional snapshots obtained in Ref. [47]. In these simulations, the magnetically dominated area extends from the region near the black hole to the direction of the rotational axis of the black hole. The Poynting flux generated by the Blandford-Znajek mechanism is transported outward in this area, and the outflow is launched as the flux is transformed into the kinetic energy of the fluid. The Poynting flux evaluated at ~ 500 km from the black hole is $\sim 10^{51}$ erg/s, which is also consistent with the luminosity of short-hard gamma-ray bursts. We note, however, that the initial dipolar magnetic field assumed in these simulations was $\sim 6 \times 10^{15}$ G on the surface of the neutron star and maximum of $\sim 10^{17}$ G inside the neutron star. This leads to the formation of the global magnetic field penetrating the remnant black hole with its amplitude $\gtrsim 10^{15}$ G near the surface right after the merger. It is not clear whether such a strong global magnetic field penetrating the remnant black hole could be formed in the realistic case for which a dipolar magnetic field has its field strength weaker than $\sim 10^{12}$ G initially.

Ref. [55] is the first study that performed the numerical-relativity simulation for the black hole-neutron star mergers incorporating magnetohydrodynamics and neutrino-radiation transport. Nearly equal-mass black hole-neutron star mergers with confined initial poloidal magnetic fields were simulated for 350 ms after the merger. They focused on giving an analysis of the fluid and the magnetic-field properties of accretion disks, while they did not find post-merger mass ejection nor the magnetically driven outflow. In comparison with Ref. [43], this work implied that disk cooling by neutrino radiation plays a role in delaying or suppressing the post-merger mass ejection. Although they did not observe the launching of a jet, they did find that the region with low-plasma β is gradually expanding from the region near the black hole to the direction of the black-hole spin. Including Ref. [55], all of the numerical simulations of black hole-neutron star

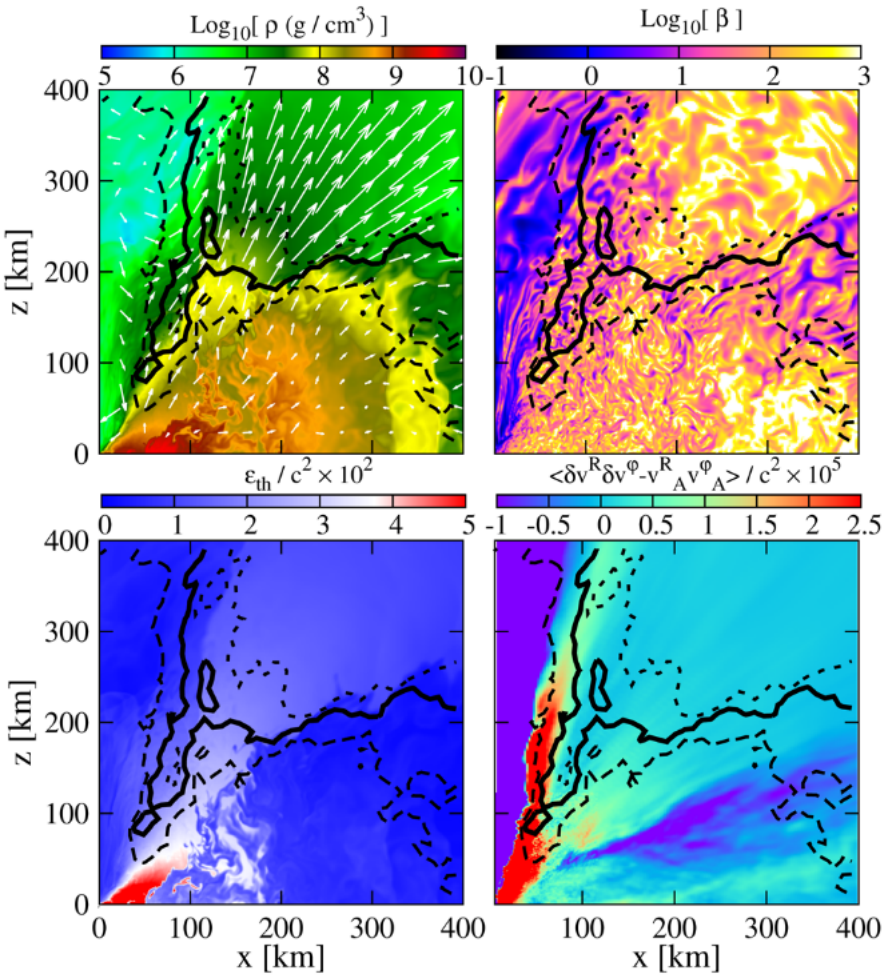

Figure 2.4: Snapshots of rest-mass density with velocity fields (top left panel), plasma β (top right panel), the thermal component of specific internal energy (bottom left panel), and the sum of the Maxwell and Reynolds stress (bottom right panel) on the meridional plane. Black lines in all panels are the boundaries between bound and unbound matter. This figure is taken from Ref. [43].

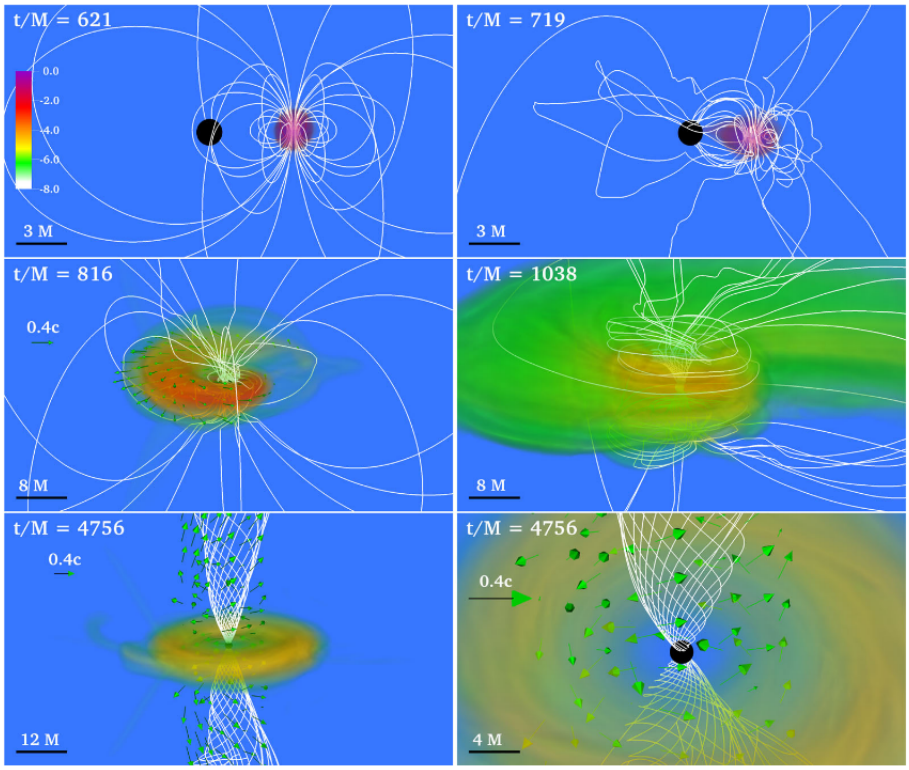

Figure 2.5: Three-dimensional snapshots of rest-mass density (volume rendering), magnetic field line (white lines), and the fluid velocity (green arrows) for the model with neutron star endowed with the global dipolar magnetic field initially. The apparent horizon is shown as a black sphere. Here, $M = 2.5 \times 10^{-2}\,\mathrm{ms} = 7.58\,\mathrm{km}$. This figure is taken from Ref. [47].

merger focused only on the early post-merger stage and evolved the system at most for a few hundred ms. The longer simulation was required to acquire a self-consistent evolution picture of both the post-merger mass ejection and jet-like collimated outflow.

In order to obtain the entire post-merger evolution process, long-term numerical simulations incorporated with viscous hydrodynamics or magnetohydrodynamics effects for black hole-accretion disk systems have also been performed [56–71]. These simulations have qualitatively clarified the evolution processes in the post-merger stage. For example, Refs. [66, 67, 70] performed numerical-relativity simulation including viscous neutrino-radiation hydrodynamics. They evolved the system for several seconds and found that 10%–30% of the disk mass is ejected as disk wind, which can be understood as post-merger ejecta. In an early phase in which the disk is compact, the temperature of the disk is as high as ~ 5–$10\,\mathrm{Mev}$ due to the viscous heating, and the luminosity of neutrinos emitted from the system are $\sim 10^{53}\,\mathrm{erg/s}$. In such a situation the free energy generated by the viscous heating is consumed by the neutrino emission and cannot be used to drive disk wind in contrast to the result of the simulation only with magnetohydrodynamics in Ref. [43]. However, the disk evolves due to the viscous effect, and the matter located at the inner part of the disk accretes onto the black hole as it loses angular momentum, while the matter located at the outer part of the disk expands as it receives the angular momentum. As the disk expands, the temperature of the disk decreases, and the neutrino luminosity decreases. When the maximum temperature of the disk drops below $\sim 3\,\mathrm{MeV}$ the neutrino emission becomes inefficient and the free energy generated by the viscous heating can then be used for mass ejection. The specific entropy at the inner edge of the disk increases and convective motion is triggered. This convective motion transports the free energy from the inner to the outer part of the disk, and as the matter obtains sufficient energy it becomes unbound and ejected from the system. The typical timescale for this mass ejection is determined by the viscous timescale in the disk as

$$\tau_{\rm vis} \sim \frac{R^2}{\alpha_\nu c_{\rm s} H} \sim 1{\rm s}\left(\frac{\alpha_\nu}{0.05}\right)^{-1}\left(\frac{c_{\rm s}}{0.05c}\right)^{-1}\left(\frac{H}{30{\rm km}}\right)^{-1}\left(\frac{R}{150{\rm km}}\right)^{2}. \tag{2.5}$$

Here, R and H are the radius and the height of the disk, respectively, and $c_{\rm s}$ denotes the sound speed. α_ν is the dimensionless viscous coefficient [77]. They also discovered that the electron fraction or the ratio of electrons to baryons of the ejecta is ≈ 0.30–0.35 typically. They suggest that not heavy r-process elements but light trans-iron elements would be synthesized in the ejected matter.

Refs. [61, 62, 64] performed the general-relativistic neutrino-radiation magnetohydrodynamics simulation for the black hole-accretion disk system. They found the launch of the disk wind powered by magnetohydrodynamical effective viscous heating. The time evolution of this viscous-driven disk wind is consistent with viscous neutrino-radiation hydrodynamics simulations. They also found the launch of the magnetically driven outflow perpendicular to the disk as the system becomes magnetically-arrested disk [78]. In the magnetically-arrested disk, the magnetic field penetrating the black hole becomes dynamically important and obstructs the accretion of the gas from the disk. The magnetic field penetrating a black hole is aligned and extends globally to the direction perpendicular to the disk which forms the magnetically dominated area. The Poynting flux of $\sim 10^{50}$–$10^{51}\,\mathrm{erg/s}$ are generated by the Blandford-Znajek mechanism and transferred outward in the magnetically dominated area. Ref. [64] also showed that the polarity of the magnetic field in the magnetically dominated area could be flipped. They suggested that the MRI dynamo activated in the disk played a role in the polarity flip. MRI dynamo in the black hole-accretion disk is observed in several magnetohydrodynamical simulations [61, 79] as

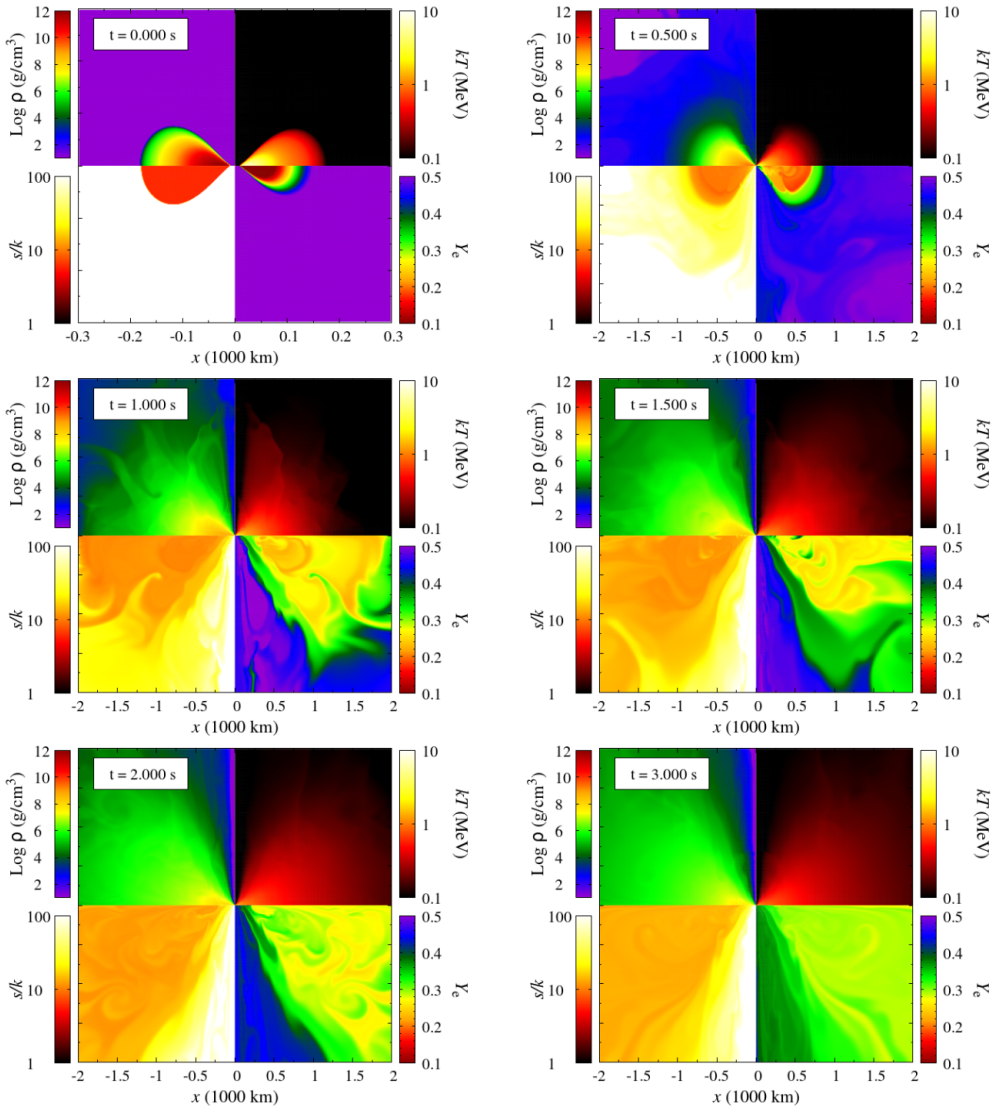

Figure 2.6: Snapshots for the rest-mass density, temperature, specific entropy per baryon, and electron fraction for numerical-relativity simulation of black hole-accretion disk including viscous neutrino-radiation hydrodynamics. This figure is taken from Ref. [66].

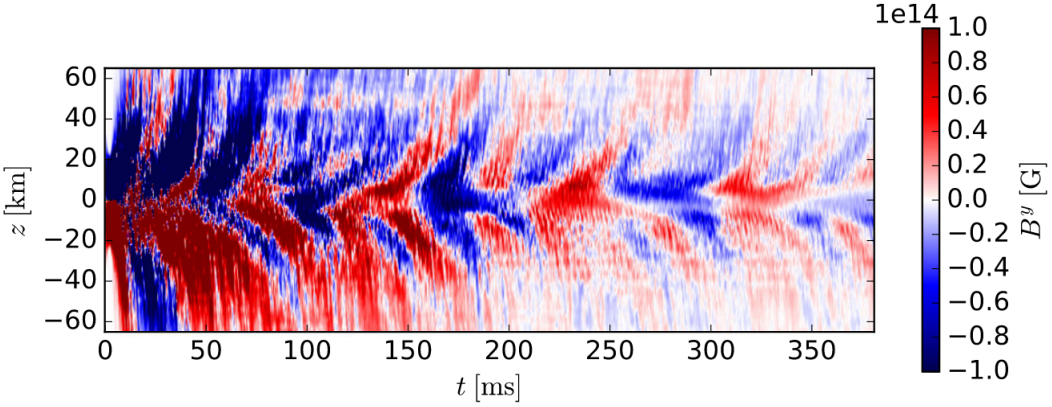

Figure 2.7: The time-toroidal magnetic field diagram for the black hole-accretion disk simulation. This figure is taken from Ref. [61].

the so-called butterfly structure in the time-toroidal magnetic field diagram. Figure 2.7 shows that the polarity of the toroidal magnetic field flips in a quasi-periodic manner and the magnetic field ascends from the equatorial plane to the surface of the accretion disk. MRI dynamo is activated as a result of the combination of several magnetohydrodynamical processes: magnetorotational instability that produces the radial field, magnetic field winding that produces the toroidal field, and magnetic buoyancy that produces the toroidal field.

Those works on simulations for the black hole-accretion disk system have played an important role in understanding the post-merger stage. However, it is not clear whether the initial conditions adopted in those simulations are appropriate for the black hole-neutron star merger case. The merger is a highly non-axisymmetric phenomenon and thus the resulting accretion disk formed after the merger is highly non-axisymmetric. The fall-back matter associated with the failed dynamical ejecta could have a significant effect on the evolution of the disk. The magnetic field properties and configuration in the disk after the merger are also unknown. Non-axisymmetric remnant matter could have a significant effect on the magnetic field amplification and its structure. It is difficult to create initial conditions that reproduce the properties of the accretion disk and its surrounding environment. Therefore the conclusive and quantitative details of the post-merger stage have not been fully understood yet.

Chapter 3

Methods

To acquire full understanding of the evolution picture of the black hole-neutron star merger starting from the inspiral stage throughout the post-merger stage, we solve the evolution of the gravitational field, magnetohydrodynamics, and neutrino-radiation transfer self-consistently. In this chapter, we review the basic equations and numerical schemes implemented in the code which we used in the simulations.

3.1 Einstein's equation

The dynamical evolution of the gravitational field is an essential factor particularly in the inspiral, merger, and early post-merger stages. In such stages, solving Einstein's equation is inevitable for obtaining the accurate evolution of the system. For numerically solving Einstein's equation, we adopt the Baumgarte-Shapiro-Shibata-Nakamura (BSSN) formalism[80–84], incorporating a Z4c-type constraint-propagation prescription [42, 85]. This BSSN formalism is based on the 3+1 decomposition, which decomposes the four-dimensional spacetime into three-dimensional space and one-dimensional time. The dynamical variables for the 3+1 decomposition are the induced metric $\gamma_{\mu\nu}$ and extrinsic curvature $K_{\mu\nu}$ defined as follows.

$$\gamma_{\mu\nu} := g_{\mu\nu} + n_\mu n_\nu, \tag{3.1}$$

$$K_{\mu\nu} := -\gamma^\rho{}_\mu \gamma^\sigma{}_\nu \nabla_\rho n_\sigma = -\frac{1}{2}\mathcal{L}_n \gamma_{\mu\nu}. \tag{3.2}$$

Here, $g_{\mu\nu}$ and n_μ are the four-dimensional spacetime metric and the unit normal vector of the three-dimensional hypersurface parameterized by the time, respectively. ∇_μ and $\mathcal{L}_n$ are the covariant derivative and Lie derivative with respect to unit normal vector n^μ, respectively. The line element is written as

$$ds^2 = -\alpha dt^2 + \gamma_{ij}(dx^i + \beta^i dt)(dx^j + \beta^j dt), \tag{3.3}$$

where α and β^i are the lapse function and the shift vector, respectively. The lapse function and the shift vector are not the dynamical variables of the gravitational field and they describe the gauge degree of freedom. Determining the lapse function corresponds to defining the time slice, and determining the shift vector corresponds to defining the spacial coordinate on the time slice. By considering Einstein's equation, the following constraints

and evolution equations for 3+1 decomposition are obtained.

$$
\begin{aligned}
R - K_{ij}K^{ij} + K^2 &= 16\pi\rho_h, && (3.4)\\
D_jK_i^j - D_iK &= 8\pi J_i, && (3.5)\\
(\partial_t - \beta^k\partial_k)\gamma_{ij} &= 2\alpha K_{ij} + D_i\beta_j + D_j\beta_i && (3.6)\\
(\partial_t - \beta^k\partial_k)K_{ij} &= \alpha R_{ij} - 8\pi\alpha\left[S_{ij} - \frac{1}{2}\gamma_{ij}(S^k{}_k - \rho_h)\right] + \alpha(-2K_{ik}K^k{}_j + KK_{ij})\\
&\quad -D_iD_j\alpha + \beta^kD_kK_{ij} + K_{ik}D_j\beta^k + K_{jk}D_i\beta^k && (3.7)
\end{aligned}
$$

The first and second equations are the Hamiltonian and the momentum constraints, respectively. The third and fourth equations are the evolution equation of the induced metric and the extrinsic curvature. Here, D_i, R_{ij}, and R are the covariant derivative, the Ricci tensor, and the Ricci scalar associated with the induced metric. ρ_h, J_i, and S_{ij} are the projected components of the energy-momentum tensor of matter defined by

$$
\begin{aligned}
T_{\mu\nu} &= \rho_h n_\mu n_\nu + J_\mu n_\nu + J_\nu n_\mu + S_{\mu\nu}, && (3.8)\\
\rho_h &:= T_{\mu\nu}n^\nu n^\mu, && (3.9)\\
J_\mu &:= -T_{\nu\rho}n^\rho\gamma_\mu{}^\nu, && (3.10)\\
S_{\mu\nu} &:= T_{\rho\sigma}\gamma^\rho{}_\mu\gamma^\sigma{}_\nu. && (3.11)
\end{aligned}
$$

Though we obtained the evolution equations for the dynamical variables in 3+1 decomposition formalism, i.e. induced metric and extrinsic curvature, it is known that this formulation is not suitable for numerical simulations because the equations are not strongly hyperbolic. The truncation error is unavoidable due to the discretization of field equations. In this formalism, the error does not propagate away but accumulates locally, and thus calculation becomes numerically unstable. The BSSN formalism is one of the most successful formalism that provides strongly hyperbolic equations and hence can solve Einstein's equation stably [80, 81].

In the BSSN formalism, the dynamical variables are decomposed by conformal decomposition as

$$
\begin{aligned}
\tilde{\gamma}_{ij} &:= W^2\gamma_{ij}, && (3.12)\\
\tilde{A}_{ij} &:= W^2\left(K_{ij} - \frac{1}{3}K\gamma_{ij}\right), && (3.13)\\
W &:= \gamma^{-1/6}, && (3.14)\\
K &:= \gamma^{ij}K_{ij}, && (3.15)
\end{aligned}
$$

where γ is the determinant of γ_{ij}. This decomposition introduces the additional two variables, but it is not the physical freedom and the following two corresponding constraints are introduced:

$$
\begin{aligned}
\tilde{\gamma} &= 1, && (3.16)\\
\tilde{\gamma}^{ij}\tilde{A}_{ij} &= 0. && (3.17)
\end{aligned}
$$

Furthermore, the original BSSN formalism, which we adopt in the present simulations, introduces an auxiliary variable

$$
F_i := \delta^{jk}\partial_k\tilde{\gamma}_{ij} \tag{3.18}
$$

and evolve it as an independent variable [80]. This is the key point in the BSSN formalism and make it possible to solve Einstein's equation stably. Using the conformally decomposed variables and the auxiliary variable, the evolution equations are written as

$$\left(\partial_t - \beta^k\partial_k\right) W = \frac{1}{3}\left(\alpha K - \partial_k\beta^k\right) W, \tag{3.19}$$

$$\left(\partial_t - \beta^k\partial_k\right) \tilde{\gamma}_{ij} = -2\alpha\tilde{A}_{ij} + \tilde{\gamma}_{ik}\partial_j\beta^k + \tilde{\gamma}_{jk}\partial_i\beta^k - \frac{2}{3}\tilde{\gamma}_{ij}\partial_k\beta^k \tag{3.20}$$

$$\left(\partial_t - \beta^k\partial_k\right) K = -D^k D_k\alpha + \alpha\left[\tilde{A}_{ij}\tilde{A}^{ij} + \frac{1}{3}K^2\right] + 4\pi\alpha\left(\rho_h + S\right), \tag{3.21}$$

$$\begin{aligned}\left(\partial_t - \beta^k\partial_k\right) \tilde{A}_{ij} &= \alpha W^2\left(R_{ij} - \frac{1}{3}\tilde{\gamma}_{ij}R\right) - \left(W^2 D_i D_j\alpha - \frac{1}{3}\tilde{\gamma}_{ij}D^k D_k\alpha\right) \\ &\quad +\alpha\left(K\tilde{A}_{ij} - 2\tilde{A}_{ik}\tilde{A}^k_j\right) + \tilde{A}_{ik}\partial_j\beta^k + \tilde{A}_{jk}\partial_i\beta^k - \frac{2}{3}\tilde{A}_{ij}\partial_k\beta^k \\ &\quad -8\pi\alpha\left(W^2 S_{ij} - \frac{1}{3}\tilde{\gamma}_{ij}S\right),\end{aligned} \tag{3.22}$$

$$\begin{aligned}\left(\partial_t - \beta^k\partial_k\right) F_i &= -16\pi\alpha J_i \\ &\quad +2\alpha\left(f^{kj}\partial_j\tilde{A}_{ik} + \tilde{A}_{ik}\partial_j f^{kj} - \frac{1}{2}\tilde{A}^{jl}\partial_i h_{jl} - 3\tilde{A}^k_i\partial_k\ln W - \frac{2}{3}\partial_i K\right) \\ &\quad +\delta^{jk}\left\{-2\tilde{A}_{ij}\partial_k\alpha + \left(\partial_k\beta^l\right)\partial_l h_{ij}\right. \\ &\quad \left.+\partial_k\left(\tilde{\gamma}_{il}\partial_j\beta^l + \tilde{\gamma}_{jl}\partial_i\beta^l - \frac{2}{3}\tilde{\gamma}_{ij}\partial_l\beta^l\right)\right\},\end{aligned} \tag{3.23}$$

where $f^{ij} = \tilde{\gamma}^{ij} - \delta^{ij}$.

As a gauge condition, we adopt the dynamical slicing for the lapse function [86, 87] and dynamical-shift equation for the shift vector [88]:

$$\left(\partial_t - \beta^k\partial_k\right)\alpha = -2K\alpha, \tag{3.24}$$

$$\partial_t\beta^i = \frac{3}{4}\tilde{\gamma}^{ij}\left(F_j + \Delta t\partial_t F_j\right), \tag{3.25}$$

where Δt is the numerical time step.

The fourth-order finite differencing in space and fourth-order Runge-Kutta time integration are applied in solving the evolution equations numerically. The advection term is treated with fourth-order upwind scheme.

3.2 3+1 decomposition for the matter field

In addition to the gravitational field, we have to solve the evolution of the matter field in the presence of the neutron star or accretion disk. We apply 3+1 decomposition onto the matter field in order to solve the general relativistic equation of motion. Here we define $S_0 := W^{-3}\rho_h$ and $S_i := W^{-3}J_i$, and derive the evolution equations for these variables from

$$\nabla_\mu T^\mu{}_\nu = 0. \tag{3.26}$$

By taking the spacial projection of Eq. (3.26) we obtain the evolution equation of S_i as

$$\partial_0 S_k + \partial_i\left(\alpha\sqrt{\gamma}S^i{}_k - \beta^i S_k\right) = -S_0\partial_k\alpha + S_i\partial_k\beta^i - \frac{1}{2}\alpha\sqrt{\gamma}S_{ij}\partial_k\gamma^{ij}. \tag{3.27}$$

This is the equation of motion for the matter field. By taking the time projection of Eq. (3.26) we obtain the evolution equation of S_0 as

$$\partial_0 S_0 + \partial_i \left(-S_0 \beta^i + \alpha S^i \right) = \alpha \sqrt{\gamma} S^{ij} K_{ij} - S_i D^i \alpha. \tag{3.28}$$

This is the energy equation for the matter field.

3.3 Magnetohydrodynamics

3.3.1 GRMHD equations

The fundamental variables in the hydrodynamics are rest-mass density ρ, specific internal energy ε, specific internal pressure P, and four velocity u^μ. We also define the following variables from the fundamental variables:

$$\begin{aligned}
\rho_* &:= \rho w W^{-3}, && (3.29)\\
v^i &:= \frac{dx^i}{dt} = \frac{u^i}{u^t} = -\beta^i + \gamma^{ij}\frac{u_j}{u^t}, && (3.30)\\
h &:= 1 + \varepsilon + \frac{P}{\rho}, && (3.31)\\
w &:= \alpha u^t. && (3.32)
\end{aligned}$$

Here, ρ_* is the conservative baryon rest-mass density, v^i is the three velocity, h is the specific enthalpy and w is the Lorentz factor measured by a normal observer. The fundamental variable in ideal magnetohydrodynamics is the magnetic field in the comoving frame b^μ. The electric field in the comoving frame $E^\mu := F^{\mu\nu} u_\nu$ is zero under the assumption of zero electrical resistivity, where $F^{\mu\nu}$ is the electromagnetic tensor. The current j^μ does not appear in the evolution equation explicitly. The magnetic field b^μ is defined by

$$b_\mu := -F^*_{\mu\nu} u^\nu = -\frac{1}{2} \epsilon_{\mu\nu\alpha\beta} u^\nu F^{\alpha\beta}, \tag{3.33}$$

where $F^*_{\mu\nu}$ is the dual tensor of $F_{\mu\nu}$, and $\epsilon_{\mu\nu\alpha\beta}$ is the Livi-Civita tensor with $\epsilon_{0123} = \sqrt{-g}$ and $\epsilon^{0123} = 1/\sqrt{-g}$. For evolving the magnetic field in the 3+1 decomposed formalism, we define the three-magnetic field measured in the inertia frame as follows.

$$\begin{aligned}
\mathcal{B}^i &:= W^{-3} \gamma^i{}_j F^{*j\mu} n_\mu \\
&:= W^{-3} B^i \\
&= W^{-3} (w b^i - \alpha b^t u^i). && (3.34)
\end{aligned}$$

Here, $\mathcal{B}^0 = 0$, and $\mathcal{B}^i$ satisfies $\mathcal{B}_i = \gamma_{ij} \mathcal{B}^j$. The relation between b^μ and $\mathcal{B}^i$ is as

$$b^0 = \frac{W^3 \mathcal{B}^i u_i}{\alpha}, \text{ and } b_i = \frac{W^3}{w} (\mathcal{B}_i + \mathcal{B}^j u_j u_i), \tag{3.35}$$

and thus,

$$b^2 = b_\mu b^\mu = \frac{W^3 (\mathcal{B}^2 + (\mathcal{B}^i u_i)^2}{w^2}, \tag{3.36}$$

where $\mathcal{B}^2 = \mathcal{B}^i \mathcal{B}_i$. The energy-momentum tensor of the ideal magnetohydrodynamical fluid is

$$T^{\mathrm{MHD}}_{\mu\nu} = T^{\mathrm{Fluid}}_{\mu\nu} + T^{\mathrm{EM}}_{\mu\nu}, \tag{3.37}$$

where $T^{\rm Fluid}_{\mu\nu}$ and $T^{\rm EM}_{\mu\nu}$ are the fluid and electromagnetic parts of the energy-momentum tensor defined by

$$\begin{aligned} T^{\rm Fluid}_{\mu\nu} &:= (\rho + \rho\varepsilon + P)u_\mu u_\nu + P g_{\mu\nu} \\ &= \rho h u_\mu u_\nu + P g_{\mu\nu}, \end{aligned} \tag{3.38}$$

$$\begin{aligned} T^{\rm EM}_{\mu\nu} &:= \frac{1}{4\pi}\left(F_{\mu\alpha}F^{\alpha}_{\nu} - \frac{1}{4}g_{\mu\nu}F_{\alpha\beta}F^{\alpha\beta}\right) \\ &= \frac{1}{4\pi}\left\{\left(\frac{1}{2}g_{\mu\nu} + u_\mu u_\nu\right)b^2 - b_\mu b_\nu\right\}. \end{aligned} \tag{3.39}$$

The 3+1 decomposition of $T^{\rm MHD}_{\mu\nu}$ derives the S_0, S_i, and S_{ij} for the ideal magnetohydrodynamical fluid as

$$S_0 = \rho_* h w - P W^{-3} + \frac{W^3}{4\pi}\left(\mathcal{B}^2 - \frac{1}{2w^2}\left[\mathcal{B}^2 + (\mathcal{B}^i u_i)^2\right]\right), \tag{3.40}$$

$$S_i = \rho_* h u_i + \frac{W^3}{4\pi w}\left[\mathcal{B}^2 u_i - (\mathcal{B}^j u_j)\mathcal{B}_i\right], \tag{3.41}$$

$$S_{ij} = \left(\rho h + \frac{b^2}{4\pi}\right)u_i u_j + \left(P + \frac{b^2}{8\pi}\right)\gamma_{ij} - \frac{1}{4\pi}b_i b_j. \tag{3.42}$$

If we do not take the neutrino radiation effect into account, the conservation of the energy-momentum tensor takes the following form: $\nabla_\mu T^{{\rm MHD}\mu}{}_\nu = 0$. By substituting Eqs. (3.40)–(3.42) into Eqs. (3.27) and (3.28) we obtain the explicit form of the evolution equation for S_0 and S_i as

$$\begin{aligned} \partial_0 S_i &+ \partial_j\left(S_i v^j + \alpha W^{-3}\left(P + \frac{b^2}{8\pi}\right)\delta^j_i - \frac{\alpha W^3}{4\pi w^2}\mathcal{B}^j[\mathcal{B}_i + (\mathcal{B}^k u_k)u_i]\right) \\ &= -S_0\partial_i\alpha + S_k\partial_i\beta^k - \alpha W^{-4}S^k{}_k\partial_i W - \frac{1}{2}\alpha W^{-1}S_{jk}\partial_i\tilde{\gamma}^{jk}, \end{aligned} \tag{3.43}$$

$$\begin{aligned} \partial_0 S_0 &+ \partial_j\left(S_0 v^j + W^{-3}\left(P + \frac{b^2}{8\pi}\right)(v^j + \beta^j) - \frac{\alpha W^3}{4\pi w}(\mathcal{B}^k u_k)\mathcal{B}^j\right) \\ &= \frac{\alpha}{3}W^{-3}KS^k{}_k + \alpha W^{-1}\hat{S}_{kl}\tilde{A}^{kl} - S_k D^k\alpha. \end{aligned} \tag{3.44}$$

In addition to the equation of motion and energy equation, the continuity equation is another component of the hydrodynamics equations. The continuity equation is written as

$$\nabla_\mu(\rho u^\mu) = 0, \tag{3.45}$$

and by using ρ_* and v^i, it is rewritten as

$$\partial_0\rho_* + \partial_i(\rho_* v^i) = 0. \tag{3.46}$$

The evolution of the magnetic field in the ideal magnetohydrodynamics is obtained from

$$\nabla_\mu F^{*\mu}{}_\nu = 0. \tag{3.47}$$

The spacial projection of Eq. (3.47) leads to the induction equation:

$$\partial_0\mathcal{B}^i = \partial_j(\mathcal{B}^j v^i - \mathcal{B}^i v^j), \tag{3.48}$$

and the time projection leads to the no-monopole constraint:

$$\partial_i\mathcal{B}^i = 0. \tag{3.49}$$

The no-monopole constraint is imposed when we give an initial condition of the magnetic field, and the induction equation is solved for evolving the magnetic field.

3.3.2 Numerical scheme

Magnetohydrodynamics equations are solved in a high-resolution shock capturing scheme [89–91] together with the second-order constrained-transport scheme [92] and Balsara's flux-preserving mesh refinement scheme [93].

The evolution equations can schematically be written as

$$\partial_0(U_A) + \partial_i(F^i_A) = S_A, \tag{3.50}$$

where $A \in [0, 7]$ and

$$U_A = (\rho_*, S_i, S_0, \mathcal{B}^i)^T, \tag{3.51}$$

$$F^j_A = \begin{pmatrix} \rho_* v^j \\ S_i v^j + \alpha W^{-3}\left(P + \dfrac{b^2}{8\pi}\right)\delta^j_i - \dfrac{\alpha W^3}{4\pi w^2}\mathcal{B}^j[\mathcal{B}_i + (\mathcal{B}^k u_k)u_i] \\ S_0 v^j + W^{-3}\left(P + \dfrac{b^2}{8\pi}\right)(v^j + \beta^j) - \dfrac{\alpha W^3}{4\pi w}(\mathcal{B}^k u_k)\mathcal{B}^j \\ \mathcal{B}^i v^j - \mathcal{B}^j v^i \end{pmatrix}, \tag{3.52}$$

$$S_A = \begin{pmatrix} 0 \\ -S_0\partial_i\alpha + S_k\partial_i\beta^k - \alpha W^{-4} S^k_k \partial_i W - \dfrac{1}{2}\alpha W^{-1} S_{jk}\partial_i\tilde{\gamma}^{jk} \\ \dfrac{\alpha}{3}W^{-3}KS^k_k + \alpha W^{-1}\hat{S}_{kl}\tilde{A}^{kl} - S_k D^k\alpha \\ 0 \end{pmatrix}. \tag{3.53}$$

These equations are in the conservation form. We adopt Kurganov-Tadmor high-resolution central difference scheme for solving this system [94]. In order to evaluate F^j_A, we calculate the quantities at the cell surface by a piecewise parabolic interpolation from the cell center. The quantities at the right- and left-hand side of each cell surface are interpolated as

$$Q_{(L)} = Q_i + \frac{\Phi(r^+_{i-1})\Delta_{i-1}}{6} + \frac{\Phi(r^-_i)\Delta_i}{3}, \tag{3.54}$$

$$Q_{(R)} = Q_{i+1} - \frac{\Phi(r^+_i)\Delta_i}{6} - \frac{\Phi(r^-_{i+1})\Delta_{i+1}}{3}, \tag{3.55}$$

$$\tag{3.56}$$

where $\Delta_{i+1} = Q_{i+1} - Q_i$. Φ is a limiter function defined by

$$\Phi(r) = \text{minmod}(1, br) \tag{3.57}$$

$(1 \le b \le 4$ for total variation diminishing condition),

$$\text{minmod}(1, x) = \begin{cases} 1 & \text{if } x > 1 \\ x & \text{if } 1 > x > 0 \\ 0 & \text{if } x < 0 \end{cases}. \tag{3.58}$$

The parameter b is chosen to be 2 in this work. From the interpolated value at the cell surface, we obtain the fluxes $F_{(L)}$ and $F_{(R)}$, and the maximum wave speed c_L and c_R at the left- and right-hand sides of each cell surface. Then we calculate the flux as

$$F = \frac{1}{2}[F_L + F_R - c_{\max}(U_R - U_L)], \tag{3.59}$$

$$c_{\max} = \max(c_L, c_R). \tag{3.60}$$

Note that superscript j and subscript A for the flux F_A^j are abbreviated here. In order to evaluate the wave speed at the cell surface, the eigenvalues for the Jacobi matrix $\partial F/\partial U$ are required. Three of the seven solutions for the eigenvalues in the x^i direction are

$$\lambda = v^i, \quad \frac{b^i \pm u^i\sqrt{\rho h + b^2}}{b^t \pm u^t\sqrt{\rho h + b^2}}, \tag{3.61}$$

and the other four solutions are obtained by solving the following equation [95]

$$\left(u^t\right)^4 (\lambda - v^i)^4(1-\zeta) + \left[c_s^2\frac{\left(b^i - \lambda b^t\right)^2}{\rho h + b^2} - \left(u^t\right)^2\left(\lambda - v^i\right)^2\left(\gamma^{ii} - \frac{\beta^i + \lambda}{\alpha^2}\right)\zeta\right] = 0, \tag{3.62}$$

where c_s is the sound velocity. ζ and the Alfvén velocity v_A are defined, respectively, by

$$\zeta = v_A^2 + c_s^2 - v_A^2 c_s^2, \tag{3.63}$$

$$v_A = \frac{b^2}{4\pi\rho h + b^2}. \tag{3.64}$$

In the Kurganov-Tadmor scheme, the maximum characteristic speed is only required. For simplicity and saving computational cost, we use the prescription [96] that replaces the fourth-order equation to approximately by a second-order equation as

$$\left(u^t\right)^2\left(\lambda - v^i\right)^2(1-\zeta) - \zeta\left(\gamma^{ii} - \frac{\beta^i + \lambda}{\alpha^2}\right) = 0. \tag{3.65}$$

The solution for this equation is

$$\lambda = \frac{1}{\alpha^2 - V_k V^k \zeta} \times \left[v^i\alpha^2(1-\zeta) - \beta^i\zeta\left(\alpha^2 - V^2\right) \pm \alpha\sqrt{\zeta}\sqrt{\left(\alpha^2 - V^2\right)\left\{\gamma^{ii}\left(\alpha^2 - V^2\zeta\right) - (1-\zeta)V^iV^i\right\}}\right], \tag{3.66}$$

where $V^i = v^i + \beta^i$ and $V^2 = \gamma_{ij}V^iV^j$.

To solve the induction equation, we must adopt the scheme that the no-monopole constraint is not violated, or otherwise, such violation accumulates and could result in a nonreliable solution. Therefore, we adopt a constrained-transport scheme [92]. In this scheme, we define a cell for numerical computation with geometrical and fluid variables at the center and magnetic field variables at the surface of the cell. In addition, electric field variables, which are related to the flux for the evolution of the magnetic field,

$$\mathcal{E}^x = -v^y\mathcal{B}^z + v^z\mathcal{B}^y, \tag{3.67}$$

$$\mathcal{E}^y = -v^z\mathcal{B}^x + v^x\mathcal{B}^z, \tag{3.68}$$

$$\mathcal{E}^z = -v^x\mathcal{B}^y + v^y\mathcal{B}^x, \tag{3.69}$$

are placed at the edge of the cell. When we label the grid at the cell as (i, j, k), the magnetic field variables $\mathcal{B}^x$, $\mathcal{B}^y$, and $\mathcal{B}^z$ are defined at $(i, j+1/2, k+1/2)$, $(i+1/2, j, k+1/2)$, and $(i+1/2, j+1/2, k)$, respectively, and the electric field variables $\mathcal{E}^x$, $\mathcal{E}^y$, and $\mathcal{E}^z$ are defined

at $(i+1/2, j, k)$, $(i, j+1/2, k)$, and $(i, j, k+1/2)$, respectively. Then the induction equation is discretized as

$$\partial_0 \left(\mathcal{B}^x\right)_{i,j+\frac{1}{2}k+\frac{1}{2}} = -\frac{\left(\mathcal{E}^z\right)_{i,j+1,k+\frac{1}{2}} - \left(\mathcal{E}^z\right)_{ij,k+\frac{1}{2}}}{\Delta y} + \frac{\left(\mathcal{E}^y\right)_{i,j+\frac{1}{2}k+1} - \left(\mathcal{E}^y\right)_{i,j+\frac{1}{2}k}}{\Delta z}, \tag{3.70}$$

$$\partial_0 \left(\mathcal{B}^y\right)_{i+\frac{1}{2}j,k+\frac{1}{2}} = -\frac{\left(\mathcal{E}^x\right)_{i+\frac{1}{2}j,k+1} - \left(\mathcal{E}^x\right)_{i+\frac{1}{2}j,k}}{\Delta z} + \frac{\left(\mathcal{E}^z\right)_{i+1,j,k+\frac{1}{2}} - \left(\mathcal{E}^z\right)_{i,j,k+\frac{1}{2}}}{\Delta x}, \tag{3.71}$$

$$\partial_0 \left(\mathcal{B}^z\right)_{i+\frac{1}{2},j+\frac{1}{2},k} = -\frac{\left(\mathcal{E}^y\right)_{i+1,j+\frac{1}{2}k} - \left(\mathcal{E}^y\right)_{i,j+\frac{1}{2}k}}{\Delta x} + \frac{\left(\mathcal{E}^x\right)_{i+\frac{1}{2}j+1,k} - \left(\mathcal{E}^x\right)_{i+\frac{1}{2}j,k}}{\Delta y}, \tag{3.72}$$

where $(\Delta x, \Delta y, \Delta z)$ are the grid spacing. In order to evaluate the electric field, the magnetic field defined at the cell surface has to be interpolated to the cell edge using piecewise parabolic interpolation. We adopt the scheme [97] that writes the flux as

$$\mathcal{E}^x = \frac{\left(\mathcal{E}^x\right)^{LL} + \left(\mathcal{E}^x\right)^{LR} + \left(\mathcal{E}^x\right)^{RL} + \left(\mathcal{E}^x\right)^{RR}}{4} + \frac{c_y}{2}\left(\mathcal{B}^z_R - \mathcal{B}^z_L\right) - \frac{c_z}{2}\left(\mathcal{B}^y_R - \mathcal{B}^y_L\right), \tag{3.73}$$

at $(i+1/2, j, k)$. Here $\left(\mathcal{E}^x\right)^{LR}$ is the flux defined at the left-hand side in the y direction and right-hand side in the z direction. The other fluxes $\left(\mathcal{E}^x\right)^{LL}$, $\left(\mathcal{E}^x\right)^{RL}$, and $\left(\mathcal{E}^x\right)^{RR}$ are defined in the similar way. c_y and c_z are the characteristic speed for the prescription of an upwind flux construction and are calculated by simple average:

$$\left(c_y\right)_{i+\frac{1}{2},j,k} = \frac{\left(v^y\right)_{i,j,k} + \left(v^y\right)_{i+1,j,k}}{2}, \tag{3.74}$$

$$\left(c_z\right)_{i+\frac{1}{2},j,k} = \frac{\left(v^z\right)_{i,j,k} + \left(v^z\right)_{i+1,j,k}}{2}. \tag{3.75}$$

The expression for $\mathcal{E}^y$ and $\mathcal{E}^z$ are written in a similar way by permutation of the indices.

3.4 Neutrino radiation transport

Neutrino transfer is handled using a leakage-based scheme [98] together with a truncated moment formalism using a closure relation for the free-streaming component [99, 100]. Neutrino heating and absorption on free nucleons are incorporated using the updated numerical procedure [101].

3.4.1 Energy-momentum conservation equations

The energy-momentum conservation for the general-relativistic magnetohydrodynamics with neutrino radiation transfer is written as

$$\nabla_\alpha T^{(\mathrm{Total})\alpha}{}_\beta = \nabla_\alpha \left[T^{(\mathrm{MHD})\alpha}{}_\beta + T^{(\nu)\alpha}{}_\beta\right] = 0, \tag{3.76}$$

where $T^{(\mathrm{Total})\alpha}{}_\beta$ is the total energy-momentum tensor and $T^{(\nu)\alpha}_\beta$ is the energy-momentum tensor for neutrinos. It can be decomposed into the magnetohydrodynamics part and neutrino radiation transport part as

$$\nabla_\alpha T^{(\mathrm{MHD})\alpha}{}_\beta = -Q_\beta, \tag{3.77}$$

$$\nabla_\alpha T^{(\nu)\alpha}{}_\beta = Q_\beta, \tag{3.78}$$

$$\tag{3.79}$$

where Q_β is the interaction term. However, the timescale of this interaction between fluid and neutrino is much shorter than the dynamical timescale in hot dense matters. If we are to numerically solve this interaction explicitly, a very short time step is required, which makes the computational cost very expensive. To overcome this problem, we adopt the formulation that phenomenologically decomposes the neutrino part into the "trapped" and "streaming" parts as

$$T^{(\nu)\alpha}{}_\beta = T^{(\nu,\mathrm{T})\alpha}{}_\beta + T^{(\nu,\mathrm{S})\alpha}{}_\beta, \tag{3.80}$$

where $T^{(\nu,\mathrm{T})\alpha}{}_\beta$ and $T^{(\nu,\mathrm{S})\alpha}{}_\beta$ are the energy-momentum tensor of the "trapped" and "streaming" neutrinos respectively. Here, the "trapped" part represents neutrinos that interact with matter sufficiently frequently and can be treated as a part of the fluid. The "streaming" part represents neutrinos that do not interact with fluid frequently and freely stream out from the system. Also, we assume that some of the "trapped" neutrinos "leak out" and become "streaming" neutrinos at a leakage rate of $Q^{(\mathrm{leak})}_\beta$. Then, Eq. (3.76) can be decomposed as

$$\nabla_\alpha T^{(\mathrm{MHD}+\nu,\mathrm{T})\alpha}{}_\beta = \nabla_\alpha \left[T^{(\mathrm{MHD})\alpha}{}_\beta + T^{(\nu,\mathrm{T})\alpha}{}_\beta \right] = -Q^{(\mathrm{leak})}{}_\beta, \tag{3.81}$$

$$\nabla_\alpha T^{(\nu,\mathrm{S})\alpha}{}_\beta = Q^{(\mathrm{leak})}{}_\beta. \tag{3.82}$$

The energy-momentum tensor of the fluid, electromagnetic field and trapped neutrinos $T^{(\mathrm{MHD}+\nu,\mathrm{T})\alpha}_{\quad\beta}$ are treated in the form of Eqs. (3.37)–(3.39). The specific internal energy and the pressure are written as

$$\varepsilon = \varepsilon_\mathrm{B} + \varepsilon_\mathrm{e} + \varepsilon_\mathrm{ph} + \varepsilon_\nu, \tag{3.83}$$

$$P = P_\mathrm{B} + P_\mathrm{e} + P_\mathrm{ph} + P_\nu, \tag{3.84}$$

where the subscript B, e, ph, and ν represent the contribution from baryons, electrons and photons, and neutrinos. ε and P are obtained through an EOS. By adding the leakage rate $Q^{(\mathrm{leak})}_\beta$ to the source term of Eqs. (3.43) and (3.44), we acquire the equation of motion and energy equation as

$$\begin{aligned} \partial_0 S_i &+ \partial_j \left(S_i v^j + \alpha W^{-3} \left(P + \frac{b^2}{8\pi} \right) \delta^j_i - \frac{\alpha W^3}{4\pi w^2} \mathcal{B}^j [\mathcal{B}_i + (\mathcal{B}^k u_k) u_i] \right) \\ &= -S_0 \partial_i \alpha + S_k \partial_i \beta^k - \alpha W^{-4} S^k_k \partial_i W - \frac{1}{2} \alpha W^{-1} S_{jk} \partial_i \tilde{\gamma}^{jk} - \alpha W^{-3} Q^{(\mathrm{leak})\beta} \gamma_{\beta i}, \end{aligned} \tag{3.85}$$

$$\begin{aligned} \partial_0 S_0 &+ \partial_j \left(S_0 v^j + W^{-3} \left(P + \frac{b^2}{8\pi} \right) (v^j + \beta^j) - \frac{\alpha W^3}{4\pi w} (\mathcal{B}^k u_k) \mathcal{B}^j \right) \\ &= \frac{\alpha}{3} W^{-3} K S^k{}_k + \alpha W^{-1} \hat{S}_{kl} \tilde{A}^{kl} - S_k D^k \alpha + \alpha W^{-3} Q^{(\mathrm{leak})\beta} n_\beta. \end{aligned} \tag{3.86}$$

For the streaming neutrinos, the energy-momentum tensor is written as

$$T^{(\nu,\mathrm{S})}_{\alpha\beta} = E n_\alpha n_\beta + F_\alpha n_\beta + F_\beta n_\alpha + P_{\alpha\beta}. \tag{3.87}$$

Here $E = T^{(\nu,\mathrm{S})}_{\alpha\beta} n^\alpha n^\beta$, $F_\alpha = T^{(\nu,\mathrm{S})}_{\sigma\beta} \gamma^\sigma_\alpha n^\beta$, and $P_{\alpha\beta} = T^{(\nu,\mathrm{S})}_{\rho\sigma} \gamma^\rho_\alpha \gamma^\sigma_\beta$ are the energy density, the energy flux, and the spacial stress tensor of the streaming neutrinos respectively. Also, they are the zeroth-, first-, and second-rank moments for the distribution function of the radiation field respectively [99]. In this work, we obtain the approximate solution

of the radiation by solving the evolution equation for zeroth- and first-rank moments. The higher-rank moments are determined from the zeroth- and first-rank moments by closure relations. This is truncated momentum formalism [100] and it significantly reduces the computational cost by reducing a six-dimensional problem into a four-dimensional problem. F_α and $P_{\alpha\beta}$ satisfy $F_\alpha n^\alpha = 0$ and $P_{\alpha\beta} n^\alpha = 0$. By considering Eqs. (3.27) and (3.28), the evolution equations for E and F_i are explicitly written as,

$$\partial_0 \tilde{E} + \partial_k \left(\alpha \tilde{F}^k - \beta^k \tilde{E} \right) = \alpha \tilde{P}^{kl} K_{kl} - \tilde{F}^k \partial_k \alpha - \alpha W^{-3} Q^{(\mathrm{leak})\beta} n_\beta, \tag{3.88}$$

$$\partial_0 \tilde{F}_i + \partial_k \left(\alpha \tilde{P}^k_i - \beta^k \tilde{F}_i \right) = -\tilde{E} \partial_i \alpha + \tilde{F}_k \partial_i \beta^k + \frac{\alpha}{2} \tilde{P}^{kl} \partial_i \gamma_{kl} + \alpha W^{-3} Q^{(\mathrm{leak})\beta} \gamma_{\beta i}, \tag{3.89}$$

where $\tilde{E} = W^{-3} E$, $\tilde{F}_k = W^{-3} F_k$, and $\tilde{P}_{kl} = W^{-3} P_{kl}$. In this formalism, we need to determine P^{kl} from E and F^k. We adopt the M1-closure relation for this [102, 103]. Specifically, the spacial stress tensor P^{kl} is written as

$$P^{ij} = \frac{3\chi - 1}{2} \left(P^{ij} \right)_{\mathrm{thin}} + \frac{3(1-\chi)}{2} \left(P^{ij} \right)_{\mathrm{thick}}, \tag{3.90}$$

$$\left(P^{ij} \right)_{\mathrm{thin}} = E \frac{F^i F^j}{\gamma_{kl} F^k F^l}, \tag{3.91}$$

$$\begin{aligned} \left(P^{ij} \right)_{\mathrm{thick}} &= \frac{E}{2w^2 + 1} \left[\left(2w^2 - 1 \right) \gamma^{ij} - 4 V^i V^j \right] \\ &\quad + \frac{1}{w} \left[F^i V^j + F^j V^i \right] + \frac{2 F^k u_k}{w \left(2w^2 + 1 \right)} \left[-w^2 \gamma^{ij} + V^i V^j \right], \end{aligned} \tag{3.92}$$

where $V^i = \gamma^{ij} u_j$. χ is the so-called variable Eddington factor which is chosen to be [102]

$$\chi = \frac{3 + 4f^2}{5 + 2\sqrt{4 - 3f^2}}, \tag{3.93}$$

$$f = \sqrt{\frac{h_{\alpha\beta} H^\alpha H^\beta}{J}}. \tag{3.94}$$

Here, $J = T^{(\nu,\mathrm{S})}_{\alpha\beta} u^\alpha u^\beta$ and $H_\alpha = T^{(\nu,\mathrm{S})}_{\sigma\beta} h^\sigma_\alpha u^\beta$ are the energy density and the energy flux of streaming neutrino measured in the fluid rest frame, respectively. A projection operator is defined by $h_{\alpha\beta} = g_{\alpha\beta} + u_\alpha u_\beta$.

3.4.2 Baryon- and lepton-number conservation equations

In addition to the continuity equation for baryon described in Eqs. (3.45) and (3.46), we need to solve the conservation equations of the lepton fractions written as

$$\partial_0 (\rho_* Y_e) + \partial_k (\rho_* Y_e v^k) = \alpha W^{-3} \rho (-\gamma^{\mathrm{local}}_{\nu_e} + \gamma^{\mathrm{local}}_{\bar{\nu}_e}), \tag{3.95}$$

$$\partial_0 (\rho_* Y_{\nu_e}) + \partial_k (\rho_* Y_{\nu_e} v^k) = \alpha W^{-3} \rho (\gamma^{\mathrm{local}}_{\nu_e} - \gamma^{\mathrm{leak}}_{\nu_e}), \tag{3.96}$$

$$\partial_0 (\rho_* Y_{\bar{\nu}_e}) + \partial_k (\rho_* Y_{\bar{\nu}_e} v^k) = \alpha W^{-3} \rho (\gamma^{\mathrm{local}}_{\bar{\nu}_e} - \gamma^{\mathrm{leak}}_{\bar{\nu}_e}), \tag{3.97}$$

$$\partial_0 (\rho_* Y_{\nu_x}) + \partial_k (\rho_* Y_{\nu_x} v^k) = \alpha W^{-3} \rho (\gamma^{\mathrm{local}}_{\nu_x} - \gamma^{\mathrm{leak}}_{\nu_x}). \tag{3.98}$$

Here, Y_e, Y_{ν_e}, $Y_{\bar{\nu}_e}$, and Y_{ν_x} is the fraction per baryon number for electrons, electron neutrinos, electron anti-neutrinos, and the other neutrinos, i.e. the total of μ and τ neutrinos and anti-neutrinos. γ^{local} and γ^{leak} are the local production rate and leakage rate for each neutrino, respectively. For the local cooling process, we consider electron

capture, positron capture, electron–positron pair annihilation, plasmon decay, and the bremsstrahlung radiation of pair neutrinos, and for the local heating process, we consider the electron neutrino and electron anti-neutrino absorption processes. The local processes have timescales characterized by the weak-interaction, which is much shorter than the dynamical time scale of the system. In order to solve the equations with a usual time step ($\Delta t \approx O(0.1)\,\mu$s) we adopt the following procedure. First, we consider the following conservation equation for the total lepton fraction:

$$\partial_0(\rho_* Y_l) + \partial_k(\rho_* Y_l v^k) = \alpha W^{-3}\rho(-\gamma^{\rm leak}_{\nu_e} + \gamma^{\rm leak}_{\bar{\nu}_e}), \tag{3.99}$$

where $Y_l = Y_e + Y_{\nu_e} - Y_{\bar{\nu}_e}$. The time scale of the source term is that of the leakage and thus it can be solved explicitly. Here, we solve Eq. (3.99) together with Eqs. (3.46), (3.85), (3.86), (3.88), (3.89), (3.98), under the the assumption of the β-equilibrium. We obtain the lepton fractions in the "hypothetical" β-equilibrium (Y^β_e, $Y^\beta_{\nu_e}$, and $Y^\beta_{\bar{\nu}_e}$) from the evolved Y_l. Second, we solve the entire evolution equation including the conservation equation for each lepton fraction. Here, we limit the source term for the local processes as

$$\gamma^{\rm local}_{\nu_e} = \min\left[\gamma^{\rm local}_{\nu_e}, \gamma^{\rm local}_{\nu_e,{\rm max}}\right], \tag{3.100}$$

$$\gamma^{\rm local}_{\bar{\nu}_e} = \min\left[\gamma^{\rm local}_{\bar{\nu}_e}, \gamma^{\rm local}_{\bar{\nu}_e,{\rm max}}\right], \tag{3.101}$$

$$Q^{\rm local}_{\nu_e} = \min\left[Q^{\rm local}_{\nu_e}, Q^{\rm local}_{\nu_e}\left(\gamma^{\rm local}_{\nu_e,{\rm max}}/\gamma^{\rm local}_{\nu_e}\right)\right], \tag{3.102}$$

$$Q^{\rm local}_{\bar{\nu}_e} = \min\left[Q^{\rm local}_{\bar{\nu}_e}, Q^{\rm local}_{\bar{\nu}_e}\left(\gamma^{\rm local}_{\bar{\nu}_e,{\rm max}}/\gamma^{\rm local}_{\bar{\nu}_e}\right)\right], \tag{3.103}$$

where $\gamma^{\rm local}_{\nu_e,{\rm max}}$ and $\gamma^{\rm local}_{\bar{\nu}_e,{\rm max}}$ are the maximum local production rates under the assumption that $Y^\beta_{\nu_e}$, and $Y^\beta_{\bar{\nu}_e}$ are the maximum neutrino fractions allowed for the next time step. Third, we check the condition,

$$\mu_p + \mu_e < \mu_n + \mu_{\nu_e}, \tag{3.104}$$

$$\mu_n - \mu_e < \mu_p + \mu_{\bar{\nu}_e}, \tag{3.105}$$

where $\mu_p, \mu_n, \mu_e, \mu_{\nu_e}$, and $\mu_{\bar{\nu}_e}$ are the chemical potentials of protons, neutrons, electrons, electron neutrinos, and electron anti-neutrinos, respectively. When both conditions are satisfied, we regard that the β-equilibrium is achieved, and we reset the lepton fractions for the next timestep to be $Y^\beta_e, Y^\beta_{\nu_e}$, and $Y^\beta_{\bar{\nu}_e}$.

3.5 Microphysics

3.5.1 Equation of state

For the EOS, we adpot DD2 [104] and SFHo [105] for a high-density range and Helmholtz EOS [106] for a low-density range. These EOSs are tabulated in terms of rest-mass density ρ, temperature T, and electron fraction Y_e (for non-β-equilibrium case) or total lepton fraction Y_l (for β-equilibrium case). These EOSs include baryons (free protons, free neutrons, α-particles, and heavy nuclei), leptons (electrons, positrons, and trapped neutrinos), and photons to the specific internal energy and the pressure. For the DD2 and SFHo EOSs, the circumferential radius of the isolated spherical neutron star of mass 1.3–1.4$M_\odot$ is ≈ 13.2 km and ≈ 11.9 km, respectively. These EOSs satisfy constraints imposed by the observation of gravitational waves for GW170817 [4] and by the X-ray observation by NICER [107].

3.5.2 Weak-interaction and leakage rates

The leakage rates are phenomenologically defined by

$$Q_{\alpha}^{\rm leak} = \sum_{(\nu)} Q_{(\nu)}^{\rm leak} u_{\alpha} = \sum_{(v)} \left[\left(1 - e^{-b\tau_{(\nu)}} \right) Q_{(\nu)}^{\rm diff} + e^{-b\tau_{(\nu)}} Q_{(\nu)}^{\rm local} \right] u_{\alpha}, \tag{3.106}$$

$$\gamma_{(\nu)}^{\rm leak} = \left(1 - e^{-b\tau_{(\nu)}} \right) \gamma_{(\nu)}^{\rm diff} + e^{-b\tau_{(\nu)}} \gamma_{(\nu)}^{\rm local}, \tag{3.107}$$

where $\tau_{(\nu)}$ is the optical depth for neutrinos and b is a constant parameter that is set to be $b^{-1} = 2/3$. $Q_{(\nu)}^{\rm leak}$ is regarded as the emissivity of neutrinos measured in the fluid rest frame. The subscript (ν) is the abbreviation for each species of neutrinos ν_e, $\bar{\nu}_e$, and ν_x. The superscript diff and local correspond to the diffusion [108] and local production. As a local production reaction, we consider electron and positron capture [109], electron-positron annihilation [110], plasmon decay [111, 112], and nucleon-nucleon bremsstrahlung process [113]. We also consider electron neutrino and electron anti-neutrino absorption processes [114] for the local heating process.

The optical depth is calculated by

$$\tau_{(\nu)} = \min \left[\tau_{(\nu)}^{x}, \tau_{(\nu)}^{y}, \tau_{(\nu)}^{z} \right], \tag{3.108}$$

where $\tau_{(\nu)}^{x}$, $\tau_{(\nu)}^{y}$, and $\tau_{(\nu)}^{z}$ are the optical depths along x, y, and z direction respectively. For example, $\tau_{(\nu)}^{x}$ is obtained by integrating the opacity of the neutrinos as

$$\tau_{(v)}^{x}(x,y,z) = E_{(\nu)}(x,y,z)^2 \tilde{\tau}_{(\nu)}^{x}(x,y,z), \tag{3.109}$$

$$\tilde{\tau}_{(\nu)}^{x}(x,y,z) = \int_{x}^{x_{\rm out}} \tilde{\kappa}_{(\nu)} \left(x', y, z \right) dx', \tag{3.110}$$

$$\tilde{\kappa}_{(\nu)} = \kappa_{(\nu)} / E_{(\nu)}^2, \tag{3.111}$$

where $x_{\rm out}$ is the outer boundary of the computational domain in the x direction, and $\kappa_{(\nu)}$ is an opacity. The neutrino energy $E_{(\nu)}$ is obtained by solving the following algebraic equation

$$\begin{aligned} E_{(\nu)} &= \left(1 - e^{-\tau_{(v)}/a} \right) E_{(\nu)}^{\rm diff} + e^{-\tau_{(\nu)}/a} E_{(\nu)}^{\rm local} \\ &= \left(1 - e^{-{E_{(\nu)}}^2 \tilde{\tau}_{(v)}/a} \right) E_{(\nu)}^{\rm diff} + e^{-{E_{(\nu)}}^2 \tilde{\tau}_{(\nu)}/a} E_{(\nu)}^{\rm local}, \end{aligned} \tag{3.112}$$

by the Newton-Raphson method. Here, the constant parameter a is set to be 5. $E_{(\nu)}^{\rm diff}$ and $E_{(\nu)}^{\rm local}$ are the average diffusion and local production energy, which are given respectively by

$$E_{(\nu)}^{\rm diff} = k_B T \frac{F_3 \left(\mu_{(\nu)}/k_B T \right)}{F_2 \left(\mu_{(\nu)}/k_B T \right)} \tag{3.113}$$

$$E_{(\nu)}^{\rm local} = \frac{m_u}{\rho} \frac{Q_{(\nu)}^{\rm local}}{\gamma_{(\nu)}^{\rm local}} \tag{3.114}$$

where $F_k(x)$ is the Fermi-Dirac integral and m_u is the atomic mass unit.

3.6 Primitive recovery

The numerical calculations for primitive recovery are performed based on Ref. [90, 115] The quantities numerically evolved are the conservation quantities ρ_*, S_i, S_0, $\mathcal{B}^i$, $\rho_* Y_e$ or $\rho_* Y_l$ and geometrical variables. From these quantities, we need to obtain the primitive quantities ρ, T, and Y_e or Y_l which are the argument variables of the EOS table, together with w. Note that Y_e or Y_l can be directly calculated from the conserved variables. For obtaining primitive variables, we first consider normalization condition for u^μ in the following form:

$$s^2 = \rho_*^{-2}\gamma^{ij}S_iS_j = \left(B^2+hw\right)^2\left(1-w^{-2}\right) - D^2(hw)^{-2}\left(B^2+2hw\right), \quad (3.115)$$

where

$$B^2 = W^3\frac{\mathcal{B}^i\mathcal{B}_i}{4\pi\rho_*}, \text{ and } D^2 = W^3\frac{(\mathcal{B}^iS_i)^2}{4\pi\rho_*}. \quad (3.116)$$

This can be regarded as the equation of hw and w^{-2} for the given data set of s^2, B^2, and D^2. We next consider the definition S_0 and obtain

$$\frac{S_0}{\rho_*} = hw - \frac{PW^{-3}}{\rho_*} + B^2 - \frac{1}{2}\left[B^2w^{-2} + D^2(hw)^{-2}\right]. \quad (3.117)$$

This can also be regarded as the equation of hw and w^{-2} for the given data set of ρ_*, S_0, B^2, and D^2. In order to determine primitive variables using Eqs. (3.115), (3.117), and tabulated EOS, we need the following iteration procedure. First, we give a trial value $\hat{w}$ for w, then we obtain the trial value of the rest-mass density $\hat{\rho} = \rho_* W^3/\hat{w}$. Second, we obtain the trial value for the temperature $\hat{T}$ by solving Eq. (3.117) in the form of

$$S_0 - \rho_* B^2 + \frac{1}{2}\rho_*\left[B^2w^{-2} + D^2(hw)^{-2}\right] - \sum_{(\nu)} S_{0,(\nu)}(\hat{\rho}, Y_{(\nu)}, \hat{T}) = S_{0,\mathrm{EOS}}(\hat{\rho}, Y_e, \hat{T}). \quad (3.118)$$

Here, $S_{0,\mathrm{EOS}}(\hat{\rho}, Y_e, \hat{T})$ is evaluated from the tabulated EOS that does not include the contributions from the trapped neutrinos, and $S_{0,(\nu)}(\hat{\rho}, Y_{(\nu)}, \hat{T})$ is the contributions from trapped neutrinos. Note that the one-dimensional search over the EOS table is required to obtain $\hat{T}$. Third, we calculate the next trial value $\hat{w}$ from $\hat{\rho}$ and $\hat{T}$. For this, we solve Eq. (3.115) for w by the Newton-Raphson method. By repeating these three steps until the solution converges, we obtain primitive variables ρ, T, and w. Until here, we have described the recovery procedure for the non-β-equilibrium case.

For the case that β-equilibrium is archived we need a slight modification. First, we need to prepare the β-equilibrium EOS. Then the Eq. (3.118) is modified in to

$$S_0 - \rho_* B^2 + \frac{1}{2}\rho_*\left[B^2w^{-2} + D^2(hw)^{-2}\right] = S^\beta_{0,\mathrm{EOS}}(\hat{\rho}, Y_l, \hat{T}), \quad (3.119)$$

where $S^\beta_{0,\mathrm{EOS}}(\hat{\rho}, Y_e, \hat{T})$ is evaluated from the β-equilibrium EOS. Note that β-equilibrium EOS includes the contributions from the trapped neutrinos. After ρ and T are obtained, we calculate the electron fraction $Y_e = Y_e(\rho, Y_l, T)$ using the β-equilibrium EOS.

3.7 Fixed-mesh refinement algorithm

The simulation is performed using a fixed-mesh refinement (FMR) algorithm. This algorithm enable us to simultaneously resolve the compact objects and cover a large spatial region. The computational domains consist of $i_{\rm max} = 9$–11 cuboids depending on models, centered at an approximate center of mass of the system. The i-th refinement level covers a half or full cubic box of $[-L_i : L_i]\times[-L_i : L_i]\times[0 : L_i]$ or $[-L_i : L_i]\times[-L_i : L_i]\times[-L_i : L_i]$, where $L_i = N\Delta x_i$ and Δx_i is the grid spacing for the i-th level. For the half-cubic box case, the plane-symmetric boundary condition on the $z = 0$ plane (equatorial plane) is imposed. The grid spacing for each level is determined by $\Delta x_i = 2\Delta x_{i+1}$ $(i = 1, 2, \cdots, i_{\rm max} - 1)$. For the DD2 EOS models, $\Delta x_{i_{\rm max}}$ is chosen to be $\Delta x_{i_{\rm max}} = 400\,{\rm m}$,and $270\,{\rm m}$ for low- and high-resolution models respectively. For SFHo EOS model, $\Delta x_{i_{\rm max}} = 250\,{\rm m}$ is adopted. The values of the N is chosen to be 170–282 depending on models. The detailed values of $i_{\rm max}$, $\Delta x_{i_{\rm max}}$, and N for each models will be described in the later chapters.

3.8 Prescription for shift vector

During the merger stage, the black hole is kicked mainly by the back reaction of the dynamical mass ejection in our present setting (see Chapter 4 and 5) and the resulting velocity is $v_{\rm kick} = 200$–$400\,{\rm km/s}$ (which is estimated by $m_{\rm ej}v_{\rm ej}/M_{\rm BH}$ with $m_{\rm ej}$ dynamical ejecta mass, $v_{\rm ej}(\sim 0.2c)$ its absolute average velocity, and $M_{\rm BH}$ the remnant black hole mass). Thus, the black hole moves toward a refinement boundary of the finest FMR level with time and eventually escapes from the highest-resolution level in the absence of any prescription. To keep the black hole in the highest-resolution level, we control the shift vector by modifying Eq. 3.25 in the following prescription:

$$\begin{aligned}\partial_t\beta^i &= \frac{3}{4}\tilde{\gamma}^{ij}\left(F_j + \partial_t F_j \Delta t\right) - \frac{v^i_{\rm BH}}{T_{\rm relax}} \\ &\quad \text{for } T_{\rm sta} < t < T_{\rm sta} + T_{\rm relax}, \qquad (3.120)\\ \partial_t\beta^i &= \frac{3}{4}\tilde{\gamma}^{ij}\left(F_j + \partial_t F_j \Delta t\right) \\ &\quad \text{for other cases}, \qquad (3.121)\end{aligned}$$

where $v^i_{\rm BH}$, $T_{\rm relax}$, and $T_{\rm sta}$ are constants that we determine appropriately based on the numerical result. $v^i_{\rm BH}$ is the coordinate velocity of the black-hole center (the location of the puncture) just before modifying the shift vector, which is of order $10^{-3}c$ as we already mentioned. $T_{\rm relax}$ is the relaxation time, which we choose $T_{\rm relax} = 40$ ms. $T_{\rm sta}$ is the starting time of this prescription, and it is set to be $T_{\rm sta} \approx 100$–200 ms to satisfy $v_{\rm kick}(T_{\rm sta} + T_{\rm relax}) \lesssim L_{i_{\rm max}}/2$.

3.9 Initial setups

As initial data, we prepare black hole-neutron star binaries in a quasi-equilibrium state assuming the neutrinoless beta-equilibrium cold state [45]. The initial gravitational mass of the neutron star is set to be $M_{\rm NS} = 1.35M_\odot$ following Ref. [45]. For the initial black-hole mass, we choose $M_{\rm BH,0} = 5.4M_\odot$ or $8.1M_\odot$; the mass ratio of the black hole to the neutron star is $Q := M_{\rm BH,0}/M_{\rm NS} = 4$ or 6. The initial dimensionless spin parameter of the black hole is set to be 0.75. With such a spin, tidal disruption of the neutron star with $M_{\rm NS} = 1.35M_\odot$ takes place for a wide range of Q. The initial orbital angular velocity Ω_0 is set to be $m_0\Omega_0 = 0.056$ for $Q = 4$ and 0.064 for $Q = 6$, where m_0 is the sum of the

initial black-hole mass and neutron-star mass, i.e., $m_0 = M_{\rm BH,0} + M_{\rm NS} = 1.35(Q+1)M_\odot$. In this initial setup, the binary merges after about three orbits.

We initially superimpose a poloidal or toroidal magnetic field confined in the neutron star. For the poloidal field case, following the previous work [43], the magnetic field is given in terms of the vector potential as

$$\begin{aligned} A_j &= \{-y_{\rm NS}\delta_j{}^x + x_{\rm NS}\delta_j{}^y\} \\ &\quad \times A_b \max(P/P_{\rm max} - 10^{-3}, 0)^2. \end{aligned} \tag{3.122}$$

For the toroidal field case, the vector potential is given as

$$\begin{aligned} A_j &= \{(x_{\rm NS}(z_{\rm NS}^2 - R_{\rm NS}^2))\delta_j{}^x + (y_{\rm NS}(z_{\rm NS}^2 - R_{\rm NS}^2))\delta_j{}^y \\ &\quad -(z_{\rm NS}(x_{\rm NS}^2 + y_{\rm NS}^2 - R_{\rm NS}^2))\delta_j{}^z\} \\ &\quad \times A_b(1 + \cos(r_{\rm NS}/0.95R_{\rm NS})) \\ &\quad\quad (r_{\rm NS} < 0.95R_{\rm NS}). \end{aligned} \tag{3.123}$$

Here, $(x_{\rm NS}, y_{\rm NS}, z_{\rm NS})$ denote the coordinates with respect to the neutron-star center (location of the maximum rest-mass density), $r_{\rm NS}$ is the radius with respect to the neutron-star center, and $R_{\rm NS}$ is the coordinate radius of the neutron-star. P is the pressure, $P_{\rm max}$ is the maximum pressure, and $j = x, y$, and z. A_b is a constant and is chosen so that the initial maximum magnetic-field strength $b_{0,\rm max}$ is 3×10^{15} G, 3×10^{16} G, or 5×10^{16} G. These values are chosen to obtain a strong magnetic field in the remnant disk formed after tidal disruption of the neutron star in a short timescale after the merger. The strong magnetic field is required to resolve the fastest growing mode of the magnetorotational instability (MRI) [75, 76] in the accretion disk with the limited grid resolution, because its wavelength is proportional to the magnetic-field strength. Although such strong fields are not realistic in orbiting neutron stars, the resulting turbulent state in the accretion disk established by the MRI is not likely to depend strongly on the initial magnetic-field strength.[1] Thus, it would be reasonable to suppose that the resulting strong magnetic field and turbulent state will be established even for the case that we start a simulation from a much weaker magnetic-field strength in the presence of a sufficient grid resolution. We also note that even with $b_{0,\rm max} = 5 \times 10^{16}$ G, the electromagnetic energy (of order 10^{49} erg) is much smaller than the internal energy and gravitational potential energy (of order 10^{53} erg) of the neutron star.

We only consider the magnetic field confined in the neutron star initially, and do not consider a pulsar-like dipole magnetic field extending to the outside of the neutron star. This is because only the magnetic field confined in the neutron star has a significant effect on the subsequent evolution of the system. In terms of the accretion disk evolution including the post-merger mass ejection, only the magnetic field in the disk, which originates from the magnetic field inside the neutron star, plays an important role. In terms of the magnetosphere formation, a dipolar magnetic field initially located outside the neutron star may be amplified linearly due to winding. However in the disk, the magnetic field is amplified exponentially by the MRI, and the amplified magnetic field flux is ejected from the disk to the polar region by the MRI dynamo and subsequently forms the magnetosphere of a high field strength. For the realistic initial magnetic-field strength lower than 10^{12} G, the magnetic field amplified by the MRI should dominantly come into play.

[1] That is, we implicitly assume that the magnetic-field strength would be increased by the MRI and a turbulent state would be eventually established even if we started a simulation from low magnetic-field strengths (as is often done in this research field). This is just an assumption, but the result of a simulation, which is started with a low magnetic-field strength, illustrates that this is likely to be indeed the case (see Chapter 5).

We do not consider the effect of the neutrino viscosity to the MRI supposing that the magnetic-field strength could be enhanced to be $\gtrsim 10^{14}$ G due to the rapid winding in the main region of the accretion disk (see Sec. 4.2) even if the early growth of the MRI is suppressed [116, 117].

Chapter 4

Result1: The overall evolution of the entire merger and post-merger stages

In this chapter, we describe the result of the seconds-long numerical-relativistic neutrino-radiation magnetohydrodynamics simulations for black hole-neutron star mergers. We clarified the entire merger process starting from the inspiral stage throughout the post-merger stage for the cases with the tidal disruption.

In this first attempt we perform 7 simulations changing the black-hole mass, value of $b_{0,\max}$, and grid resolution. DD2 EOS is adopted to model the neutron star. The poloidal magnetic field configuration is assumed in the neutron star initially. The parameters and quantities for the 7 models employed in this chapter are summarized in Table 4.1. Numerical simulations with the low-resolution setting are always performed for the duration of $\geq 1\,\mathrm{s}$. In particular, for $Q = 4$ models, the low-resolution simulations are performed for $\gtrsim 2\,\mathrm{s}$. On the other hand, the high-resolution simulations are performed only for $\lesssim 1\,\mathrm{s}$ because such simulations require an extremely high computational cost. However, as we show below, the results for the low-resolution runs are quantitatively similar to those for the corresponding high-resolution runs, and hence, we consider that a fair convergence is achieved even with the low-resolution runs.

4.1 Overview of the evolution

First, we summarize the entire merger process found in a seconds-long simulation presenting the result for model Q4B5L for which the system was evolved up to $\sim 2.1\,\mathrm{s}$. Figure 4.1 displays the snapshot for the rest-mass density, absolute value of the magnetic-field strength, electron fraction Y_e, and temperature T, respectively, on the x-z plane. The magnetic-field strength is defined by $b = (b_\mu b^\mu)^{1/2}$ and the temperature is shown by multiplying the Boltzmann's constant k and in units of MeV.

In the present choice of the dimensionless spin parameter for the black hole and the fairly large radius of the neutron star, the neutron star is tidally disrupted by the black hole before the binary reaches the innermost stable circular orbit both for $Q = 4$ and 6. During the tidal disruption process, the neutron-star matter located in the black-hole side falls into the black hole. Specifically, $\sim 80\%$ of the neutron-star matter falls into the black hole in a short timescale of a few ms. On the other hand, the neutron-star matter located distant from the black hole forms a one-armed spiral structure. Due to the subsequent

Table 4.1: Key parameters and quantities for the initial conditions together with the parameters of grid setup for our numerical simulations. $M_{\rm BH,0}$: the initial black-hole mass, $b_{0,\rm max}$: the initial maximum magnetic-field strength, Ω_0: the initial orbital angular velocity, $M_{\rm ADM,0}$: the initial ADM mass, $\Delta x_{i_{\rm max}}$: the grid spacing for the finest refinement level, L_1: the location of the outer boundaries along each axis, and the values of N and $i_{\rm max}$. For all the models, the neutron-star mass is $1.35M_\odot$ and the initial dimensionless black-hole spin is 0.75. Note that $M_{\rm ADM,0}$ is by $\sim 1\%$ smaller than $m_0 =$ (6.75 and $9.45M_\odot$ for $Q = 4$ and 6) because of the presence of the gravitational binding energy.

model name	$M_{\rm BH,0}$ $[M_\odot]$	$b_{0,\rm max}$ [G]	$m_0\Omega_0$	$M_{\rm ADM,0}$ $[M_\odot]$	$\Delta x_{i_{\rm max}}$ [m]	L_1 [km]	N	$i_{\rm max}$
Q4B5H	5.400	5×10^{16}	0.056	6.679	270	1.62×10^4	234	9
Q4B5L	5.400	5×10^{16}	0.056	6.679	400	1.74×10^4	170	9
Q4B3L	5.400	3×10^{16}	0.056	6.679	400	1.74×10^4	170	9
Q6B5H	8.100	5×10^{16}	0.064	9.368	270	3.90×10^4	282	10
Q6B5L	8.100	5×10^{16}	0.064	9.368	400	3.97×10^4	194	10
Q6B3H	8.100	3×10^{16}	0.064	9.368	270	3.90×10^4	282	10
Q6B3L	8.100	3×10^{16}	0.064	9.368	400	3.97×10^4	194	10

Table 4.2: The mass $M_{\rm BH}$ and the dimensionless spin parameter $\chi_{\rm BH}$ of the remnant black hole evaluated at $t = 100$ ms together with the gravitational-wave and neutrino energy emitted before $t = 100\,$ms, $E_{\rm GW}$ and E_ν, and the rest mass of the matter located outside the black hole at $t = 100\,$ms, $M_{>\rm AH,0.1}$. All the quantities related to the mass or energy are described in units of $M_\odot$ and $M_\odot c^2$.

model	$M_{\rm BH}$	$\chi_{\rm BH}$	$E_{\rm GW}$	E_ν	$M_{>\rm AH,0.1}$
Q4B5H	6.466	0.856	0.069	0.008	0.129
Q4B5L	6.400	0.838	0.066	0.008	0.135
Q4B3L	6.396	0.838	0.066	0.008	0.138
Q6B5H	9.145	0.837	0.117	0.007	0.097
Q6B5L	9.138	0.832	0.112	0.007	0.104
Q6B3H	9.145	0.838	0.117	0.007	0.097
Q6B3L	9.136	0.833	0.112	0.007	0.106

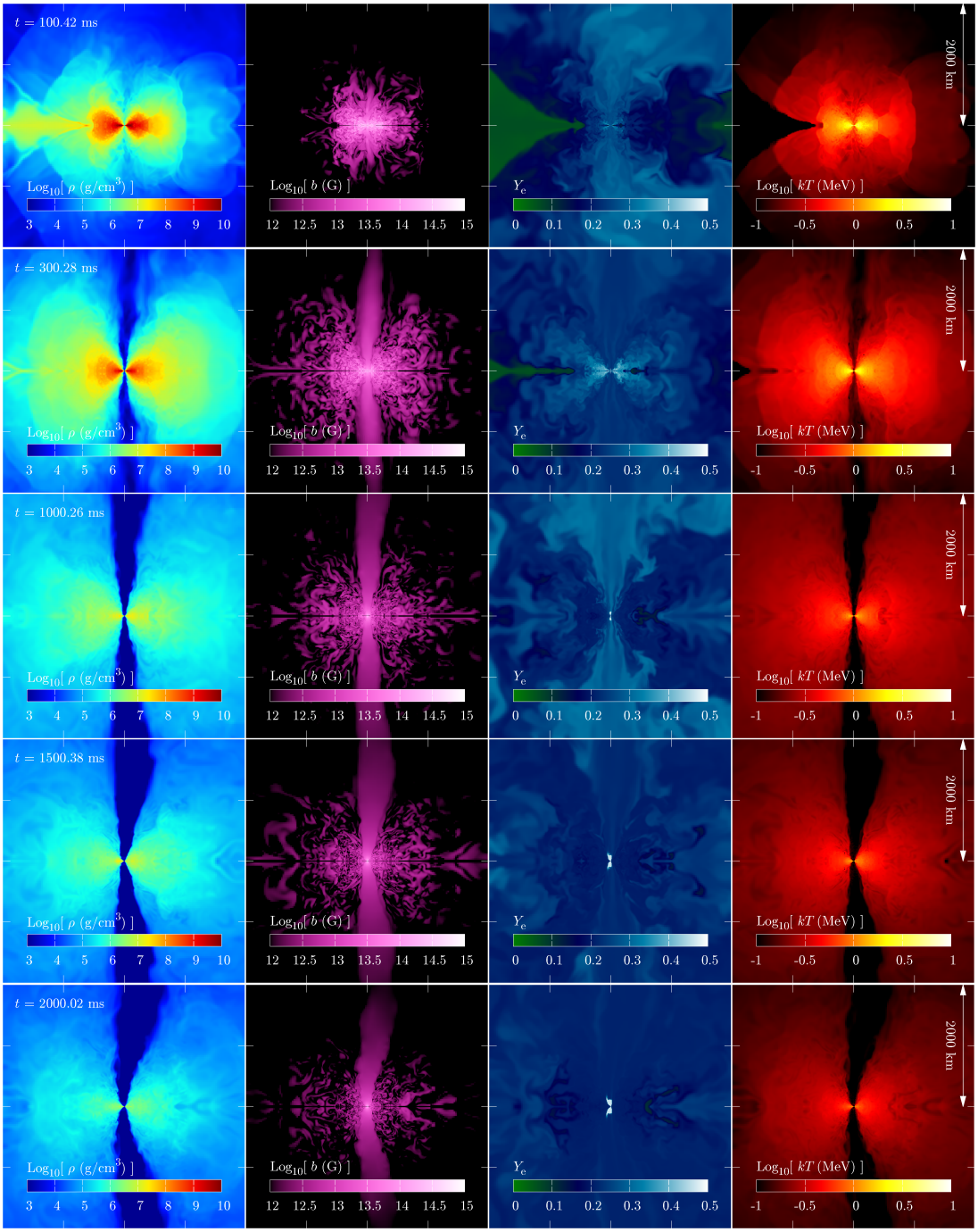

Figure 4.1: The snapshot for the rest-mass density ρ (g/cm^3), magnetic-field strength $b = \sqrt{b^\mu b_\mu}$ (G), electron fraction Y_e, and temperature T (kT in units of MeV) on the x-z plane with $[-2000$ km $: 2000$ km$]$ for both x and z at $t \approx 0.1$, 0.3, 1.0, 1.5, and 2.0 s for model Q4B5L. Note that the green region in Y_e found in the left side at the first and second rows shows the dynamical ejecta and fall-back matter. See also an animation: `https://www2.yukawa.kyoto-u.ac.jp/~kota.hayashi/Q4B5L-2000a.mp4`.

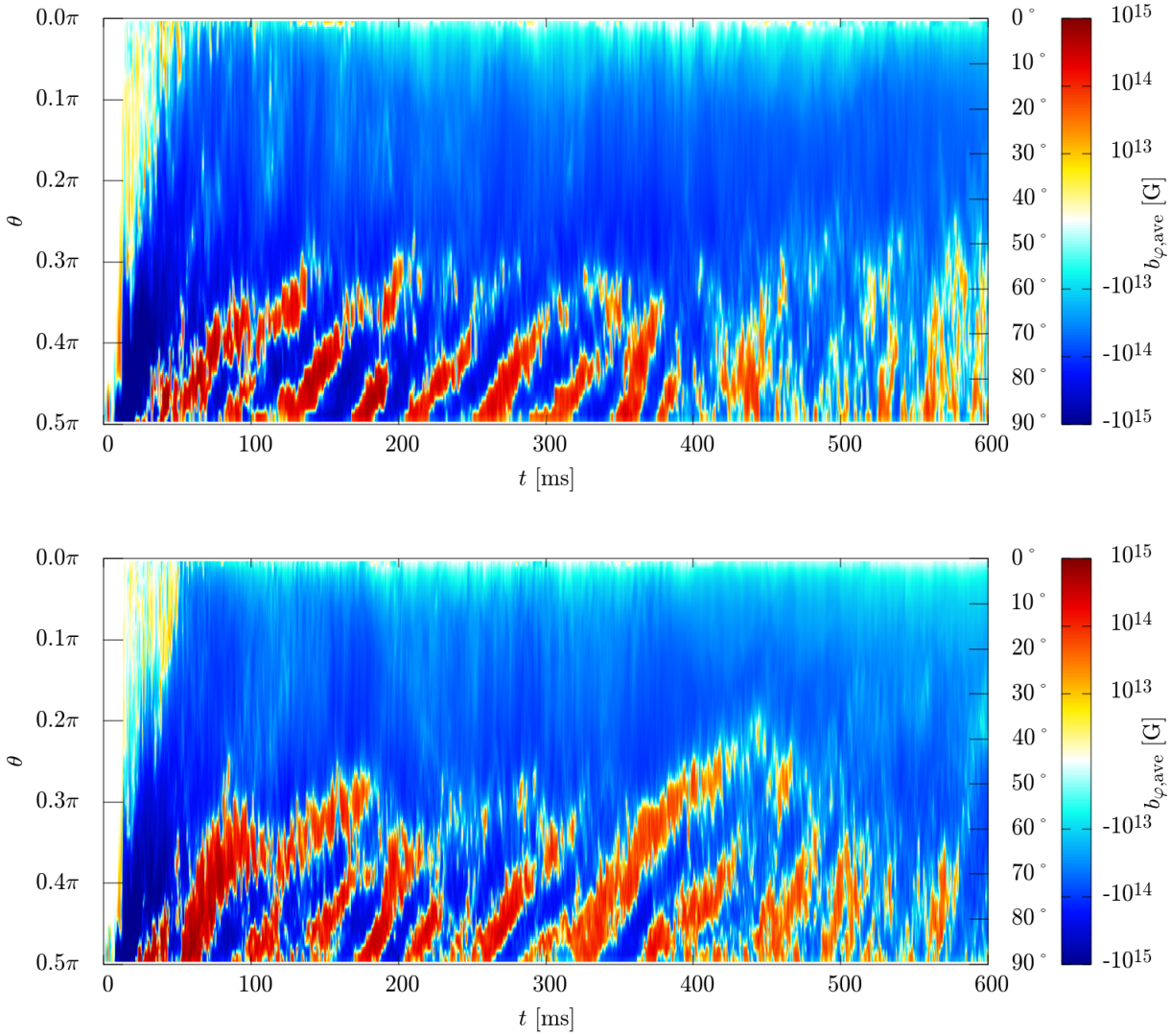

Figure 4.2: The profile of the average toroidal magnetic field along the polar direction (θ) at $r \approx 50$ km as a function of time for models Q4B5L (top panel) and Q4B5H (bottom panel).

angular-momentum transport inside the spiral arm and the dynamical evolution of the black-hole spacetime resulting from the matter infall into it, a part of the matter in the outer part of the spiral arm gains specific energy and angular momentum. The matter which gains sufficient specific energy eventually becomes dynamical ejecta, while the other part in the spiral arm which is bound to the remnant black hole forms an accretion disk. The timescale of this stage is $\lesssim 10$ ms (see the first row of Fig. 4.1 for the resulting state). All these processes have been studied by a number of previous numerical-relativity work (see e.g. Ref. [9] for a review) and our present result on the tidal disruption and disk formation processes is essentially the same as the previous findings.

The mass, $M_{\rm BH}$, and the dimensionless spin parameter, $\chi_{\rm BH}$, of the remnant black holes evaluated at $t = 100$ ms are summarized in Table 4.2. Irrespective of the runs, the black-hole mass and dimensionless spin are increased by $\approx 1.05 M_\odot$ and ~ 0.1, respectively, due to the matter infall. The black-hole mass is by $\sim 0.3 M_\odot$ smaller than the initial Arnowitt-Deser-Misner (ADM) mass. The reason for this is that a part of the neutron-star matter forms an accretion disk and ejecta, and in addition, gravitational waves and neutrinos carry away the energy (see Tables 4.1 and 4.2) in the inspiral and early merger stages.

We also list the total gravitational-wave and neutrino energy emitted before $t = 100$ ms, $E_{\rm GW}$ and E_ν, and the rest mass of the matter located outside the apparent horizon at $t = 100$ ms, $M_{>{\rm AH},0.1}$, in Table 4.2. By comparing $M_{\rm BH}$ and $M_{\rm ADM,0} - E_{\rm GW} - E_\nu - M_{>{\rm AH},0.1}$, we can assess how good (or bad) the energy conservation is satisfied in our simulation. It is found that for $Q = 4$, the energy conservation is satisfied with about 0.1% and 1.1% error for high- and low-resolution runs of $Q = 4$ model, and with $\ll 0.1\%$ and about 0.1% error for high- and low-resolution runs of $Q = 6$ model, respectively. The reason that the accuracy depends strongly on the grid resolution for $Q = 4$ (i.e., for the smaller black-hole mass) is that the accuracy for resolving the black hole depends strongly on it. This is found by taking a look at the value of the black-hole mass for $Q = 4$: For the low-resolution runs, the black-hole mass is underestimated. However, the error of $\lesssim 1\%$ at $t = 100$ ms is still in an acceptable level, indicating the reliability of the numerical results.

After the spiral arm winds around the black hole, a compact accretion disk is formed. The orbital period at the innermost region of the accretion disk is 1–2 ms. During the tidal disruption process, the neutron-star matter which eventually forms an accretion disk experiences a strong differential rotation stage in the spiral arm, and then, a toroidal magnetic field is developed from the initially poloidal magnetic field by winding. After the formation of the accretion disk, the winding continues to enhance the toroidal magnetic-field strength, in particular in the innermost region of the accretion disk. After the sufficient amplification of the magnetic-field strength, an outward expansion of the matter is driven toward the polar direction due to the enhanced magnetic pressure, and as a result, poloidal fields for which the strength is comparable to that of the toroidal fields are also generated. With these strong magnetic fields, the wavelength for the fastest growing mode of the axisymmetric MRI becomes

$$\lambda_{\rm MRI} = \frac{b_z}{\sqrt{4\pi\rho h + b^\mu b_\mu}} \frac{2\pi}{\Omega} \tag{4.1}$$

$$\sim 10 \text{ km} \left(\frac{b_z}{3\times 10^{14} \text{ G}}\right) \left(\frac{\rho}{10^{11} \text{ g/cm}^3}\right)^{-1/2} \left(\frac{\Omega}{2\times 10^3 \text{rad/s}}\right)^{-1}, \tag{4.2}$$

and can be numerically resolved. Here, Ω denotes the local angular velocity and z-direction is the direction of the rotation axis. Then, a turbulent state associated with the MRI is developed, and eventually, an MRI dynamo is activated in the accretion disk. This can be also observed from a spacetime diagram of the toroidal-field strength. In Fig. 4.2,

we plot the average value of the toroidal field as a function of time and polar angle $\theta = \tan^{-1}(\sqrt{x^2+y^2}/z)$ for models Q4B5L and Q4B5H. Here, x, y, and z are defined with respect to the black-hole center. The toroidal field is defined by $b_{\bar{\varphi}} = (xb_y - yb_x)/\sqrt{x^2+y^2}$. The average is performed with respect to the azimuthal angle $\varphi = \tan^{-1}(y/x)$ at the selected radius of $r := \sqrt{x^2+y^2+z^2} \approx 50\,\mathrm{km}$. From Fig. 4.2, we find the so-called butterfly structure [118] irrespective of the grid resolution: The polarity of the toroidal magnetic field is reversed due to the turbulent motion in a periodic manner with the period of ~ 20 local orbital periods ($\approx 2.5\,\mathrm{ms}$).[1] It is also found that strong magnetic-field regions move from the accretion disk to the polar region in the early stage, producing a global magnetic-field structure (see also the magnetic-field strength in the second row of Fig. 4.1).

During this turbulent stage, the angular momentum is transported from the inner to the outer region of the accretion disk due to the effective viscosity induced by the turbulence. In addition to this effectively viscous process, magnetohydrodynamics effects such as the magneto-centrifugal effect [119] which results from a global magnetic field could play an important role for expelling the matter from the central region. Due to these effects, the matter near the innermost stable circular orbit loses its angular momentum and falls into the black hole, while the matter in the outer part of the disk receives the angular momentum and expands gradually. As a result, the rest-mass density and the temperature in the disk decrease in the viscous timescale of order 100 ms to 1 s (see the third to fifth rows of Fig. 4.1).

In addition to the disk expansion toward the equatorial direction, the matter expands toward the direction perpendicular to the orbital plane (see the entire panels of Fig. 4.1). Our interpretation for this expansion is that the magnetic tower effect plays a role: During the evolution of the accretion disk, the toroidal magnetic-field strength is enhanced by the MRI and winding. As a result, the magnetic pressure is enhanced to be high enough for the accretion disk to expand toward the direction perpendicular to the orbital plane (and thus the disk becomes a torus), while the serious baryon contamination in the vicinity of the rotational axis is prevented by the centrifugal force of the matter. This effect produces a funnel structure around the rotational axis (see the second to fifth rows of Fig. 4.1).[2]

In spite of the enhanced magnetic-field strength, we do not find appreciable early-post-merger mass ejection associated with this enhancement within 100–200 ms after the onset of the merger. The absence of the clear early post-merger mass ejection agrees with some of the results found in Ref. [64] in which the initial magnetic-field profile is chosen to be toroidal or weakly poloidal. Only in several previous magnetohydrodynamics studies [61, 62, 64, 65] in which a strong poloidal magnetic field is given, the early post-merger mass ejection was found. In our simulations, the magnetic-field profile in the early stage of the post-merger evolution is primarily toroidal. Thus, we consider that the early post-merger mass ejection takes place only for the case that a strong poloidal field is present in the disk at the formation of the remnant disk, although our result indicates that such strong poloidal fields are not likely to be formed soon after the merger of black hole-neutron star binaries.

Not only the magnetohydrodynamics effect but also the neutrino cooling plays an

[1] After the post-merger mass ejection sets in at $t \sim 400\,\mathrm{ms}$ (cf. Sec. 4.2), the periodic butterfly diagram is not clearly observed. However, it is still seen that the polarity of the magnetic field changes with time due to the presence of the turbulent motion. The decrease of the toroidal magnetic-field strength is due to the disk expansion.

[2] In the late stage with $t \gtrsim 1.5\,\mathrm{s}$, the funnel has an asymmetric structure. This is caused by the fall-back of the matter in the tidal tail that is formed predominantly for the negative x direction at tidal disruption. This fall-back also lowers the electron fraction near the black hole in the late phase.

important role for the evolution of the accretion disk [56]. In the early stage of the accretion disk, the maximum density is $\gtrsim 10^{12}\,\mathrm{g/cm^3}$ and the maximum temperature is several MeV. In addition to the high density and high temperature, the disk is massive with the mass $\gtrsim 0.1 M_\odot$ in the early stage. In such a stage, neutrino luminosity becomes higher than $10^{53}\,\mathrm{erg/s}$ which is comparable to or higher than the viscous heating rate for a compact disk with a high viscous parameter [66]. During the stage that the neutrino luminosity is as high as the rate of the viscous heating (and the shock heating associated with the magnetohydrodynamical activity in the present context), the matter in the accretion disk is not affected significantly by the heating effect, although the accretion disk gradually expands due to the viscous/magnetohydrodynamics angular-momentum transport and magnetic pressure resulting from the enhanced magnetic-field strength. However, with the expansion, the density and temperature of the accretion disk decrease, and consequently, the neutrino luminosity sharply decreases because the neutrino emissivity is approximately proportional to T^6 [109]. As the neutrino luminosity drops below the heating rate due to the viscous and magnetohydrodynamics activities, neutrinos cannot efficiently carry away the thermal energy from the accretion disk and the thermal energy generated by the viscous/magnetohydrodynamics effect influences the evolution of the accretion disk. Specifically, convective motion of the matter at the innermost region of the disk, in which the viscous heating and shock heating are most efficient, is excited and blobs of the matter heated in the vicinity of the black hole are moved toward the outer region of the disk along the surface of the disk.[3] As a result, the matter in the outer part of the disk obtains the thermal energy and the heated matter eventually becomes unbound from the system to be the post-merger ejecta (cf. the second and third rows of Fig. 4.1). This mechanism is the same as that found in the previous viscous hydrodynamics simulations [56–58, 66] (see also Ref. [120]). This post-merger mass ejection continues from 0.2–0.3 s to $\sim$ 1 s after the merger (i.e., after the formation of the accretion disk). We note that in addition to this convective effect, purely magnetohydrodynamical effects such as magneto-centrifugal effect [119] could also play a role for the mass ejection.

In parallel with the accretion-disk evolution, a magnetosphere is developed in the low-density region near the rotational axis (see Fig. 4.1). For the merger of black hole-neutron star binaries that experience tidal disruption, such a low-density region is naturally developed because the matter is ejected primarily toward the equatorial direction. During the magnetohydrodynamics evolution of the accretion disk, a mass outflow toward the direction perpendicular to the equatorial plane is also driven by the activity of the accretion disk. However, the density in the vicinity of the rotation axis is still preserved to be low because of the presence of the centrifugal force on the injected matter. Thus the accretion of the matter into the black hole proceeds primarily from the innermost region of the disk. In ideal magnetohydrodynamics, the accretion of the matter accompanies the infall of the magnetic flux into the black hole. Although the magnetic field comoving with the infalling matter falls together into the black hole, the magnetic-field line located outside the black hole can expand toward the outer direction in particular along the rotational axis which has low matter density and low gas pressure (see Sec. 4.3). Such magnetic fields eventually develop a magnetosphere for which the magnetic-field lines are helical and nearly aligned with the rotational axis (except for the vicinity of the black hole). The magnetic pressure in such a region is lower than the gas pressure of the surrounding thick torus which is formed after the activity of the accretion disk is enhanced (see the second to fifth rows of

[3] See the following animation for the entropy per baryon (s/k) and for the convective activity: `https://www2.yukawa.kyoto-u.ac.jp/~kota.hayashi/Q4B5L-2000a.mp4`, and `https://www2.yukawa.kyoto-u.ac.jp/~kota.hayashi/Q4B5L_sent.mp4`.

Fig. 4.1). In other word, the size of the magnetosphere is determined by the structure of the thick torus.

The magnetic-field lines penetrate the black hole spinning rapidly with the dimensionless spin $\gtrsim 0.8$, and thus, the system can be subject to the Blandford-Znajek mechanism [72] by which the rotational kinetic energy of the black hole is converted to the outgoing Poynting flux. In the presence of the matter for which the rest-mass energy density is comparable to or larger than the electromagnetic energy density, the Poynting flux cannot propagate away efficiently. However, the density in the polar region decreases with time because the matter in the vicinity of the black hole falls into the black hole and a part of the matter is expelled by the magnetic pressure. Hence, eventually, electromagnetic waves generated by the Blandford-Znajek effect can propagate away (cf. the second to fifth rows of Fig. 4.1). If an efficient conversion of the electromagnetic energy to the kinetic energy of the matter occurs during the subsequent propagation, a gamma-ray burst jet may be launched. Since the magnetic field has a collimated structure, the electromagnetic emission is also collimated. This collimated emission continues as far as the gas pressure of the thick and dense torus confines the magnetosphere (see Sec. 4.3 for a discussion).

We note that the evolution processes described above are qualitatively universal irrespective of the black-hole mass, initial magnetic-field strength, and grid resolution employed. In the following subsections, we describe the quantitative details about the accretion disk evolution, mass ejection, and generation of strong Poynting flux in the magnetosphere separately.

4.2 The evolution of the accretion disk and post-merger mass ejection

4.2.1 Disk evolution and ejecta

In this subsection, we present the quantitative details on the evolution of the accretion disk and on the mass ejection. Figure 4.3 shows the rest mass of the matter located outside the apparent horizon $M_{>\rm AH}$ (dashed curves) and the accretion disk mass $M_{\rm disk}$ (solid curves) as functions of time. Figure 4.4 shows the rest mass of the unbound matter (ejecta) $M_{\rm eje}$ as a function of time. These quantities are defined by

$$M_{>\rm AH} := \int_{r>r_{\rm AH}} \rho_* d^3x + M_{\rm esc}, \tag{4.3}$$

$$M_{\rm eje} := \int_{-hu_t>h_{\rm min}, r>r_{\rm AH}} \rho_* d^3x + M_{\rm esc}, \tag{4.4}$$

$$M_{\rm disk} := M_{>\rm AH} - M_{\rm eje}, \tag{4.5}$$

where $r_{\rm AH}$ denotes the coordinate radius of the apparent horizon with the respect to the black-hole puncture. $M_{\rm esc}$ denotes the rest mass escaping from the computational domain, which is calculated from

$$\dot{M}_{\rm esc} := \oint \rho\sqrt{-g}u^i dS_i, \tag{4.6}$$

$$M_{\rm esc} := \int^t \dot{M}_{\rm esc} dt. \tag{4.7}$$

The surface integral is performed near the outer boundaries of the computational domain.

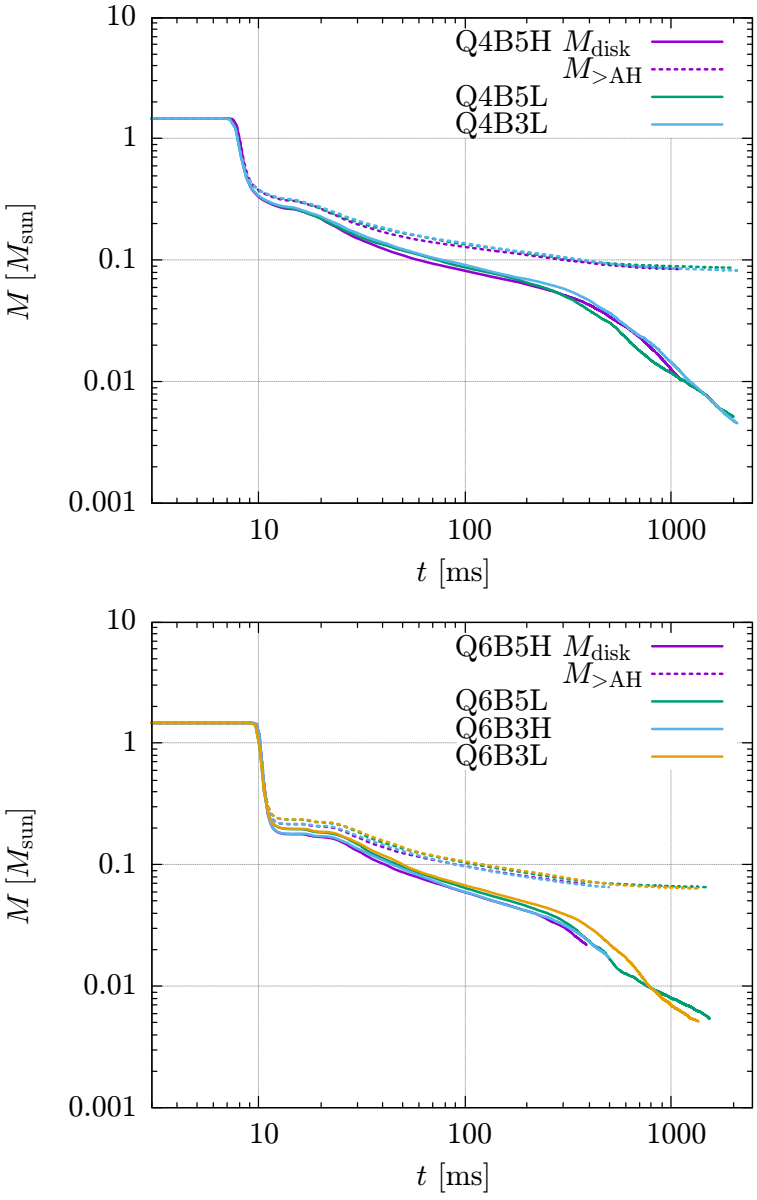

Figure 4.3: The time evolution of the rest mass of the matter located outside the apparent horizon (dashed curves) and the accretion-disk mass (solid curves) for all the runs with $Q = 4$ (top panel) and $Q = 6$ (bottom panel).

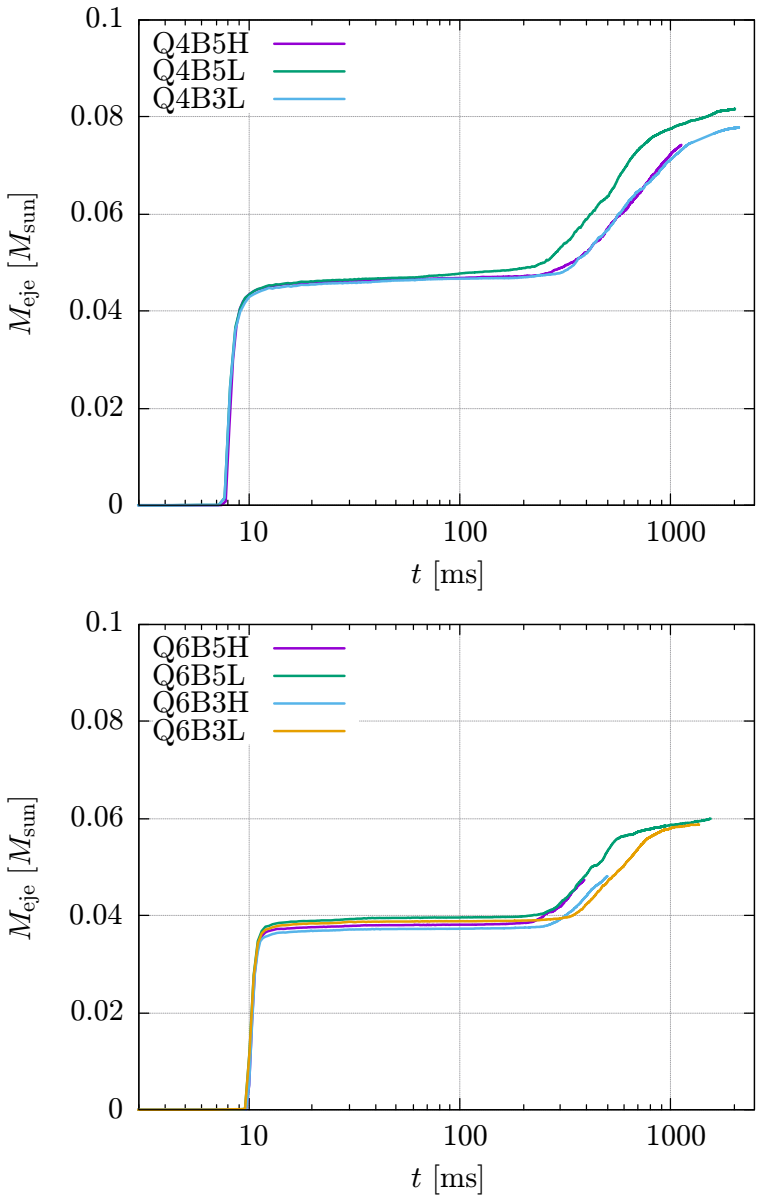

Figure 4.4: The time evolution of the rest mass of the unbound matter (ejecta) for all the runs with $Q = 4$ (top panel) and $Q = 6$ (bottom panel).

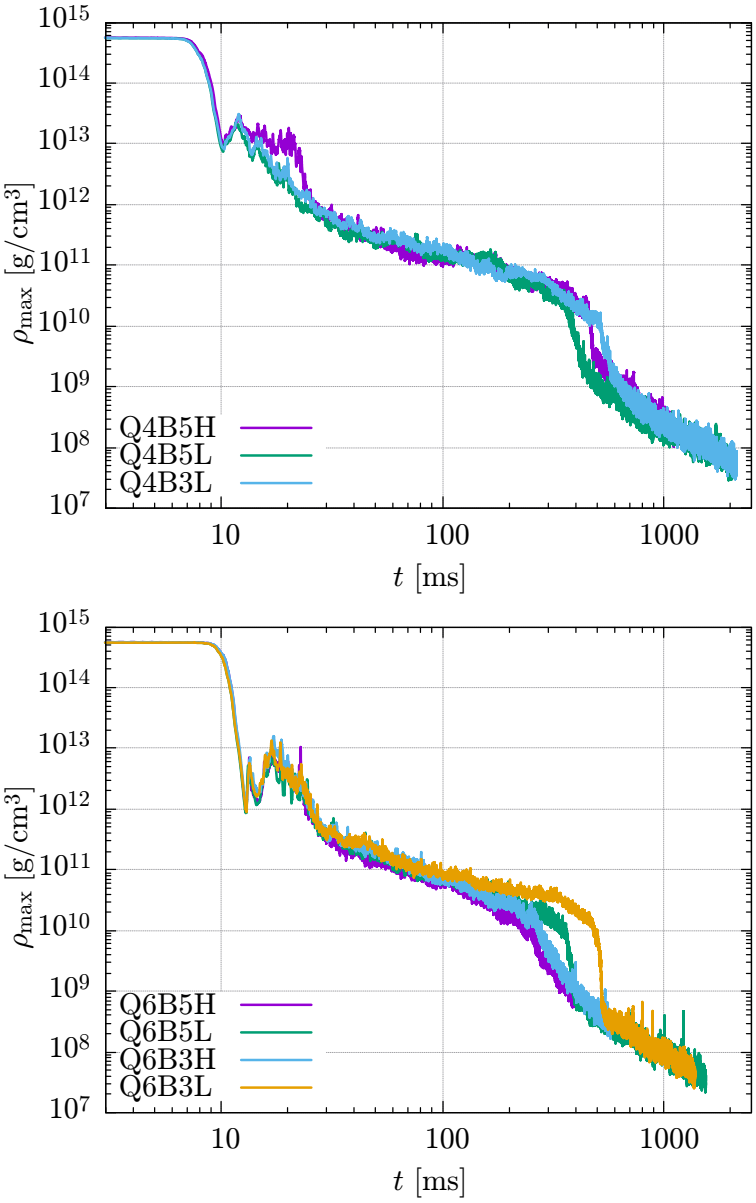

Figure 4.5: The time evolution of the maximum rest-mass density of the bound matter located outside the apparent horizon for all the runs with $Q = 4$ (top panel) and $Q = 6$ (bottom panel).

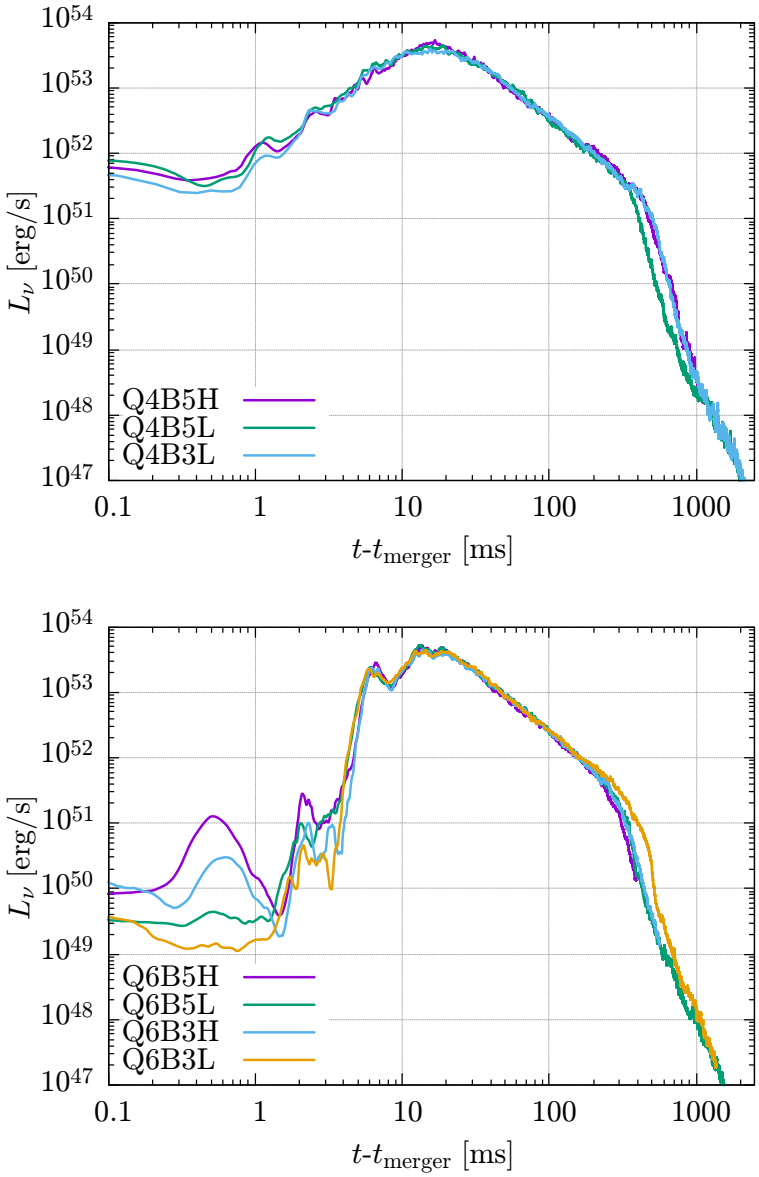

Figure 4.6: The time evolution of the total neutrino luminosity (sum of the luminosity for all the neutrino species) for all the runs with $Q = 4$ (top panel) and $Q = 6$ (bottom panel). The post-merger mass ejection sets in at $t - t_{\rm merger} \sim 300$–$500\,{\rm ms}$ at which $L_\nu \sim 10^{50}$–$10^{51.5}$ erg/s.

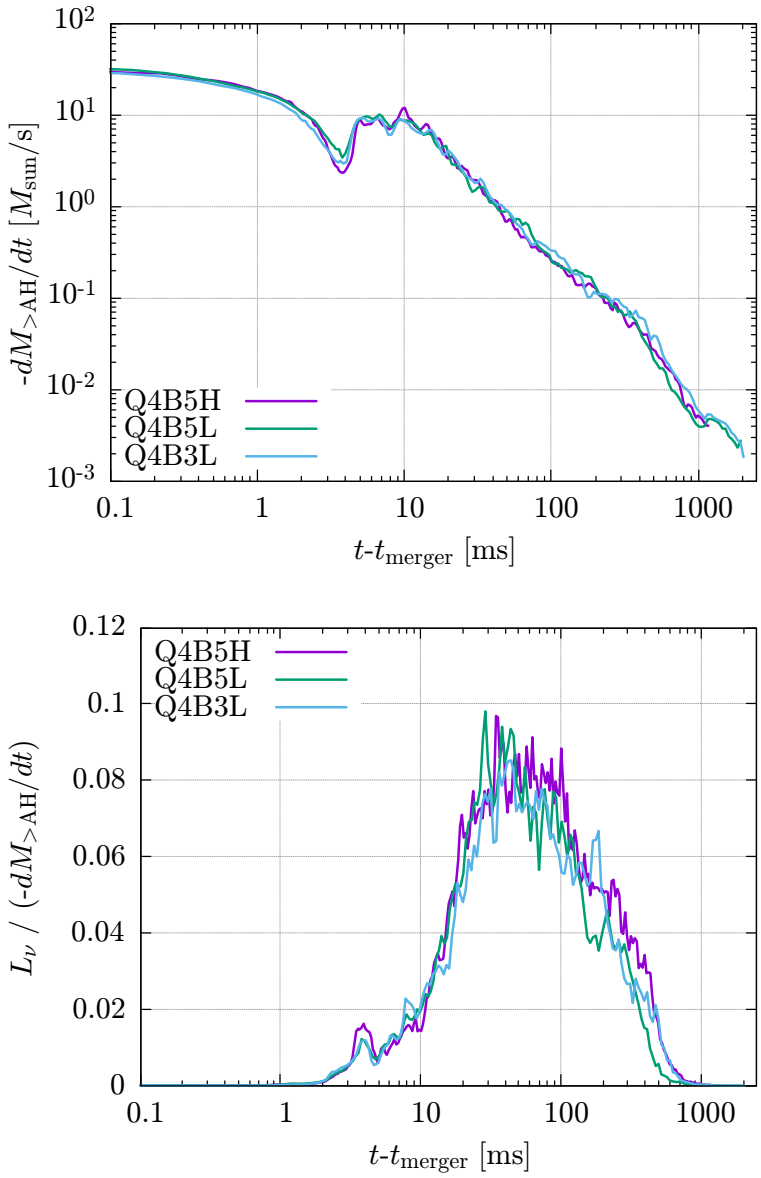

Figure 4.7: The time evolution of the rest-mass accretion rate calculated from $-dM_{>\mathrm{AH}}/dt$ (top panel), and the neutrino emission efficiency $L_\nu/(-dM_{>\mathrm{AH}}/dt)$ (bottom panel) for all the runs with $Q = 4$.

The ejecta component is identified by considering the Bernoulli criterion; i.e., we regard the matter located outside the apparent horizon that satisfies $hu_t < -h_{\rm min}$ as the unbound component. Here, $u_t(< 0)$ is the lower time component of the four velocity and h is the specific enthalpy. $h_{\rm min}$ is the minimum specific enthalpy for a given electron fraction $Y_{\rm e}$ and it is obtained from the tabulated EOS employed. The value of $M_{>\rm AH}$ for $t \lesssim 20\,$ms is in approximate agreement with that in Ref. [45] in which magnetohydrodynamics and resulting viscous effects were absent. In the present simulation, by contrast to the one in Ref. [45], for $t \gtrsim 20\,$ms, $M_{>\rm AH}$ continuously decreases due to the matter accretion onto the black hole induced by the angular-momentum transport resulting from the magnetohydrodynamics effects as already mentioned in Sec. 4.1. We note that the curves of $M_{>\rm AH}$ depend only weakly on the initial magnetic-field strength and grid resolution.

The value of $M_{\rm eje}$ steeply increases at two characteristic moments. The first increase is found right after the tidal disruption, and the steep increase continues only for a few ms, comparable to the dynamical timescale of the system. Thus, this mass ejection component is the dynamical ejecta. The rest mass for this component is $\approx 0.05 M_\odot$ and $\approx 0.04 M_\odot$ for models with $Q = 4$ and 6, respectively. The result for $Q = 4$ is in good agreement with the previous radiation-hydrodynamics result [45] because the magnetic-field strength is still weak at the tidal disruption, and hence, the magnetohydrodynamics effects play essentially no role in the dynamical mass ejection. After the steep increase, the value of $M_{\rm eje}$ remains approximately constant for the next few hundreds ms, reflecting that an efficient mass ejection activity is quiescent during this time. In this quiescent stage, however, the accretion disk is actively evolved due to the MRI and associated turbulent motion, and the density and temperature of the disk decrease (see, e.g., Fig. 4.5 for the rest-mass density) due to the expansion of the disk resulting from the angular-momentum transport process and enhanced magnetic pressure. As a result of the decrease in temperature, the neutrino luminosity eventually drops below the heating rate associated with the turbulent motion (cf. Fig. 4.6), and then, the post-merger mass ejection driven by the heating associated with the MRI turbulence sets in. Thus, the second steep increase of $M_{\rm eje}$ that starts at $t \sim$ 300–500 ms is triggered by the quick damping of the neutrino luminosity (see Fig. 4.6). We emphasize here that even in the presence of pure magnetohydrodynamics process (not effectively viscous process resulting from the MRI turbulence), the post-merger mass ejection appreciably occurs only after these onset time, and that, since the post-merger mass ejection continues for several hundred ms, simulations with the duration shorter than $\sim 500\,$ms cannot clarify this ejection process.

The rest mass of the post-merger ejecta is $\approx 0.035 M_\odot$ and $\approx 0.020 M_\odot$ for models with $Q = 4$ and 6, respectively, and these values are about 10% of the disk mass at its formation (at $t \sim 10\,$ms). For both $Q = 4$ and 6, the dynamical ejecta is the primary component of the ejecta in the present setting, and this tendency is stronger for the larger mass ratio, as discussed, e.g., in Refs. [36, 121]. The onset time of $t \sim$ 300–500 ms for the post-merger mass ejection depends on the initial magnetic-field strength and grid resolution by 100–200 ms. Our interpretation for this difference is that the magnetohydrodynamics turbulence is a stochastic process, and hence, the angular-momentum transport process can depend on the difference in the initial-field strength and grid resolution. However, the total ejecta mass and the properties of the post-merger ejecta do not depend strongly on them (see below for the electron fraction and velocity of the ejecta).

Figures 4.5 and 4.6 display the time evolution of the maximum rest-mass density $\rho_{\rm max}$ and the total neutrino luminosity L_ν, respectively. For generating Fig. 4.6, we define the merger time $t_{\rm merger}$ as the time at which the rest-mass density reaches its local minimum value for the first time; i.e., $t \approx 10$ and 13 ms for $Q = 4$ and 6, respectively. These figures

indeed show that the density and neutrino luminosity steeply decrease at $t \approx 300$–500 ms. This simultaneous decrease clearly elucidates that the evolution of the accretion disk and the timing of the post-merger mass ejection are controlled by the neutrino cooling. We also note that after the onset of the post-merger mass ejection, the accretion rate of the matter onto the black hole also decreases steeply with time: see the left panel of Fig. 4.7.

One interesting point is that the curve of L_ν well reflects the evolution of the accretion disk. From $t - t_{\rm merger} \approx 1$ ms to ~ 20 ms, L_ν increases by orders of magnitude both for $Q = 4$ and 6. This reflects the temperature increase during the formation of the accretion disk (e.g., due to the compressional heating and shock heating) and the subsequent enhancement of the turbulent state in the accretion disk due to the MRI (see, e.g., Fig. 4.8, which shows the increases of the electromagnetic energy in this stage). Subsequently, L_ν monotonically decreases for $t - t_{\rm merger} \gtrsim 20$ ms, because in this stage, the accretion disk expands due to the angular-momentum transport process and enhanced magnetic pressure, and the density and temperature decrease gradually. However, the thermal energy generated by the heating associated with the MRI turbulence is consumed primarily by neutrino cooling prior to the onset of the post-merger mass ejection. Hence, the expansion of the accretion disk does not rapidly proceed, and thus, the mass ejection due to the thermally generated energy is suppressed. It is found that L_ν decreases approximately as $t^{-1.6}$ in this stage, and the decrease is fairly mild. However, after L_ν decreases below $\approx 10^{51}$–$10^{51.5}$ erg/s as a result of the disk expansion and resulting decrease of the temperature, the neutrino emission rate becomes smaller than the thermal energy generation rate due to the MRI turbulence. Then, the turbulent heating is used for the outward expansion of the disk efficiently, in particular through the convective motion from the inner to outer region, and the post-merger mass ejection is driven. (We note that the critical neutrino luminosity, which is $\sim 10^{51}$–$10^{51.5}$ erg/s in the present case, should depend on the disk mass because the luminosity should be approximately proportional to it.) Subsequently, the neutrino luminosity exponentially drops at $t \approx 300$–500 ms irrespective of the binary mass ratio and the initial choice of the magnetic-field strength. Specifically, this post-merger mass ejection sets in when the temperature for most of the disk matter decreases below ~ 3 MeV (cf. the top panel of Fig. 4.11 for a mass distribution with respect to the temperature as a function of time). This critical temperature at the onset of the post-merger mass ejection is quantitatively the same as that found in general relativistic neutrino-radiation viscous hydrodynamics simulations of black hole-torus systems [66, 67]. However, the time at the onset of the post-merger mass ejection is earlier than that in the viscous hydrodynamics result for the similar black-hole mass cases [67]. As indicated in Refs. [58, 64, 71], the inherent magnetohydrodynamics effects such as magento-centrifugal effect [119] are likely to accelerate the mass ejection from the disk. The neutrino luminosity of $\approx 10^{51}$–$10^{51.5}$ erg/s at the onset of the post-merger mass ejection which we find is indeed similar to that found in the recent magnetohydrodynamics study [71].

Figure 4.7 plots the rest-mass accretion rate onto the black hole calculated by $-dM_{>\rm AH}/dt$ and a neutrino emission efficiency defined by $L_\nu/(-dM_{>\rm AH}/dt)$. After the early matter infall associated with the onset of the merger, the mass accretion rate has a peak at $t - t_{\rm merger} \sim 10$ ms. This is due to the fact that the magnetic-field strength is amplified in the accretion disk and the mass accretion rate is enhanced (cf. Fig. 4.8). After the peak, the mass accretion rate decreases monotonically with time approximately as $\propto t^{-2}$ for $t - t_{\rm merger} \lesssim 50$ ms and as $\propto t^{-1}$ in the subsequent stage before the onset of the post-merger mass ejection. After the onset of the post-merger mass ejection, the mass accretion rate drops more steeply. Broadly speaking, the curve of the neutrino emission efficiency reflects that of L_ν. However, the peak comes at $t - t_{\rm merger} \sim 40$–$50$ ms, which

is slightly later than the peak time of the neutrino luminosity and mass accretion rate. The reason for this is that $L_\nu \propto t^{-1.6}$ while $-dM_{>\rm AH}/dt \propto t^{-2}$ for $t - t_{\rm merger} \lesssim 50\,{\rm ms}$ and subsequently $-dM_{>\rm AH}/dt \propto t^{-1}$, and thus, the peak is shifted at $t - t_{\rm merger} \sim 50\,{\rm ms}$. The maximum neutrino emission efficiency is $\sim 8\%$–10%. Keeping the difference in the disk mass in mind, this value agrees broadly with those found in the previous viscous hydrodynamics simulations for similar black-hole mass ($M_{\rm BH} = 6M_\odot$) and dimensionless spin ($\chi_{\rm BH} = 0.8$) [67].

4.2.2 Magnetic-field evolution

Figures 4.8 and 4.9 show the time evolution of the electromagnetic energy, $E_{\rm B}$, and the ratio of the electromagnetic energy to the internal energy, $E_{\rm int}$, respectively. Here, $E_{\rm B}$ and $E_{\rm int}$ are defined, respectively, by

$$E_{\rm B} := \frac{1}{8\pi}\int_{r>r_{\rm AH}} u^t\sqrt{-g}\, b_\mu b^\mu d^3x, \tag{4.8}$$

$$E_{\rm int} := \int_{r>r_{\rm AH}} \rho_*\varepsilon d^3x, \tag{4.9}$$

and ε denotes the specific internal energy. Here we note that the energy-momentum tensor in the ideal magnetohydrodynamics is written as

$$\begin{aligned} T_{\mu\nu} &= \rho h u_\mu u_\nu + P g_{\mu\nu} \\ &+ \frac{1}{4\pi}\left(b^\alpha b_\alpha u_\mu u_\nu + \frac{1}{2}b^\alpha b_\alpha g_{\mu\nu} - b_\mu b_\nu\right), \end{aligned} \tag{4.10}$$

and with $h = c^2 + \varepsilon + P/\rho$, we have

$$u^t\sqrt{-g}T_{\mu\nu}u^\mu u^\nu = \rho_*(c^2+\varepsilon) + \frac{1}{8\pi}u^t\sqrt{-g}\, b^\mu b_\mu. \tag{4.11}$$

Here we recover c to clarify the physical units. Thus, the choice of $E_{\rm int}$ and $E_{\rm B}$ stems from Eq. (4.11).

During the merger stage, the magnetic-field strength in the accretion disk is amplified quickly in a short timescale of a few ms. This is initially induced by the magnetic winding associated with the differential rotation in the accretion disk. In the Keplerian disk with the presence of the poloidal magnetic field of the cylindrically radial component B^ϖ, the strength of the toriodal magnetic field B^T increases approximately linearly with time until a saturation as (e.g., Ref. [122])

$$B^T \approx \frac{3}{2}B^\varpi\Omega t, \tag{4.12}$$

where Ω denotes the local angular velocity. For a black hole with the dimensionless spin of 0.8, the angular velocity at the innermost stable circular orbit of the black hole is $\Omega_{\rm ISCO} \approx 0.174 M_{\rm BH}^{-1} \approx 5.43\times10^3 (M_{\rm BH}/6.5M_\odot)^{-1}\,{\rm rad/s}$ [123]. Thus for the models of $Q = 4$ and $Q = 6$, the matter near the innermost stable circular orbit rotates with the orbital period of ≈ 1.2 and 1.6 ms, respectively. This implies that in the first $\sim 10\,{\rm ms}$, the toroidal field strength can be ~ 60–80 times of B^ϖ, the maximum of which is $\sim 10^{14}\,{\rm G}$ at the formation of the accretion disk (i.e., much weaker than the field strength in the neutron star initially given) in the present simulations. This is the reason that the initial steep amplification to $E_{\rm B} > 10^{50}\,{\rm erg}$ is found in our present simulations. Because the winding timescale is quite short, the magnetic-field amplification by ~ 3 orders of magnitude in $\lesssim 100\,{\rm ms}$ is possible even in the absence of other instabilities such as MRI: Even for the

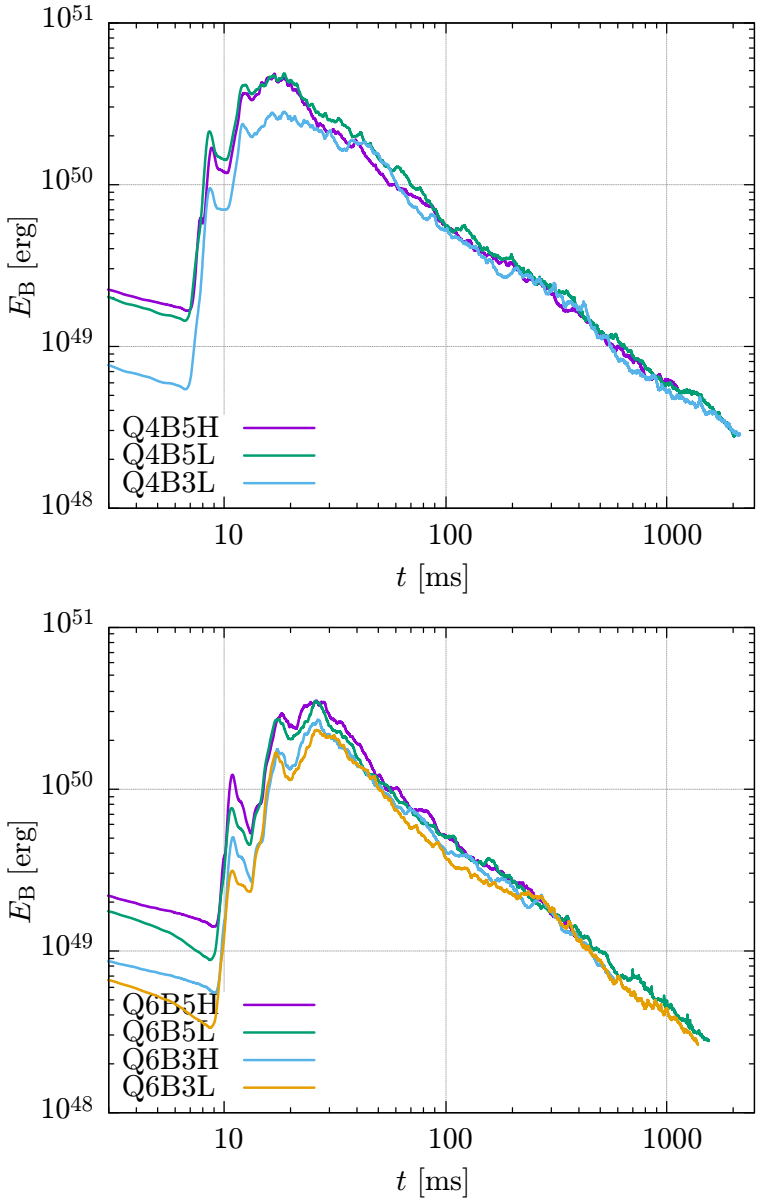

Figure 4.8: The time evolution of the electromagnetic energy evaluated for the outside of the apparent horizon for all the runs with $Q = 4$ (top panel) and $Q = 6$ (bottom panel)

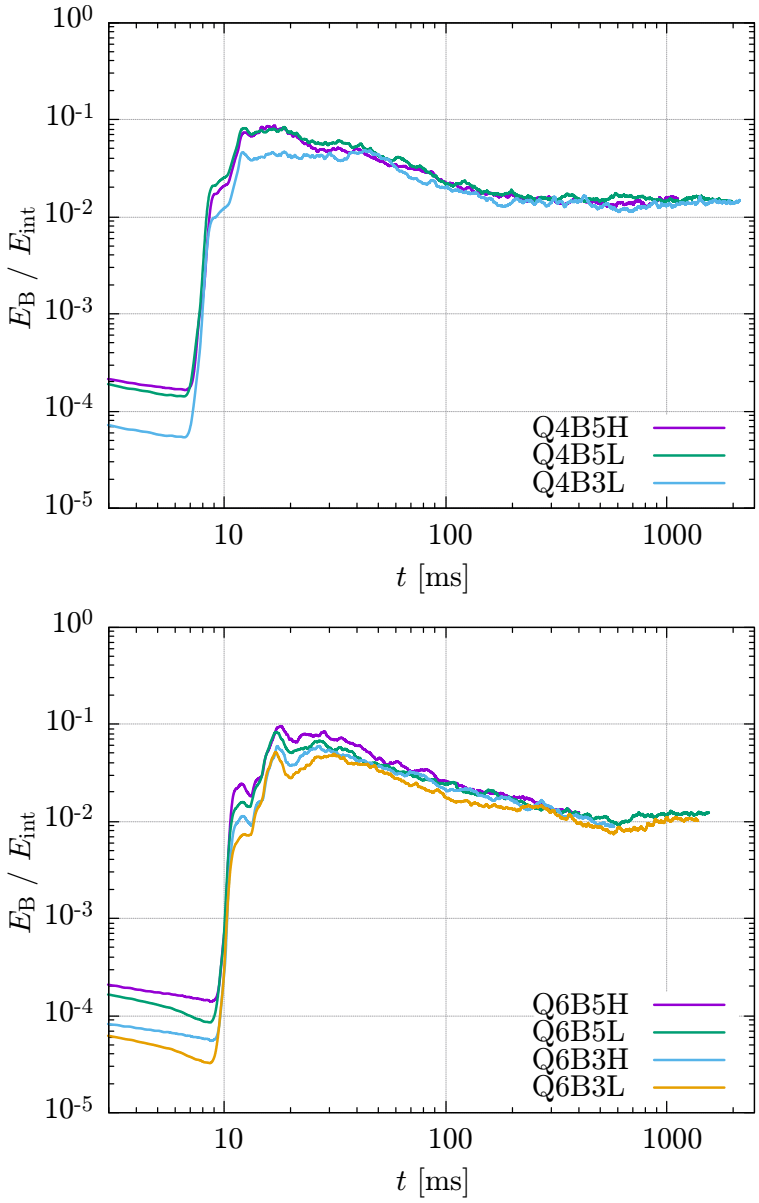

Figure 4.9: The time evolution of the ratio of the electromagnetic energy to the internal energy evaluated for the outside of the apparent horizon for all the runs with $Q = 4$ (top panel) and $Q = 6$ (bottom panel).

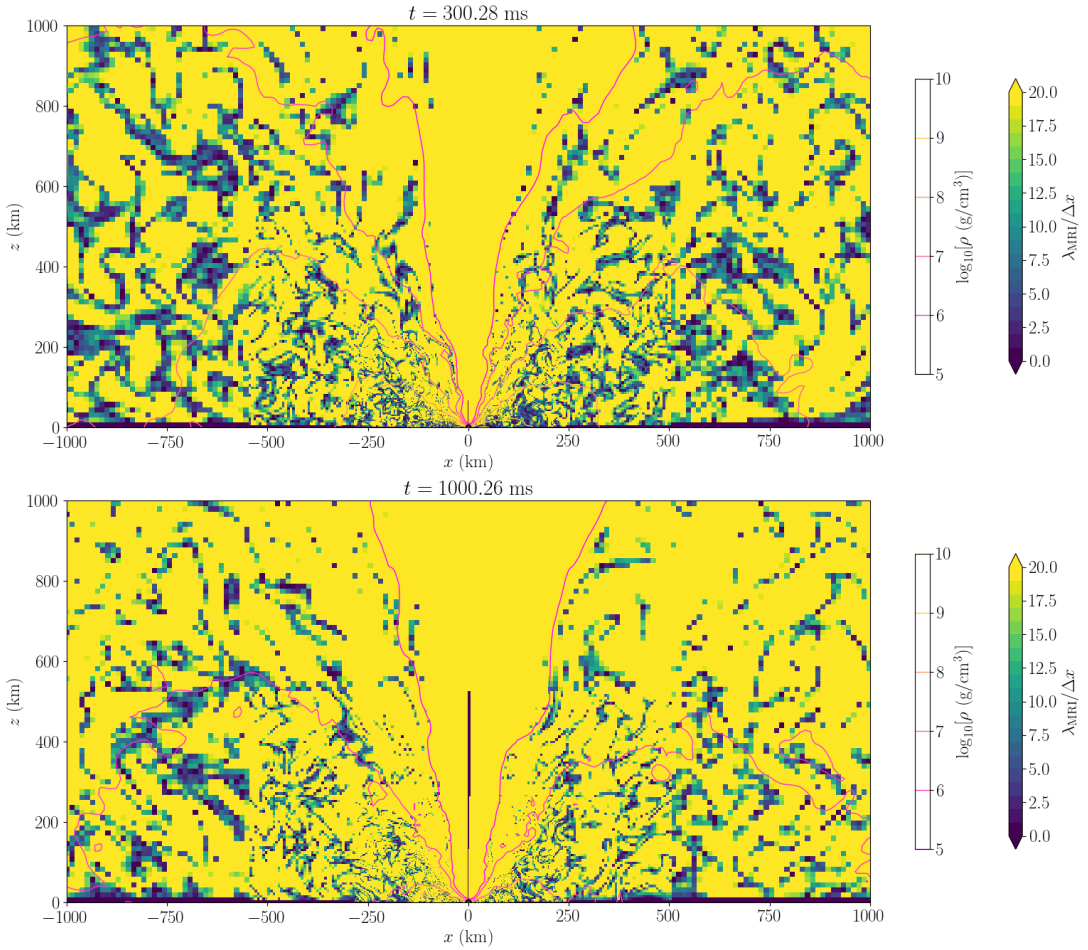

Figure 4.10: The snapshots of the MRI quality factor (color profile) together with the rest-mass density (contour) on the x-z plane at $t \approx 300$ and 1000 ms for model Q4B5L.

initial value of $B^{\varpi} = 10^{12}$ G, the toroidal field can be amplified to $\sim 10^{15}$ G in ~ 100 ms. After the sufficient amplification of the toroidal magnetic field, an outward expansion of the accretion disk is driven toward the polar direction due to the enhanced magnetic pressure and a poloidal field with its strength comparable to that of the toroidal field is also generated. In addition to the winding, the Kelvin-Helmholtz instability induced by the shear motion at the contact surfaces of the spiral arms also amplifies the magnetic-field strength.

After the initial amplification of the magnetic-field strength, the ratio of $E_{\rm B}/E_{\rm int}$ reaches ~ 0.05–0.1. Then, the magnetic-field growth is saturated. The electromagnetic energy at the saturation, $E_{\rm B,sat}$, is smaller for the smaller value of the initial magnetic-field strength. However, the relative difference in the saturated electromagnetic energy between models with different initial magnetic-field strengths is not as large as that in the initial electromagnetic energy. Furthermore, the electromagnetic energy for $t \gtrsim 30$ ms depends only weakly on the initial condition (as well as on the grid resolution). Thus, we infer that the amplification and saturation of the magnetic-field strength take place in a universal manner irrespective of the initial magnetic-field strength.

When reaching the saturation, the typical magnetic-field strength is 10^{15} G (cf. Fig. 4.2) and the maximum rest-mass density is $\sim 10^{11}$–10^{12} g/cm^3 in the innermost region. Thus the Alfvén velocity is $\approx b/\sqrt{4\pi\rho} \approx 9 \times 10^8\,{\rm cm/s}\,(b/10^{15}\,{\rm G})(\rho/10^{11}\,{\rm g\,cm^{-3}})^{-1/2}$ and the wavelength of the fastest growing mode of the MRI is typically ~ 10 km [76]. As a result, the wavelength of this unstable mode is covered by tens of grid points in our setting, and hence, the effect of the MRI comes into play subsequently. With the evolution of the disk, the typical magnetic-field strength and rest-mass density decrease, but in the equipartition stage (see below), the Alfvén velocity is always of order $\sqrt{E_{\rm B}/E_{\rm int}}(\sim 10\%)$ of the sound speed, which changes weakly with time. Thus, the wavelength of the fastest growing mode of the MRI is always covered by tens of grid points in the present setting. Figure 4.10 shows the snapshots of the MRI quality factor defined by $\lambda_{\rm MRI}/\Delta x$ on the x-z plane for model Q4B5L. We note that for other time slices, the similar feature is also found. Figure 4.10 shows that the fastest growing mode is covered by more than 20 grid points in the large portion of the disk even for the low-resolution run ($\lambda_{\rm MRI} \sim 10$ km in the inner region of the disk), and thus, we consider that the fastest growing mode of the MRI is resolved with a reasonable accuracy in the present work.

As a result of the viscous angular-momentum transport, the matter in the inner region of the accretion disk falls into the black hole while the matter in the outer part expands outward. Because of the matter infall into the black hole, the rest mass of the accretion disk decreases (see Fig. 4.3), and associated with the decrease in the rest mass, the electromagnetic energy decreases with time although the ratio of $E_{\rm B}/E_{\rm int} = O(10^{-2})$ is preserved. Thus, for $t \gtrsim 100$ ms, the accretion disk is in a quasi-steady equipartition state; the magnetic-field energy relaxes to $\sim 1\%$ of the internal energy irrespective of the mass and internal energy of the accretion disk. It is interesting to point out that the electromagnetic energy decreases approximately in proportion to t^{-1}. All these features are found both for the models of $Q = 4$ and $Q = 6$ irrespective of the initial magnetic-field strength and grid resolution.

4.2.3 Property of ejecta

Now we turn our attention to the properties of the ejecta. The bottom panel of Fig. 4.11 displays the mass distribution of the remnant matter with respect to the electron fraction $Y_{\rm e}$ for model Q4B5H. This shows that there are two characteristic peaks of $Y_{\rm e}$ at the regions around 0.05 and of 0.25–0.35, respectively. The former peak is associated primarily

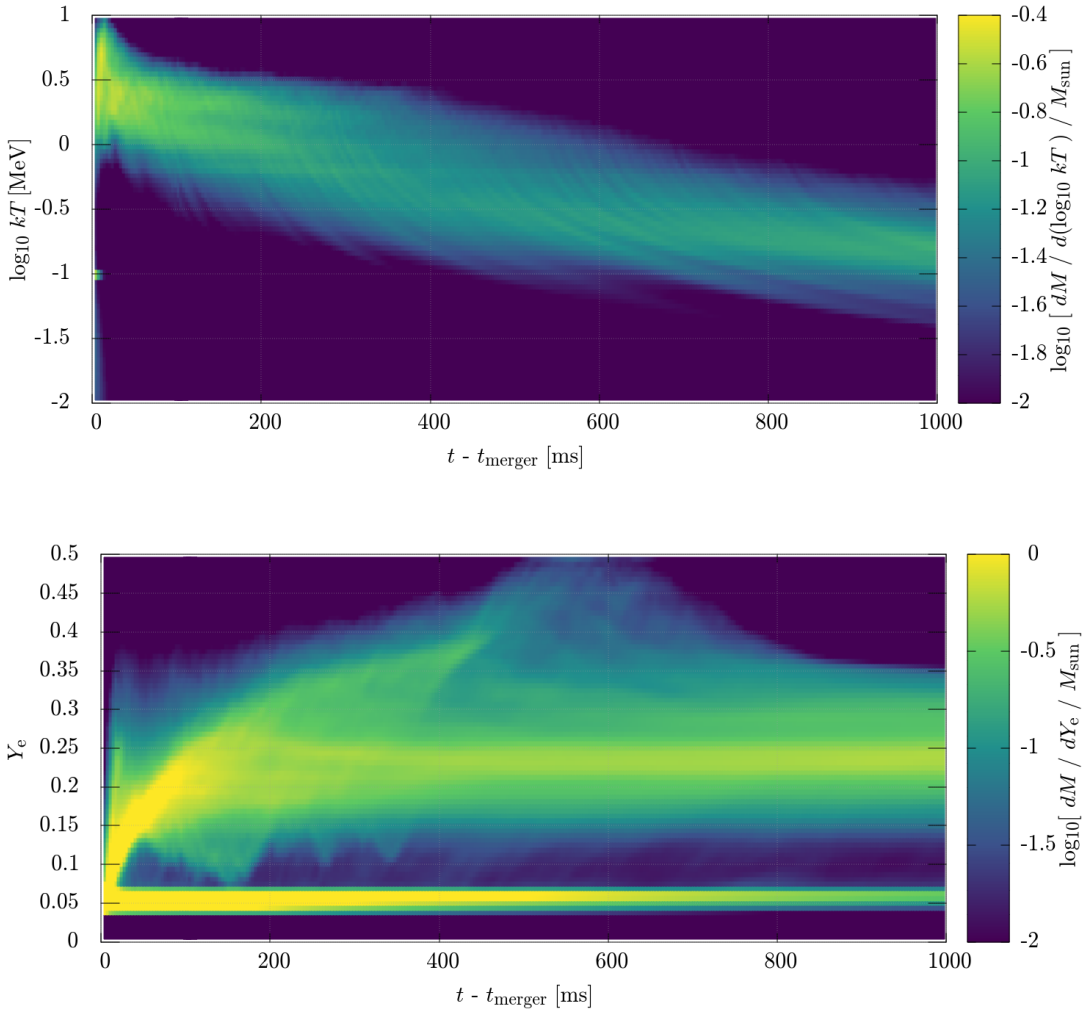

Figure 4.11: Time evolution of the mass histograms with respect to the temperature (upper panel) and electron fraction (lower panel) for model Q4B5H. The post-merger mass ejection sets in when the temperature for most of the matter decreases below 3 MeV at $t \sim 400\,\mathrm{ms}$ for this model. Note that the matter only in the computational domain is taken into account for plotting this figure, and thus, the matter which has escaped from the computational domain is neglected in the late stages. Thus, for $t \gtrsim 300$ ms, the dynamical ejecta mass decreases with time.

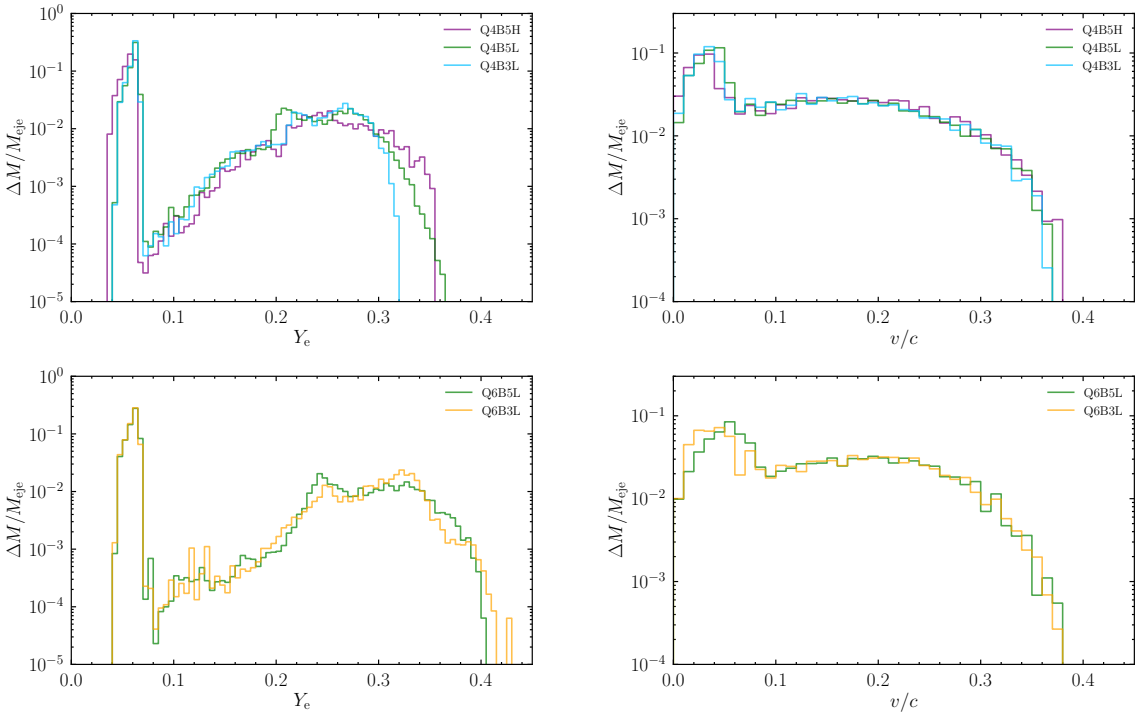

Figure 4.12: Mass histogram as functions of the electron fraction (left panels) and the velocity (right panels) of ejecta for the models with the simulation duration longer than 1 s (models Q4B5H, Q4B5L, Q4B3L, Q6B5L, and Q6B3L). Models with $Q = 4$ and $Q = 6$ are displayed in the upper and lower panels, respectively.

with the dynamical ejecta and the latter is with the accretion disk for $t \lesssim 400$ ms and post-merger ejecta for $t \gtrsim 400$ ms. This figure clearly shows that the dynamical ejecta component with $Y_e = 0.03$–0.07 comes directly from the neutron star, because the values are unchanged from the beginning. That is, this dynamical ejecta component is not essentially affected by thermal or weak-interaction processes in the merger and post-merger stages.

By contrast, the electron fraction of the post-merger ejecta is found to be determined by the evolution process of the accretion disk, in which the typical electron fraction increases from ~ 0.05 to ~ 0.25 for $0 < t \lesssim 200$ ms. As already mentioned, in this stage, the accretion disk gradually expands due to the viscous and magnetohydrodynamical angular-momentum transport and magnetic pressure by the amplified magnetic-field strength, and its rest-mass density and temperature monotonically decrease. In the disk with its optical depth to neutrinos $\lesssim 1$, the electron fraction is determined predominantly by the reaction equilibrium between electron/positron capture reactions if the temperature is high enough (typically $kT \gtrsim 2$–3 MeV; see Refs. [67, 70, 124]) for their timescale to be shorter than that of the disk expansion. Due to the disk expansion, the electron degeneracy becomes weak, and as a result, the electron fraction is shifted to higher values in the reaction equilibrium state. With the decrease of the temperature, the neutrino luminosity decreases approximately in proportion to T^6. As already mentioned, the post-merger mass ejection sets in when the neutrino luminosity drops below $\sim 10^{51}$–$10^{51.5}$ erg/s, which occurs for $t \gtrsim 300$ ms. The typical value of Y_e for the post-merger ejecta is determined around this timing, resulting in $Y_e \approx 0.25 \pm 0.10$.

Figure 4.12 displays the rest-mass histogram as functions of the electron fraction and velocity for the ejecta component for the models for which the simulation duration is longer than 1 s. The mass histogram is derived for the ejecta component outgoing from the radius of $\approx 10^4$ km. As described in the previous paragraphs, there are two distinct Y_e components for the ejecta, and this feature is clearly observed in Fig. 4.12. The dynamical ejecta component always has $Y_e \approx 0.03$–0.07 irrespective of the black-hole mass. By contrast, the distribution of Y_e for the post-merger ejecta component depends on the black-hole mass in the present results. Specifically, for larger black-hole mass, the value of Y_e tends to be larger. As a result, the peak of Y_e changes from ~ 0.25 for $Q = 4$ to ~ 0.31 for $Q = 6$. This tendency is in agreement with previous viscous hydrodynamics studies [67] (see also Refs. [69, 70]), and the reason is as follows: In the condition that the disk mass has an approximately identical value, the density of the disk can be higher for the lower black-hole mass (the lower mass ratio, Q, in the present context), because the tidally disrupted matter can have a more compact orbit around the black hole due to the smaller radius of its innermost stable circular orbit. Associated with this effect, the temperature is enhanced due to the compression and stronger shock heating, resulting in the higher neutrino emissivity and reducing the entropy per baryon of the matter in the accretion disk (cf. Fig. 4.6). With the lower entropy per baryon, the degree of the electron degeneracy becomes higher and the neutron-richness is enhanced. Therefore, for the lower black-hole mass, the electron fraction of the post-merger ejecta becomes slightly lower. Figure 4.12 shows that this effect is found irrespective of the initial-magnetic field strength and grid resolution (thus it is physical).

The right panels of Fig. 4.12 present the rest-mass histogram as a function of the ejecta velocity. The ejecta velocity v is defined by

$$\begin{aligned} v &:= \sqrt{1 - \Gamma_\infty^{-2}}, \\ \Gamma_\infty &:= -hu_t/h_{\rm min}, \end{aligned} \tag{4.13}$$

where Γ_∞ is interpreted as the terminal Lorentz factor under the assumption that the internal energy is converted completely to the kinetic energy of the ejecta in the far region. Again, there are two components. Here, the low-velocity component with $v/c \lesssim 0.08$ stems primarily from the post-merger ejecta, while the high-velocity component stems from the dynamical ejecta. We note that the velocity distribution for the dynamical ejecta is in good agreement with that in the previous study [45], and the typical velocity of the post-merger ejecta agrees approximately with that found in viscous hydrodynamics simulations (e.g., Refs. [66, 67]). As we reported in Ref. [36], the velocity of the dynamical ejecta is at highest $\sim 0.4c$. This is in contrast to the case of binary neutron star mergers in which the maximum ejecta velocity can be $\gtrsim 0.8c$ [125, 126].

Our present results confirm that there are two distinct ejecta components, low-Y_e and high-velocity component, and relatively-high-Y_e and low-velocity component, as many previous numerical work have suggested. By our self-consistent simulations, the distinction of two components emerges clearly. The former (dynamical ejecta) synthesizes heavy r-process elements, while the latter (post-merger ejecta) synthesizes relatively light r-process elements as well as heavy ones (e.g., Refs. [127]). Then, the former component is likely to shine as a red kilonova while the latter one is likely to contribute to a blue-kilonova component [57]. However, the detailed light curve and spectrum are determined by a non-trivial radiation transfer effect [128]. It is also likely that the light curve depends on the mass ratio Q. Thus, radiation transfer simulation is a topic to be explored as follow-up work.

4.3 Magnetic field in the funnel region and the relation to short gamma-ray bursts

In addition to aforementioned ejected matter (dynamical and post-merger ejecta), we find a launch of an outflow of the matter and Poynting flux in the narrow funnel region established near the rotational axis of the black hole (see Fig. 4.13). In particular, the isotropic-equivalent Poynting luminosity estimated for most of the runs is comparable to the typical luminosity of short-hard gamma-ray bursts [14, 15]. In this subsection, we discuss the quantitative details on this result.

Irrespective of the black-hole mass, initial magnetic-field strength, and grid resolution, tidal disruption of the neutron star takes place in our present setting and a magnetized accretion disk is formed around the central black hole. As already mentioned in the previous sections, the magnetic-field strength in the accretion disk is increased by the winding and MRI, and then, a turbulent state is established at $\sim$ 30–40 ms after the tidal disruption. Subsequently, the accretion disk evolves primarily due to the viscous effect stemming from the MRI turbulence. As already mentioned in the previous section, the magnetic-field strength is determined by an equipartition state, i.e., by the internal energy of the matter, which is typically ρc_s^2 where c_s is the sound speed of order 10^9 cm/s in the dense region of the disk. Since E_B/E_{int} is of $O(10^{-2})$, the magnetic-field strength can be approximated as $\sim 0.1\sqrt{8\pi\rho c_s^2} \sim 5 \times 10^{14} (\rho/10^{12}\,\mathrm{g\,cm^{-3}})^{1/2} (c_s/10^9\,\mathrm{cm\,s^{-1}})$ G near the inner edge of the accretion disk. The order of this field strength is indeed found in the accretion disk (see, e.g., Fig. 4.2). By the angular-momentum transport, the matter in the innermost part of the accretion disk falls continuously into the black hole, and in this infall, the magnetic fluxes also fall in. As a result, the poloidal magnetic-field lines for which the field strength is $\gtrsim 10^{14}$ G at the horizon penetrate the black hole. Here, the infall magnetic fluxes do not have aligned polarity because the accretion process is determined by the turbulence in the accretion disk, and hence, the magnetic-field strength

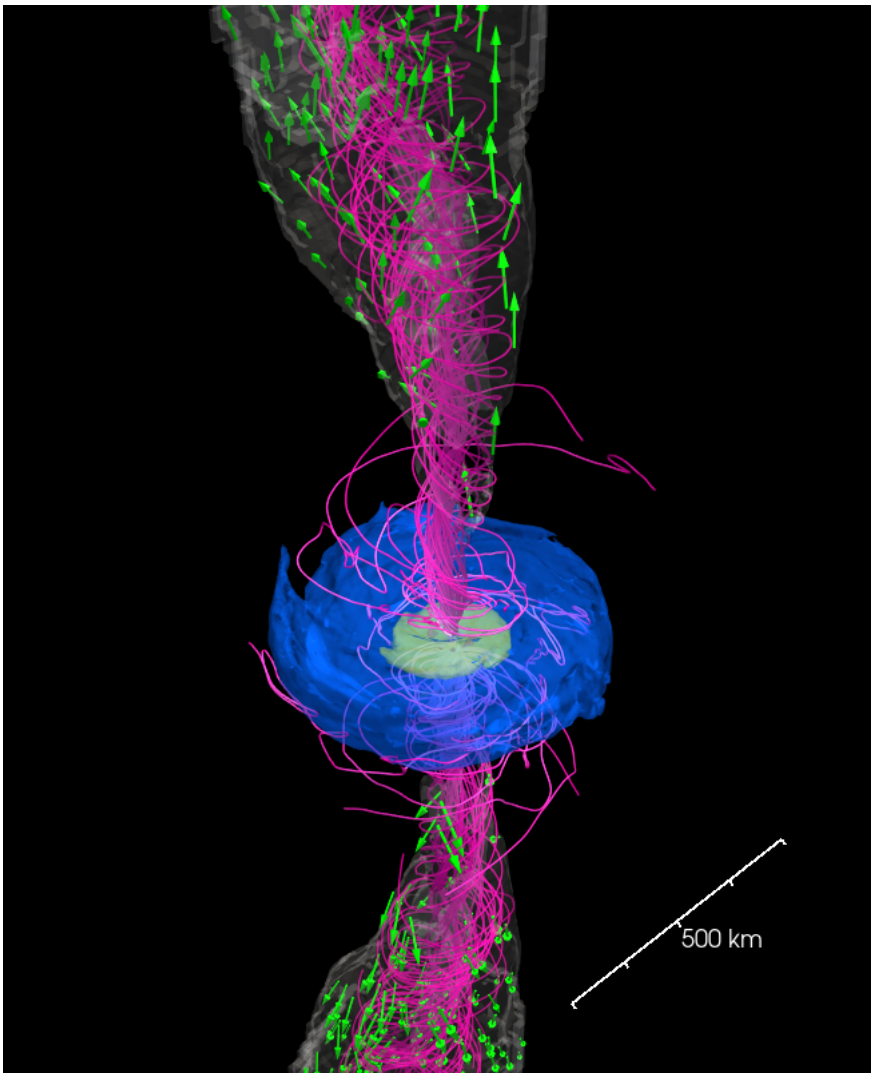

Figure 4.13: Snapshots of the rest-mass density profile (blue and green contours) with the magnetic-field lines (pink curves), unbound matter (white color) and its velocity (green arrow) for model Q4B5L at $t = 300\,\mathrm{ms}$. Magnetic-field lines penetrating the black-hole horizon are displayed. See also the following link for the time evolution: `https://www2.yukawa.kyoto-u.ac.jp/~kota.hayashi/Q4B5L-3D.mp4`

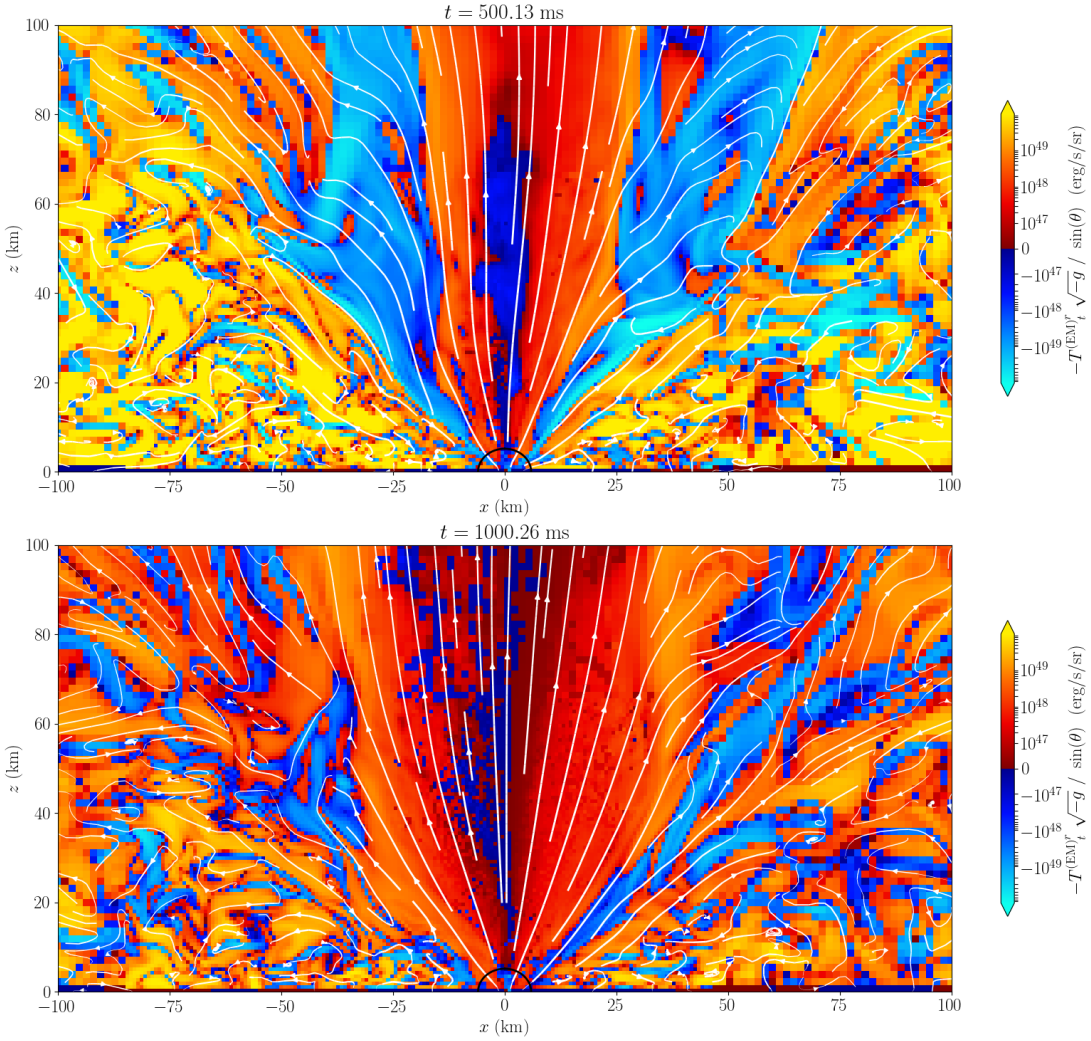

Figure 4.14: The snapshots of the outgoing Poynting flux per steradian (color profile) together with poloidal magnetic-field lines (white curves) near the apparent horizon on the x–z plane at $t \approx 500$ and 1000 ms for model Q4B5L. The apparent horizon is shown with the black circle.

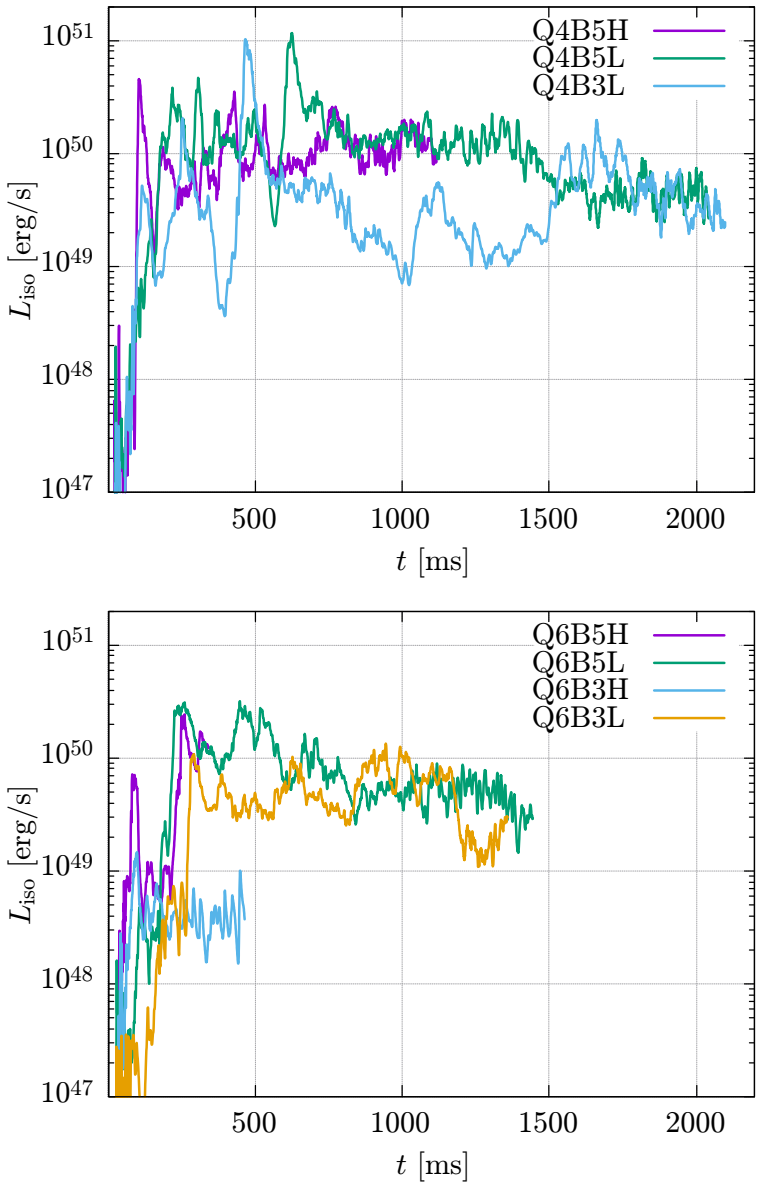

Figure 4.15: $L_{\rm iso}$ as a function of time for all the runs with $Q = 4$ (top panel) and 6 (bottom panel). The Poynting luminosity is evaluated at $r \approx 1500$ km for all the runs.

on the horizon does not monotonically increase. On the other hand, the poloidal magnetic fields in the polar region are twisted by the black-hole spin, and hence, the field strength could be larger than that for the accretion disk in the presence of a rapidly spinning black hole. Due to the twisting associated with the black-hole spin, the toroidal magnetic-field strength dominates over the poloidal one in the vicinity of the black hole (cf. Fig. 4.13).

However, such amplified magnetic fields do not immediately form a global magnetosphere. The reason for this is that at tidal disruption, a dense atmosphere ($\rho \sim 10^7$ g/cm^3) is formed in the polar region by the matter expelled by shocks generated during the winding and shock heating in the spiral arm. The matter also comes from the accretion disk due to its turbulent activity. Although a part of the matter in the polar region near the black hole eventually falls into the black hole, a certain fraction of the matter has to be expelled by the magnetic force to form a low-density magnetosphere. For this, the toroidal magnetic field amplified by the twisting due to the black-hole spin plays an important role, because a tower-like outflow is driven from the neighborhood of the black hole by this magnetic effect [47]. Hence, eventually, the matter energy density decreases below the magnetic energy density of $b^2/8\pi$ in the polar region of the black hole. This is satisfied for $\rho < b^2/8\pi c^2 = 4.4 \times 10^5 (b/10^{14}\,\mathrm{G})^2\,\mathrm{g/cm^3}$. Then, the magnetic pressure pushes the matter toward the outward direction along the rotation axis, establishing a low-density region near the rotational axis. During this process, the magnetic-field lines also expand outwardly, and a large-scale magnetosphere near the rotational axis is formed. In this region, the poloidal field is dominant (see Fig. 4.13). As a result, the rest-mass density decreases in the black-hole polar region, leading to the formation of the so-called funnel structure. At the funnel wall, the magnetic pressure is lower than the gas pressure of the surrounding thick torus and envelope, and hence, the magnetosphere is sustained by the surrounding matter.

Inside the funnel wall, the electromagnetic energy dominates over the rest-mass energy, and thus, an approximately force-free magnetosphere is formed. Here, the typical ratio of the electromagnetic energy density to the rest-mass energy density is 10–100. In such a region, the rotational kinetic energy of the black hole is extracted by the Blandford-Znajek mechanism [72] and transformed into the Poynting flux which propagates outward. Figure 4.14 shows the snapshots for an outgoing Poynting flux per steradian near the apparent horizon defined by $-T^{(\mathrm{EM})}{}_t{}^r \sqrt{-g}/\sin\theta$. Along the poloidal magnetic-field line, the outgoing Poynting flux is distributed from the apparent horizon to the mangnetosphere around the rotational axis of the black hole. This indicates that energy is extracted from the black hole through the magnetic field, and thus, we can interpret that the Blandford-Znajek mechanism is in operation. In addition, we find that the total Poynting luminosity on the apparent horizon is $\sim 10^{49}\,\mathrm{erg/s}$. This value is consistent with the luminosity expected from the formula for the Blandford-Znajek mechanism [72] for the resultant values of the magnetic-field strength, black-hole mass, and spin.

Figure 4.15 shows the time evolution of L_{iso}: an isotropic-equivalent Poynting luminosity, which we define using the Poynting luminosity for $\theta < 10^\circ$ and $r \approx 1500\,\mathrm{km}$ as

$$L_{\mathrm{iso}} := \frac{2}{1-\cos(10^\circ)} L_{\theta<10^\circ, r\approx 1500\,\mathrm{km}}, \tag{4.14}$$

where

$$L_{\theta<10^\circ, r\approx 1500\,\mathrm{km}} := -\int_{\theta<10^\circ, r\approx 1500\,\mathrm{km}} T^{(\mathrm{EM})}{}_t{}^r \sqrt{-g} dS_r. \tag{4.15}$$

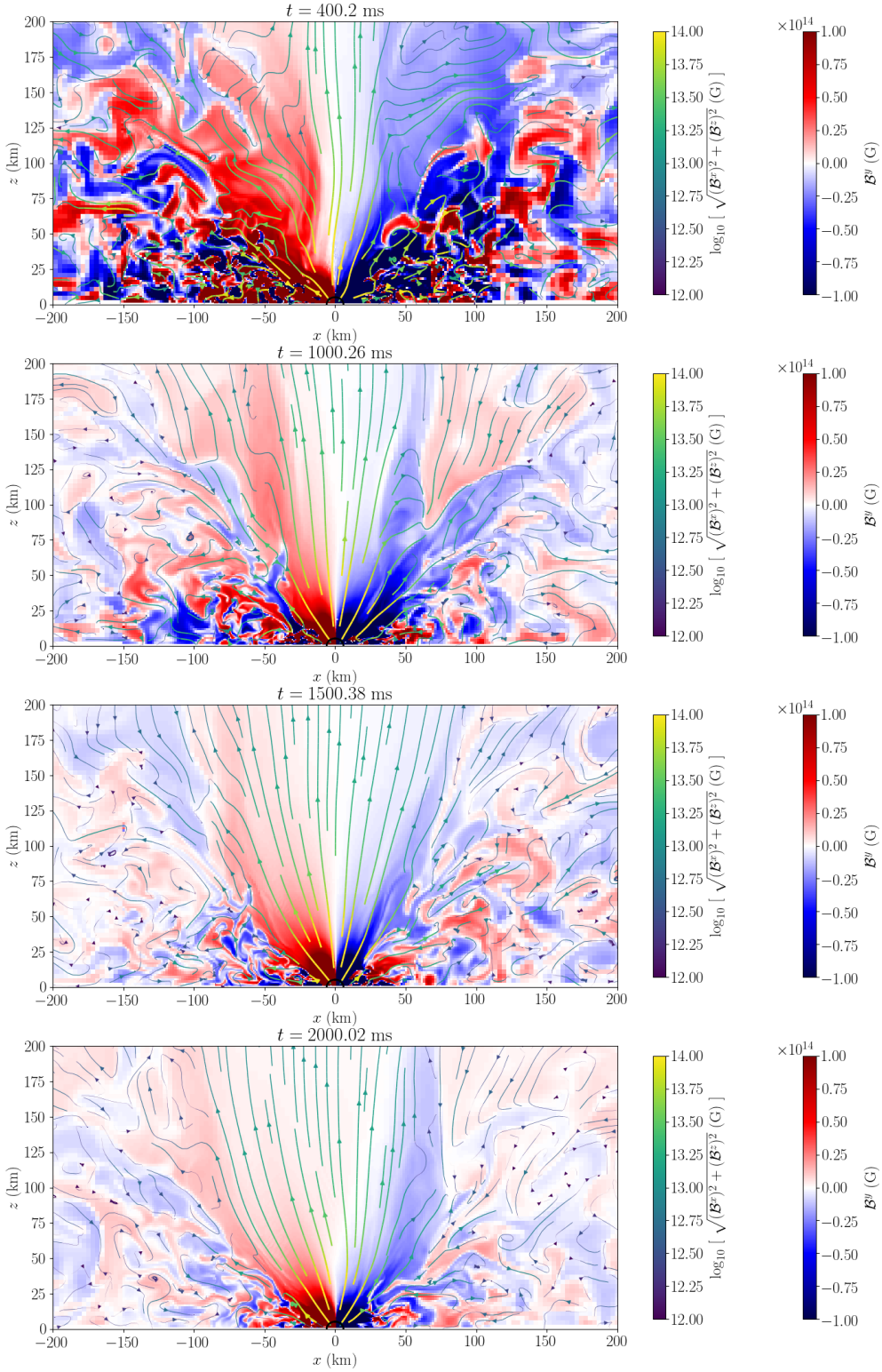

Figure 4.16: The snapshot of the toroidal magnetic field (color profile) together with the poloidal magnetic-field lines (curves) on the x-z plane at selected time slices for model Q4B5L. See also the following link for an animation: `https://www2.yukawa.kyoto-u.ac.jp/~kota.hayashi/Q4B5L-mf.mp4`

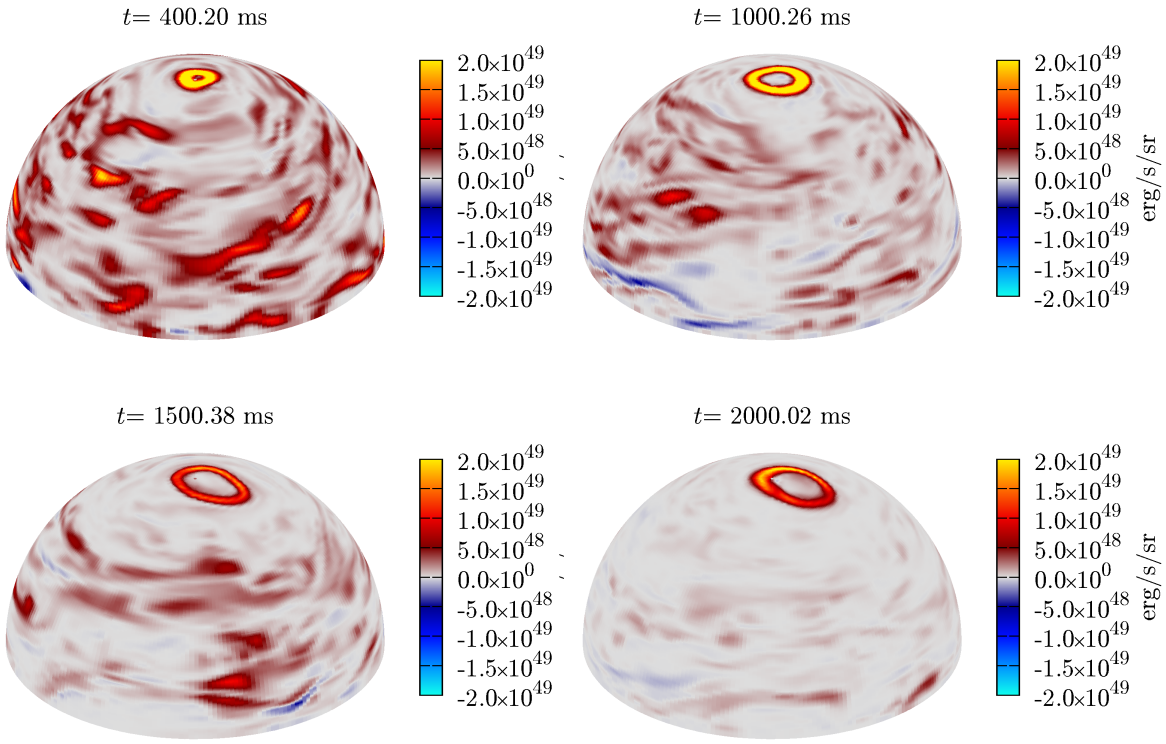

Figure 4.17: The angular distribution of the Poynting flux per steradian on a sphere of $r \approx 1500\,\mathrm{km}$ for model Q4B5L at selected time slices. The bright color displayed in the polar region stems from the Blandford-Znajek effect, while for other regions, the magnetic fields accompanying with the outflowing matter contribute mainly to the Poynting flux. The opening angle of the Poynting flux in the polar region is shown to increase with time. See the following link for an animation: `https://www2.yukawa.kyoto-u.ac.jp/~kota.hayashi/Q4B5L-f3D.mp4`

$T^{(\mathrm{EM})}_{\mu\nu}$ denotes the electromagnetic part of the energy-momentum tensor. We here choose a particular value (10°) for the surface integral because the opening angle of the funnel region is initially as narrow as $\sim 10°$ (see Figs. 4.16 and 4.17). We always assume an observer located along the z-axis for evaluating $L_{\rm iso}$.

Figure 4.15 shows that the typical maximum value of $L_{\rm iso}$ is of order $10^{50}\,{\rm erg/s}$ and $L_{\rm iso}$ varies with time irrespective of the black-hole mass and initial magnetic-field strength. This varying isotropic-equivalent luminosity together with the opening angle of $\theta \sim 10°$ (cf. Fig. 4.17) is in a fair agreement with those for short-hard gamma-ray bursts in the assumption that the conversion efficiency of the Poynting flux to the gamma-ray radiation is sufficiently high (i.e., close to unity) [14, 15].[4]

The stage with a high value of $L_{\rm iso} \gtrsim 10^{50}\,{\rm erg/s}$ continues broadly for $\sim 1\,{\rm s}$. Subsequently, the isotropic-equivalent luminosity starts decreasing. This is due to the fact that the opening angle of the funnel region increases and the magnetic-flux density is reduced. Remember that the funnel region is determined by the gas pressure of the thick torus at the funnel wall. In the long-term evolution of the accretion torus, the rest-mass density and associated gas pressure around the funnel wall decrease with time due to the post-merger mass ejection. On the other hand, the total magnetic flux penetrating the black hole does not significantly decrease in the ideal magnetohydrodynamics, and thus, the decrease in the magnetic pressure is not as significant as the gas pressure at the funnel wall. As the rest-mass density decreases, thus, the magnetic pressure exceeds the gas pressure at the original position of the funnel wall, and as a result, the funnel wall expands gradually.

Figure 4.16 displays the snapshot of the toroidal magnetic field together with the poloidal magnetic-field lines on the x-z plane at selected time slices. This indeed shows that the configuration of the magnetic-field lines changes from an aligned collimated one near the rotational axis to a more spread one for late time with $t \gtrsim 1\,{\rm s}$.

Since the collimation of the poloidal magnetic-field lines is loosened, the Poynting flux in the vicinity of the rotational axis also decreases gradually. Figure 4.17 shows that the opening angle of the strong Poynting-flux ($-T^{(\mathrm{EM})}{}_t{}^r\sqrt{-g}$) region increases from $\lesssim 10°$ to $\sim 20°$ and the intensity of the Poynting flux becomes weak with time. The reason that the peak of the Poynting flux is located near the funnel wall is that the magnetic-field lines near the funnel wall penetrate the equatorial regions of the spinning black hole, and hence, the Blandford-Znajek effect can be more efficient. If the Poynting flux indeed determines the luminosity of short-hard gamma-ray bursts, its brightness also should decrease for $t \gtrsim 1\,{\rm s}$. This mechanism could be interpreted as a reason that the timescales of short-hard gamma-ray bursts are less than 2 s with the typical timescale of $\sim 1\,{\rm s}$. Specifically, our numerical results propose that the timescale of $\sim 1\,{\rm s}$ is determined by the evolution timescale of the accretion disk (torus), which is determined by the neutrino cooling and magnetohydrodynamics turbulence (effectively viscous process) that control the post-merger mass ejection. See also Sec. 5.2.3 for other mechanism by which $L_{\rm iso}$ is decreased.

A word of the caution is appropriate here. First, the turbulence and dynamo activated by the MRI in the accretion disk are stochastic processes. This implies that the poloidal magnetic-field flux penetrating the black hole could not be precisely predicted. For example, by the accretion of the magnetic fields with a random polarity, the magnetic flux that penetrates the black hole may be smaller than that in the accretion disk. Hence, it is reasonable that the magnetic-field strength could not be always as strong as the one necessary for explaining typical short-hard gamma-ray bursts. Indeed, for model Q6B3H,

[4] In the magnetohydrodynamics simulation, the flow with low values of ρ/b^2 cannot be accurately computed. Therefore, it is not possible to reproduce the high Lorentz factor flow in these simulations.

the Poynting luminosity is by one order of magnitude lower than those for other models. In this case, the magnetic-field strength on the black-hole horizon is about 1/3 of those for other models. Therefore, broadly speaking, there are two possible cases: (1) A magnetosphere with strong poloidal magnetic fields is formed near the rotational axis of a spinning black hole. In this case, the maximum isotropic-equivalent Poynting luminosity of 10^{50}–10^{51} erg/s consistent with typical short-hard gamma-ray bursts can be generated; (2) Due to the stochastic process of the MRI-induced turbulent motion, poloidal magnetic fluxes falling from the disk are not aligned well, and the poloidal magnetic field formed around the black hole is not strong enough to appreciably form a magnetically supported funnel structure (force-free magnetosphere). In such a case, the isotropic-equivalent Poynting luminosity may not be high enough to be consistent with typical short-hard gamma-ray bursts, although a weak Poynting luminosity can be generated as in model Q6B3H. For more detailed understanding on this problem, a larger number of higher-resolution simulations will be necessary.

Chapter 5

Result2: The dependence on initial magnetic field strength, configuration, neutron-star equation of state, and equatorial-plane symmetry

In this chapter, we give results on the simulations with different initial magnetic field strengths, configurations, neutron-star EOSs, and equatorial-plane symmetry and describe the qualitative and quantitative dependence of the evolution processes. We perform 4 simulations with the parameters and quantities summarized in Table 5.1. We discovered that the essential part of the evolution is qualitatively universal irrespective of the setups. Figures. 5.1, 5.2, and 5.3 displays three-dimensional snapshots, two-dimensional snapshots on the y–z plane, and two-dimensional snapshots on the x–y plane. The model shown in these figures is Q4B5tn, for which we do not impose the equatorial-plane symmetry and provide a confined toroidal magnetic field initially with its maximum strength at the center of the neutron star of 5×10^{16} G. The overall evolution process in the merger and the post-merger stages are qualitatively the same as that described in Sec.4.1.

However, we find some differences in the post-merger mass ejection and the evolution of the magnetosphere. Due to the absence of the equatorial-plane symmetry, the post-merger ejecta does not have the symmetry. We also observe that the accretion disk and the magnetosphere tilt. In addition, another model with no equatorial-plane symmetry shows that magnetic-field polarity in the magnetosphere reverses. These differences are likely due to the fact that the post-merger evolution is determined by the stochastic turbulence in the disk. The properties of the magnetosphere denoted here play a role in the decrease of the isotropic-equivalent Poynting luminosity.

In addition, we give a more detailed analysis of the system. We analyze the quality factor of the MRI and discussed the dependence on the initial magnetic field strength. The anisotropic part of the Maxwell and the Reynolds stresses are evaluated to discuss the qualitative aspect of the effective viscosity induced by the magnetohydrodynamic turbulence. We also propose a new method to assess whether the black hole has the ability to form a magnetosphere and launch a jet by evaluating magnetohydrodynamic properties near the horizon.

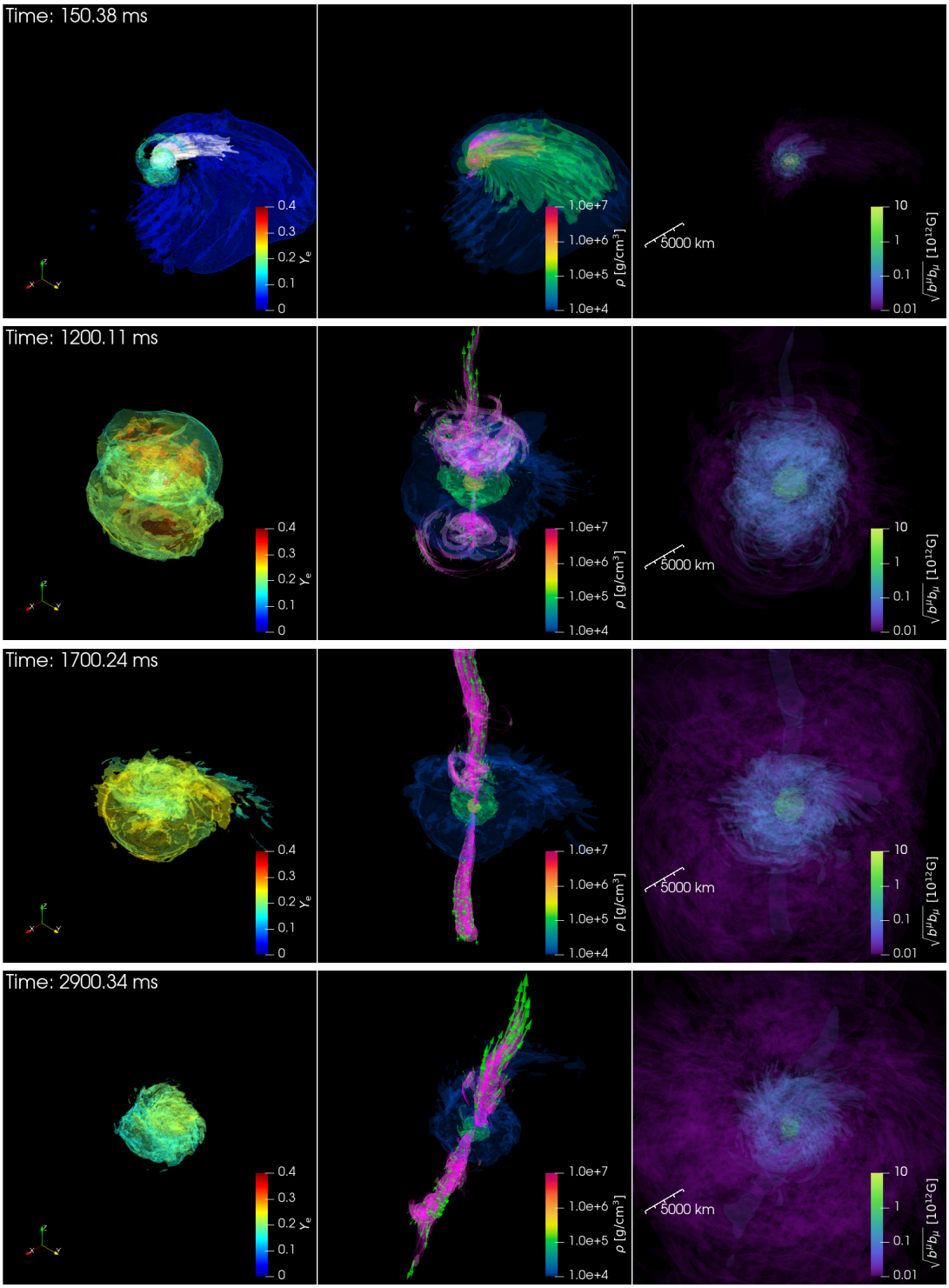

Figure 5.1: The three-dimensional snapshots for model Q4B5tn with the length scale of $\sim 10^4$ km at $t \approx 150$, 1200, 1700, and 2900 ms. For each time, the left panel shows the ejecta, which is colored for the electron fraction Y_e; the middle panel shows the rest-mass density ρ (g/cm^3) (contours) with magnetic-field lines (pink lines), unbound outflow (white color) and its velocity (green arrows); the right panel shows the magnetic-field strength $b = \sqrt{b^\mu b_\mu}$ (G). See also the following link for the animation: `https://www2.yukawa.kyoto-u.ac.jp/~kota.hayashi/Q4B5tn-3D.mp4`.

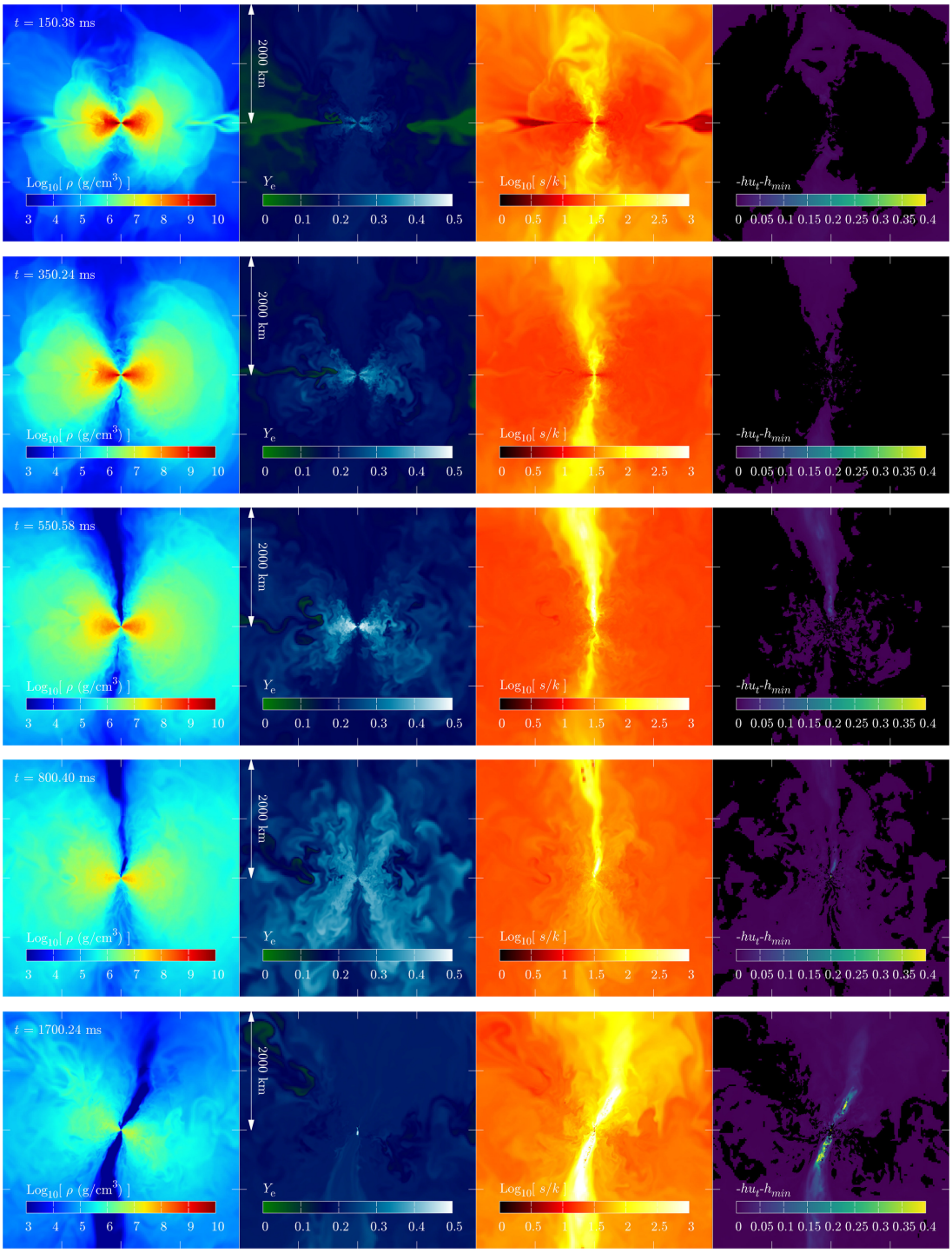

Figure 5.2: The 2D snapshots for model Q4B5tn on the y-z plane with a region of $[-2000$ km : 2000 km$]$ for both y and z at $t \approx 150$, 350, 550, 800, and 1700 ms. For each time, the first, second, third, and fourth panels show the rest-mass density $\rho\,(\mathrm{g/cm^3})$, the electron fraction Y_e, the entropy per baryon s, and $-hu_t - h_\mathrm{min}$, respectively. In the fourth panel, unbound matter is (non-black) colored and bound matter is colored by black. See also the following link for the animation: `https://www2.yukawa.kyoto-u.ac.jp/~kota.hayashi/Q4B5tn-2Dyz.mp4`.

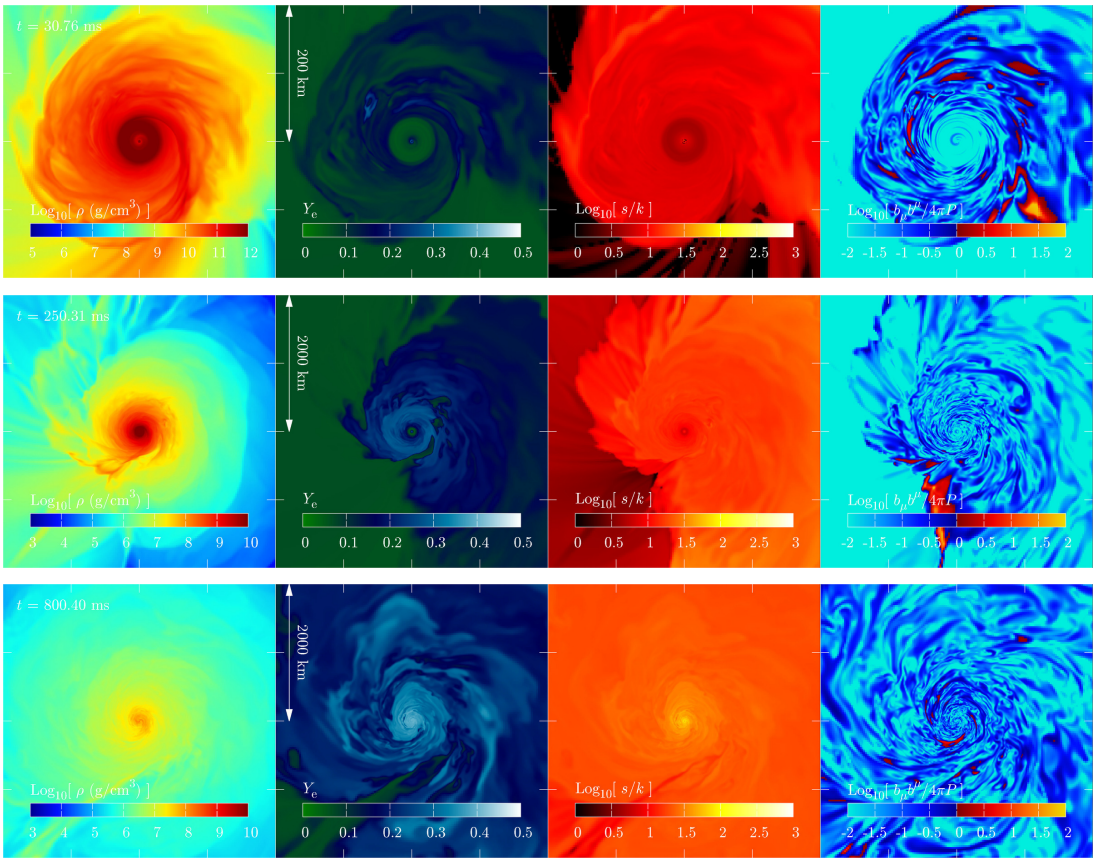

Figure 5.3: The 2D snapshots for model Q4B5tn on the x-y plane with [-200 km : 200 km] for both x and y at $t \approx 30$ ms, and with [-2000 km : 2000 km] at $t \approx 250$, and 800 ms. For each time, the first, second, third, and fourth panels show the rest-mass density $\rho\,(\mathrm{g/cm^3})$, the electron fraction Y_e, the entropy per baryon s, and the inverse of the plasma beta $b^2/4\pi P$, respectively. See also the following link for the animation: `https://www2.yukawa.kyoto-u.ac.jp/~kota.hayashi/Q4B5tn-2Dxy.mp4`.

Table 5.1: Key parameters and quantities for the initial conditions together with the parameters of grid setup for our numerical simulations. $b_{0,\max}$: the initial maximum magnetic-field strength, $\Delta x_{i_{\max}}$: the grid spacing for the finest refinement level, L_1: the location of the outer boundaries along each axis, and the values of N and $i_{\max}$. For all the models, the neutron-star mass is $1.35M_\odot$, the initial black-hole mass is $5.4M_\odot$, the initial dimensionless spin of the black hole is 0.75, and the initial ADM mass $M_{\rm ADM,0}$ is $6.679M_\odot \approx 0.9894m_0$. The models from the previous chapter (Q4B5L and Q4B5H) are also shown for comparison.

model name	EOS	$b_{0,\max}$ [G]	b_0 config.	plane sym.	$\Delta x_{i_{\max}}$ [m]	L_1 [km]	N	$i_{\max}$
Q4B3e15	DD2	3×10^{15}	poloidal	yes	400	6.98×10^4	170	11
Q4B5tn	DD2	5×10^{16}	toroidal	no	400	6.98×10^4	170	11
Q4B5n	DD2	5×10^{16}	poloidal	no	400	6.98×10^4	170	11
SFHoQ4B5	SFHo	5×10^{16}	poloidal	yes	250	3.10×10^4	243	10
Q4B5L	DD2	5×10^{16}	poloidal	yes	400	1.74×10^4	170	9
Q4B5H	DD2	5×10^{16}	poloidal	yes	270	1.62×10^4	234	9

Table 5.2: The dynamical ejecta mass evaluated at $t = 20\,$ms: $M_{\rm eje,dyn}$, and the lower bound of the post-merger ejecta mass: $M_{\rm eje,pm}$ in units of $M_\odot$. Since the mass of the post-merger ejecta is still increasing at the termination of all the runs, we here list the lower bound for it.

model name	$M_{\rm eje,dyn}$	$M_{\rm eje,pm}$
Q4B3e15	0.045	$\geq$0.030
Q4B5tn	0.045	$\geq$0.030
Q4B5n	0.046	$\geq$0.033
SFHoQ4B5	0.013	$\geq$0.019
Q4B5L	0.046	$\geq$0.035
Q4B5H	0.046	$\geq$0.028

5.1 The evolution of the accretion disk and post-merger mass ejection

5.1.1 Disk evolution and ejecta

In this subsection, we present quantitative details on the evolution of the accretion disk and on the post-merger mass ejection. Figure 5.4 shows the time evolution of the rest mass of the matter located outside the apparent horizon $M_{>\rm AH}$ (dashed curves) and the accretion disk mass $M_{\rm disk}$ (solid curves). Figure 5.5 shows the time evolution of the rest mass of the unbound matter (ejecta) $M_{\rm eje}$. The definition of $M_{>\rm AH}$, $M_{\rm disk}$, and $M_{\rm eje}$ are the same as Eqs. (4.3)–(4.7). Table 5.2 shows the rest mass of the dynamical ejecta and the post-merger ejecta.

The results for $M_{>\rm AH}$, $M_{\rm disk}$, and $M_{\rm eje}$ show that the dependence of these quantities on the initial magnetic field setup and equatorial symmetry imposed is weak. Also, the results for the SFHo EOS model are qualitatively similar to those for the DD2 model, although for the SFHo model, $M_{>\rm AH}$, $M_{\rm disk}$, and $M_{\rm eje}$ are smaller than those for the DD2

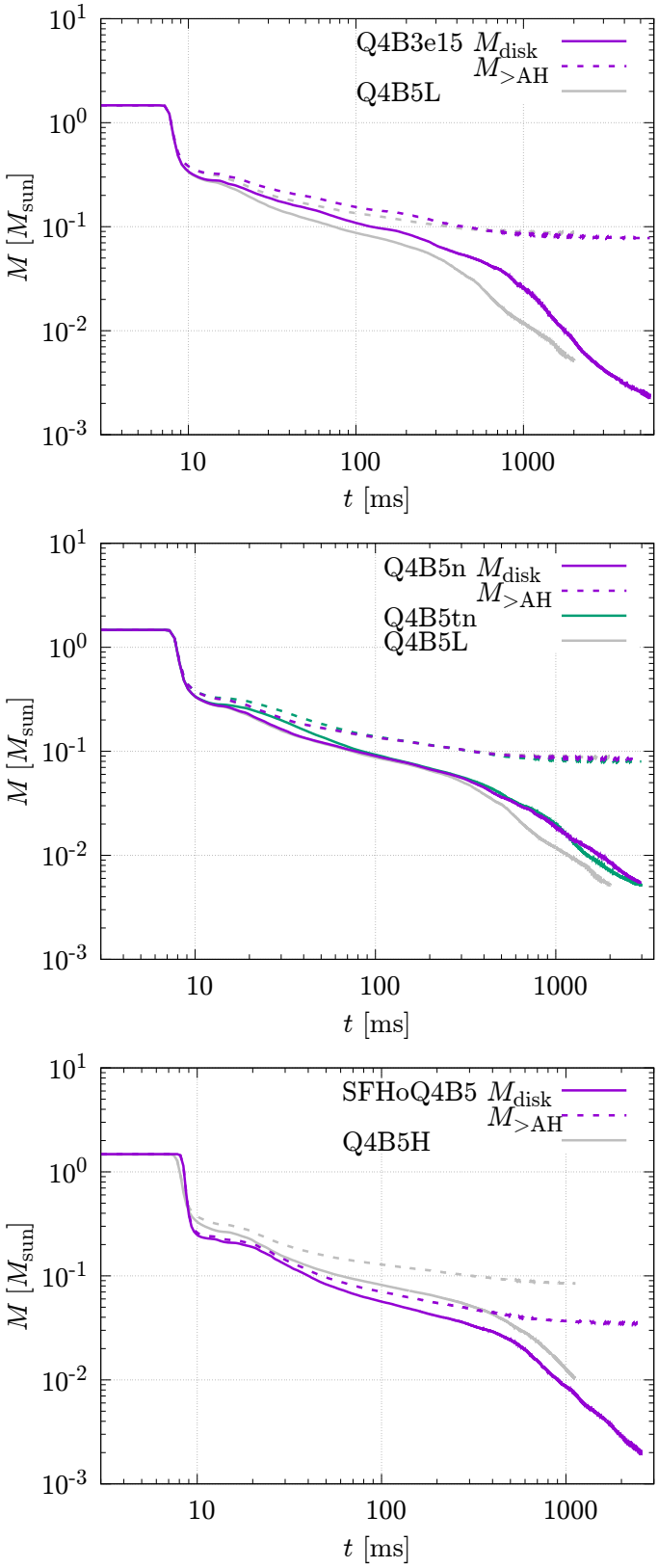

Figure 5.4: The time evolution of the rest mass of the matter located outside the apparent horizon (dotted curves) and the accretion-disk mass (solid curves) for models Q4B3e15 (top panel), Q4B5n and Q4B5tn (middle panel), and SFHoQ4B5 (bottom panel). The results for models Q4B5L and Q4B5H of the previous chapter are also shown for comparison.

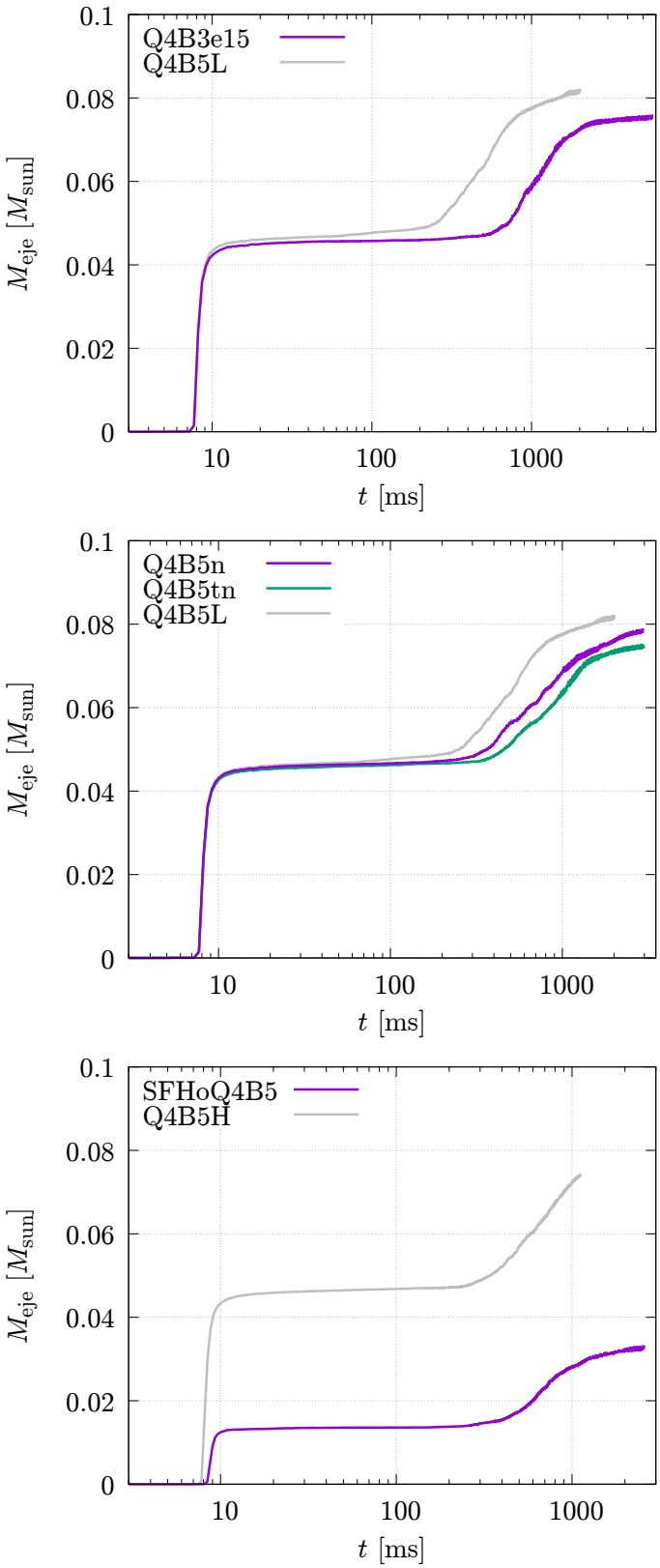

Figure 5.5: The same as Fig. 5.4 but for the time evolution of the rest mass of the unbound matter.

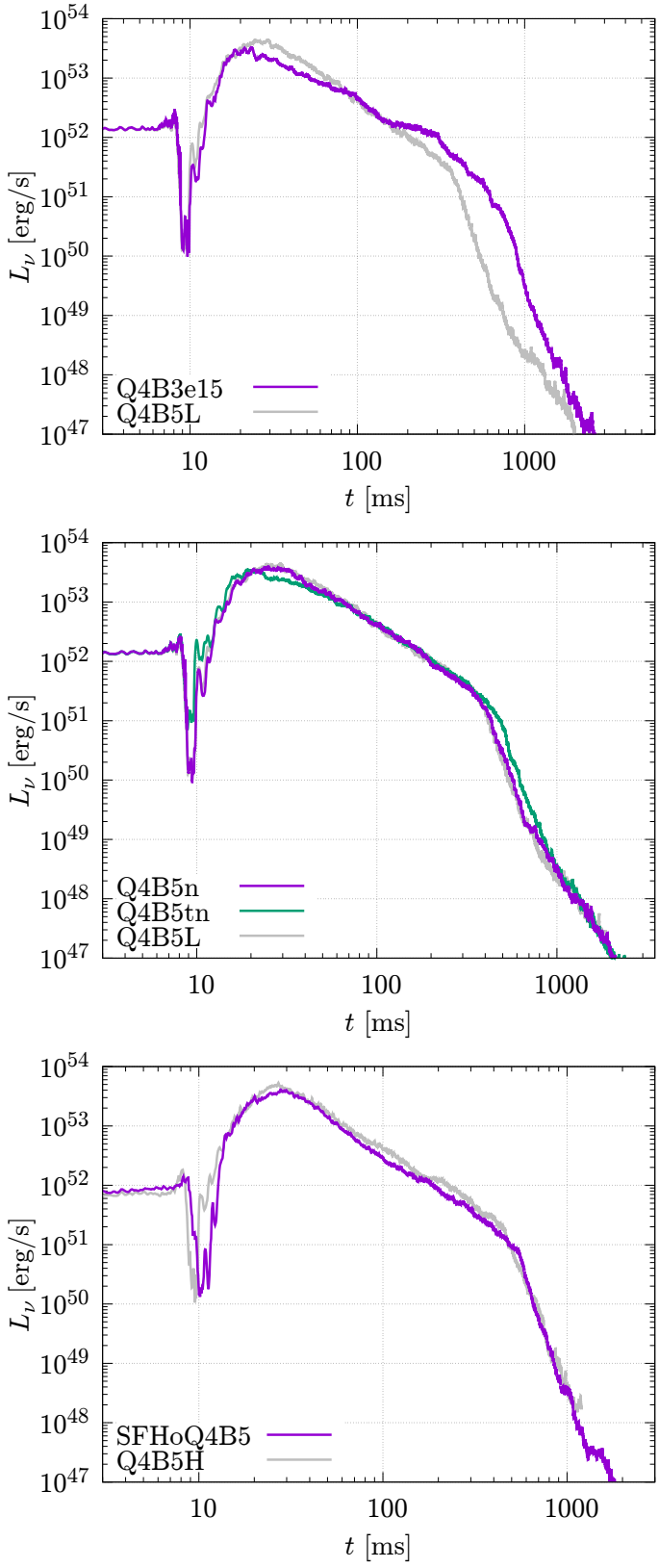

Figure 5.6: The same as Fig. 5.4 but for the time evolution of the total neutrino luminosity. The post-merger mass ejection sets in at $t \sim 300$–500 ms at which $L_\nu \sim 10^{51}$–$10^{51.5}$ erg/s. The results for models Q4B5L and Q4B5H of the previous chapter are also shown for comparison.

model reflecting the smaller neutron-star radius for the SFHo model.

$M_{>\rm AH}$ decreases steeply at $\sim$ 10 ms at which the merger occurs and the majority of the neutron-star matter plunges into the black hole. After that, $M_{>\rm AH}$ continues to decrease gradually due to the matter accretion into the black hole induced by the angular-momentum transport from the magnetohydrodynamics effect. $M_{\rm disk}$ right after the merger is $M_{\rm disk,0} \approx 0.28 M_\odot$ and $\approx 0.22 M_\odot$ for the DD2 and SFHo models, respectively.

The evolution of $M_{\rm eje}$ clearly shows that two distinct components of the ejecta exist. One is the dynamical ejecta, for which the mass steeply increases right after the merger spending only for a few ms. The rest mass for this component is $\approx 0.046 M_\odot$ and $\approx 0.013 M_\odot$ for DD2 and SFHo models, respectively. After this increase by the dynamical mass ejection, $M_{\rm eje}$ remains approximately constant for several hundred ms. Then, $M_{\rm eje}$ starts increasing again at $t \sim$ 300–600 ms. This component is the post-merger ejecta driven by the heating associated with MRI turbulence after the neutrino luminosity decreases below the heating rate (see Fig. 5.6), i.e., L_ν decreases below 10^{51}–$10^{51.5}$ erg/s. The rest mass for this component is $\approx 0.030 M_\odot$ and $\approx 0.019 M_\odot$ for the DD2 and SFHo models at the termination of the simulations, respectively. [1] These values are about 10% of $M_{\rm disk,0}$. The result for the DD2 model shows good agreement with the result of the previous chapter.

The only significant quantitative difference is found in the onset time of the post-merger mass ejection. For example, for model Q4B3e15 which has the low initial magnetic field strength, the onset time of the post-merger mass ejection is $t \sim 600$ ms, i.e., ~ 200 ms behind a high initial magnetic-field strength model Q4B5L. The reason for this is that for the model with the low initial field strength it takes a longer time until the magnetic-field strength is enhanced enough for the disk to be in the equipartition state and for numerical computation to resolve the fastest growing mode of the MRI. It results in the delay of the development of the MRI-induced turbulence in the accretion disk. Note, however, that this delay may not be present in the realistic case, in which the MRI is resolved even for the weak fields. Besides this difference, the process leading up to the post-merger mass ejection is qualitatively the same as that found the previous chapter.

5.1.2 Magnetic-field evolution

Figures 5.7 and 5.8 show the time evolution of the electromagnetic energy, $E_{\rm B}$, and the ratio of the electromagnetic energy to the internal energy, $E_{\rm int}$, respectively. Here, $E_{\rm B}$ and $E_{\rm int}$ are defined, respectively, by Eqs. (4.8), and (4.9). The evolution feature of $E_{\rm B}$ and $E_{\rm B}/E_{\rm int}$ is qualitatively the same as described in the previous chapter.

A quantitative difference is found for models Q4B3e15 and Q4B5nt at $t \lesssim 100$ ms, which corresponds to the stage where the disk is not yet in the equipartition state. For model Q4B3e15, the initial magnetic field is weak and the magnetic-field amplification by winding during the merger stage is insufficient to reach the saturation. For this case, the magnetic-field energy keeps increasing until $t \sim 60$ ms at which the disk settles eventually into an equipartition state, and thus, the magnetic-field amplification saturates. The main contributor to this amplification is clearly understood to be the magnetic winding because E_B increases in proportion to t^2 approximately for $t \approx$ 20–60 ms. In this model, the MRI is not well resolved until $t \sim 200$ ms because of the insufficient grid resolution and/or the insufficient magnetic-field strength (see below), so that we can only find the effect

[1] Strictly speaking we can provide only the lower bound of the post-merger ejecta mass because at the termination of the simulations, the mass is still increasing slightly. Note, however, that the possible additional increase is less than $0.01 M_\odot$ because the disk mass at the termination of the simulation is less than $0.01 M_\odot$.

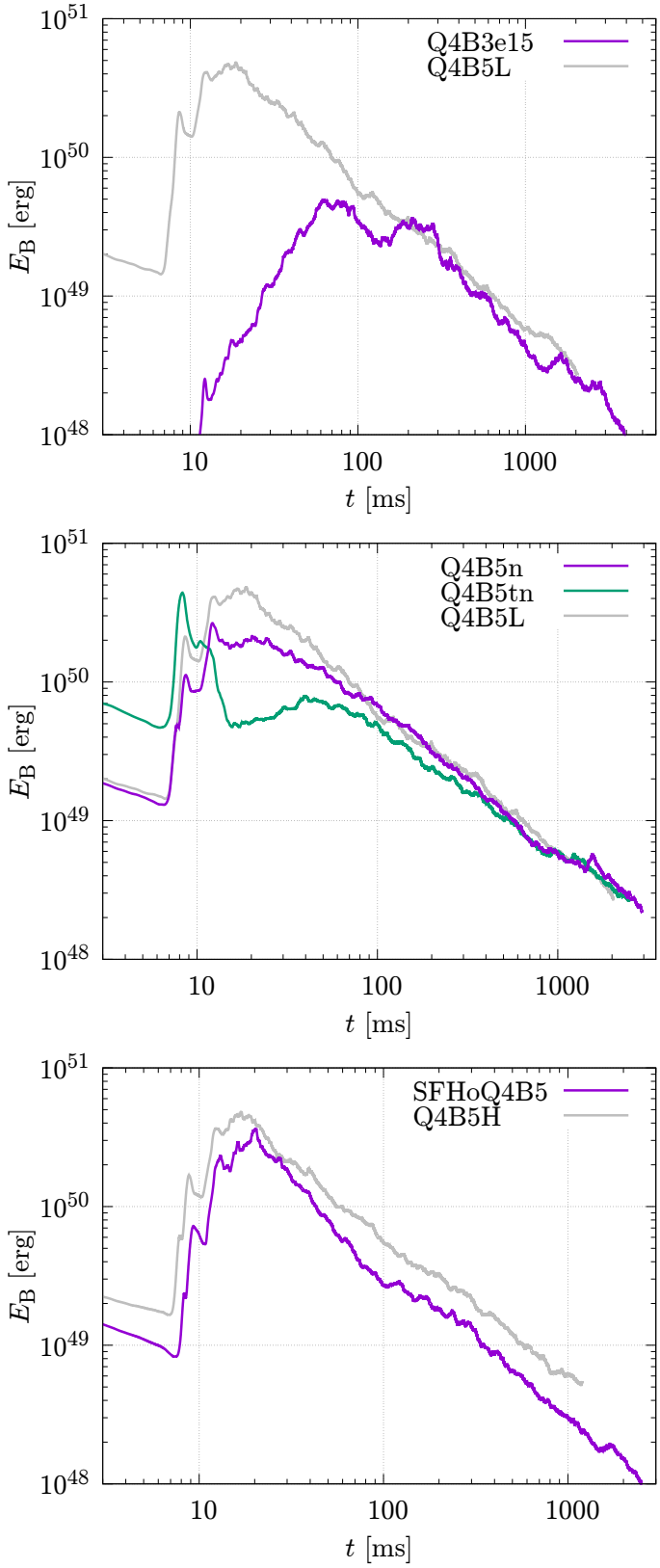

Figure 5.7: The time evolution of the electromagnetic energy evaluated for models Q4B3e15 (top panel), Q4B5n and Q4B5tn (middle panel), and SFHoQ4B5 (bottom panel). The results for models Q4B5L and Q4B5H of the previous chapter are also shown for comparison.

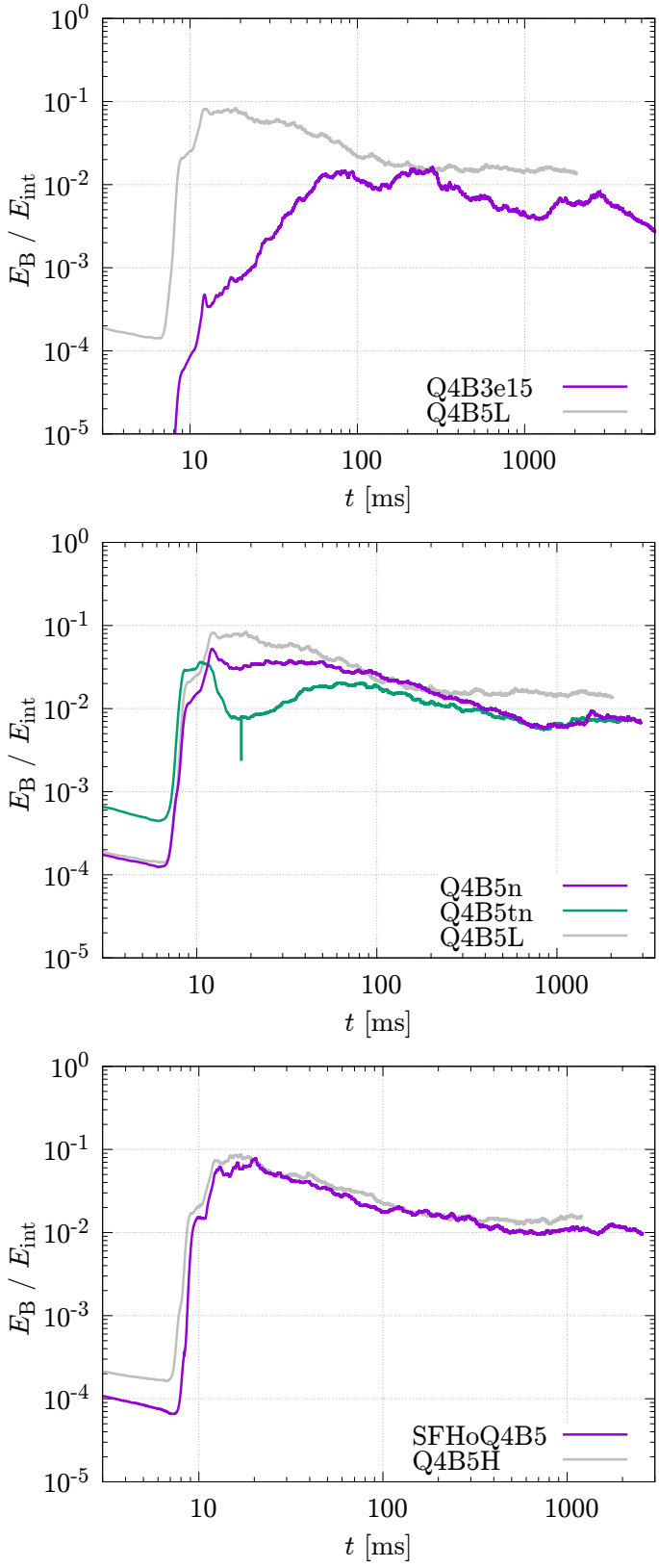

Figure 5.8: The same as Fig. 5.7 but for the time evolution of the ratio of the electromagnetic energy to the internal energy evaluated for the outside of the apparent horizon.

of winding in the magnetic-field amplification. However, for a real system (or in an ideal computation with an infinite grid resolution), the MRI should take place significantly from an earlier stage after the merger. In such realistic cases, we expect that the disk would achieve the equipartition state earlier.

For model Q4B5tn, we find another remarkable behavior right after the merger: During the merger stage $E_{\rm B}$ is amplified up to $\sim 4\times10^{51}$ erg/s, but it rapidly drops by an order of magnitude to $\sim 4\times10^{50}$ erg/s. We do not see this drop for other models. Our interpretation for this drop is that the magnetic-field dissipation by reconnection near the equatorial plane occurs. For this model, we initially embed a strong magnetic field with opposite polarities across the equatorial plane. This magnetic-field configuration causes the magnetic-field reconnection. After this drop, $E_{\rm B}$ starts increasing again by winding, although we do not find the clear power law proportional to t^2 because the magnetic-field energy is close to saturation. At $t \approx 40$ ms $E_{\rm B}$ reaches saturation and starts decreasing again. After the saturation, $E_{\rm B}/E_{\rm int}$ approaches asymptotically $\sim 10^{-2}$ as in other models.

The evolution process after the magnetic field saturates is qualitatively identical irrespective of the initial magnetic-field strength, configuration, neutron-star EOS, and equatorial-plane symmetry. Thus, we conclude that the evolution process shown here is the universal one for black hole-neutron star mergers that experience tidal disruption of neutron stars.

Figure 5.9 shows the evolution of an MRI quality factor, defined by

$$Q_z := \langle |\lambda_{\rm MRI}/\Delta x| \rangle_{\rm ave}\,, \tag{5.1}$$

where $\lambda_{\rm MRI}$ is the wavelength for the fastest growing mode of the axisymmetric MRI defined by Eq. (4.1), and $\langle \cdots \rangle_{\rm ave}$ denotes the spatial average with the weight of the rest-mass density for the region with $\rho \geq 10^6$ g/cm^3. For $Q_z > 10$, we interpret that the MRI is numerically well-resolved. It is found that for most of the models, $Q_z > 10$ is achieved for $t \gtrsim$ 20–50 ms, while for model Q4B3e15, $Q_z > 10$ is achieved only for $t \gtrsim 250$ ms.[2] This illustrates that for the model with lower initial magnetic-field strengths, it takes a longer time until the fastest growing mode of the MRI can be well resolved. As we already remarked, this is an artifact due to the insufficient grid resolution in numerical computation, and hence, in real systems, the MRI turbulence would be developed from an earlier stage.

5.1.3 Effective viscosity

Associated with the development of the MRI turbulence and dynamo, effective viscosity is enhanced in the accretion disk. We here analyze an effective viscosity tensor by evaluating the ratio of the magnetohydrodynamical anisotropic stress to the pressure, which is defined by

$$\alpha_{ij} := \left\langle \left| \frac{1}{P} \left(\rho h \hat{u}_i \hat{u}_j - \frac{1}{4\pi} b_i b_j \right) \right| \right\rangle_{\rm ave}. \tag{5.2}$$

We also evaluate the ratio of the Maxwell stress to the pressure defined by

$$\alpha^{\rm M}_{ij} := \left\langle \left| \frac{1}{P} \left(-\frac{1}{4\pi} b_i b_j \right) \right| \right\rangle_{\rm ave}. \tag{5.3}$$

[2] A steep increase of Q_z takes place at $t \sim 200$ ms, and thus, the MRI activity is also partly visible already for $t \gtrsim 200$ ms in this model.

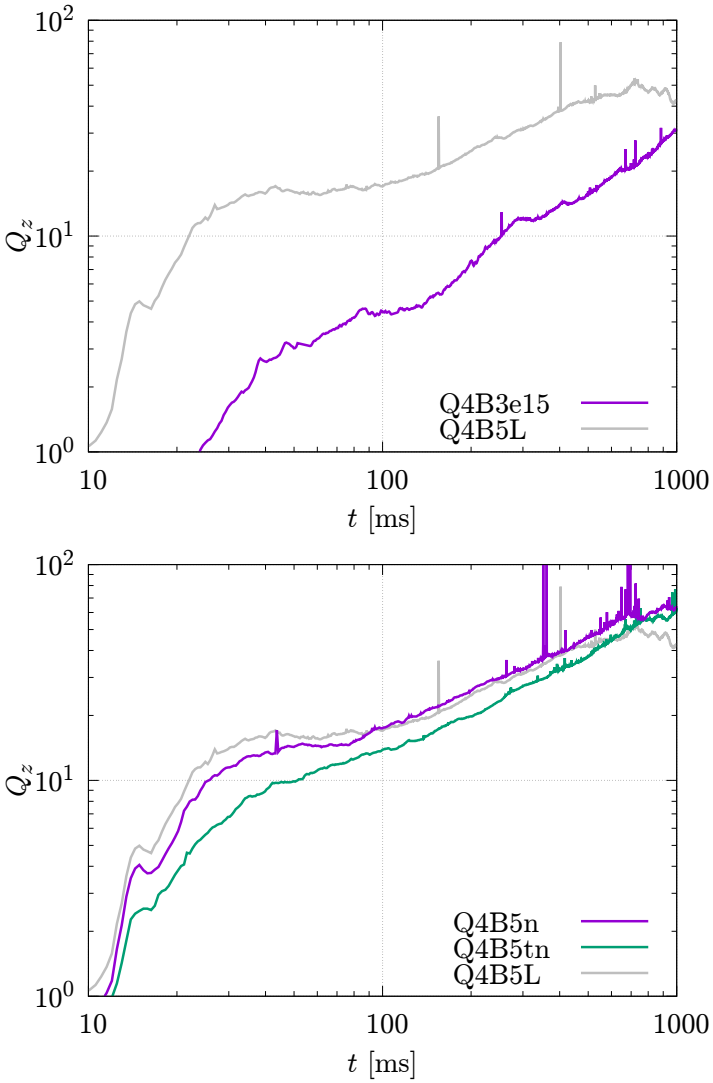

Figure 5.9: The time evolution of the MRI quality factor for models Q4B3e16 (left panel) and Q4B5n and Q4B5tn (right panel). The results for model Q4B5L of the previous chapter are also shown for comparison.

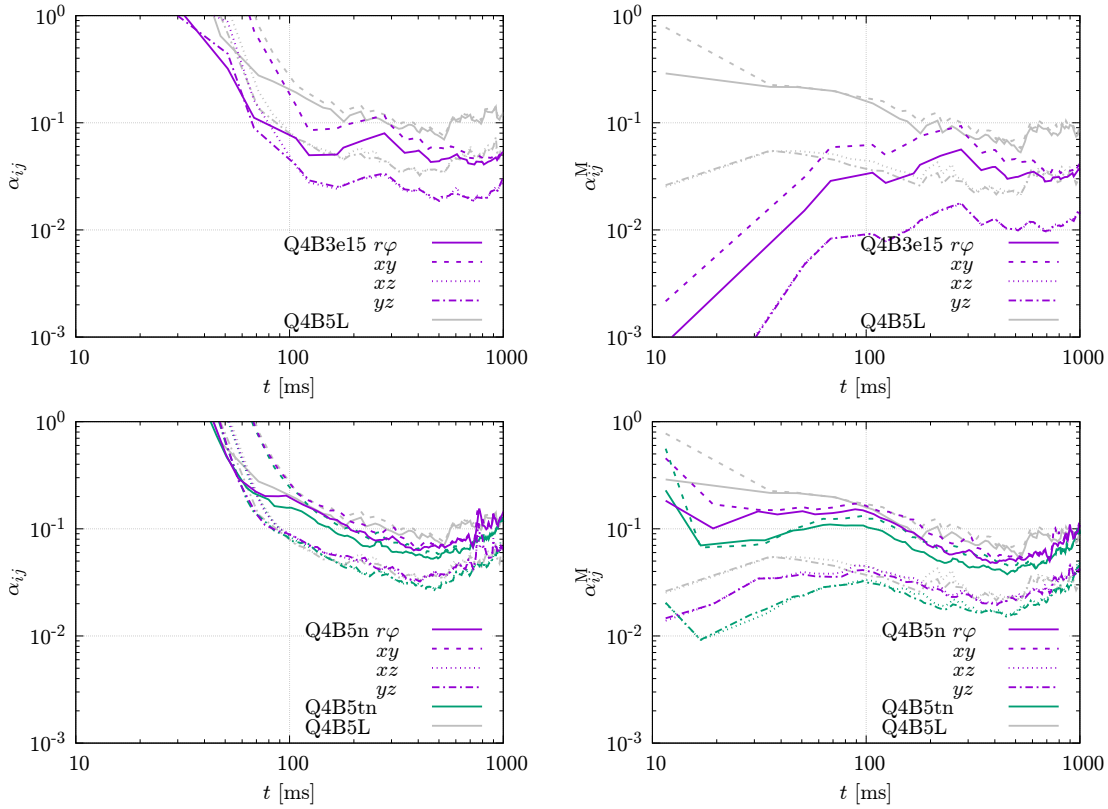

Figure 5.10: The time evolution of the ratio of the magnetohydrodynamical anisotropic stress (left) and Maxwell stress (right) to the pressure, α_{ij} and $\alpha^{\rm M}_{ij}$, respectively. The results for $r\varphi$, xy, xz, and yz components are shown. The top two panels show the results for model Q4B3e15, and the bottom two panels show the results for models Q4B5n and Q4B5tn.

Here, $i \neq j$ (i, $j = x, y, z$) and $\langle \cdots \rangle_{\rm ave}$ denotes the spatial average with the weight of the rest-mass density for the region with $\rho \geq 10^7\,{\rm g/cm^3}$. $\hat{u}_i$ is defined by $u_i - \langle u_i \rangle_{t,{\rm ave}}$ where $\langle u_i \rangle_{t,{\rm ave}}$ denotes the local time average of u_i. The time average needs to be subtracted from u_i to eliminate the contribution of coherent motion (not random motion) for evaluating the anisotropic stress associated with the turbulent motion.

Figure 5.10 plots the time evolution of the off-diagonal components of α_{ij} and $\alpha^{\rm M}_{ij}$. This shows that for $t \lesssim 100\,{\rm ms}$ $\alpha_{ij} > O(0.1)$, but we interpret that this is not a physical value, nor associated with the magnetohydrodynamics effect: The remnant matter shows the non-axisymmetric structure for $\lesssim 100\,{\rm ms}$ after the merger, and in such a case, the value of α_{ij}, specifically the contribution from the Reynolds stress part, cannot be evaluated properly. Thus we focus only on the stage for $t \gtrsim 100\,{\rm ms}$ for which the non-axisymmetric structure is not very appreciable and the MRI turbulence is developed.

When the disk is in a MRI turbulent stage, we find that the $r\varphi$ and xy components are $\approx$ 0.05–0.1, and xz and yz components are $\approx$ 0.02–0.05. Hence, the order of the magnitude of α_{ij} agrees with the often-used value of the alpha viscous parameter for the accretion disk [77], although the magnitude for each component of α_{ij} has anisotropy. Our interpretation for this anisotropy is that not only the MRI turbulence but also the effects by the global magnetic fields such as magneto-centrifugal effects [119] contribute to the angular momentum transport because α_{ij} for $r\varphi$ and xy components are larger than the others. We also note that the dominant part of α_{ij} stems from the Maxwell stress; the contribution of the Reynolds stress, which originates from the fluid turbulent motion, is ~ 0.01 irrespective of the model and component. This trend is universally found for all the models.

The previous subsection showed that the typical timescale of this disk evolution is several hundred ms. Considering the $r\varphi$ component of the effective viscosity tensor $\alpha_{r\varphi} \approx 0.05$, we evaluate the timescale of the effectively vicious process to be

$$\tau_{\rm vis} \sim \frac{R^2}{\alpha_{r\varphi} c_{\rm s} H} \sim 660{\rm ms} \left(\frac{\alpha_{r\varphi}}{0.05}\right)^{-1} \left(\frac{c_{\rm s}}{10^9{\rm cm/s}}\right)^{-1} \times \left(\frac{H}{3\times 10^6{\rm cm}}\right)^{-1} \left(\frac{R}{10^7{\rm cm}}\right)^{2}, \quad (5.4)$$

which is consistent with the timescale of the disk evolution. Here, R and H are the radius and the height of the disk, respectively, and $c_{\rm s}$ denotes the sound speed.

Model Q4B3e15, which has a low initial magnetic-field strength, shows a factor of ~ 2 smaller value than for the other models, but this is relatively minor compared to the difference in the initial magnetic field strength (the initial magnetic field is smaller than the other models by a factor of ~ 17). This result suggests that for this model, the fastest growing mode of the MRI might be only partly resolved. Indeed, for this model, a delay with $\sim 200\,{\rm ms}$ in the magnetic-field amplification as well as in all the processes of the disk evolution is found. This indicates that the disk expansion due to the angular momentum transport is delayed due to the weaker turbulence viscosity. As a result of this delay, the drop of the disk temperature and neutrino luminosity delays, and thus, the post-merger mass ejection is delayed by $\sim 200\,{\rm ms}$. Note, however, that the delay could be the artifact due to the insufficient grid resolution.

5.1.4 Property of ejecta

Now, we turn our attention to the properties of the ejecta. Figures 5.11 and 5.12 show the rest-mass histogram as a function of the electron fraction $Y_{\rm e}$ and velocity v for the ejecta component, respectively.

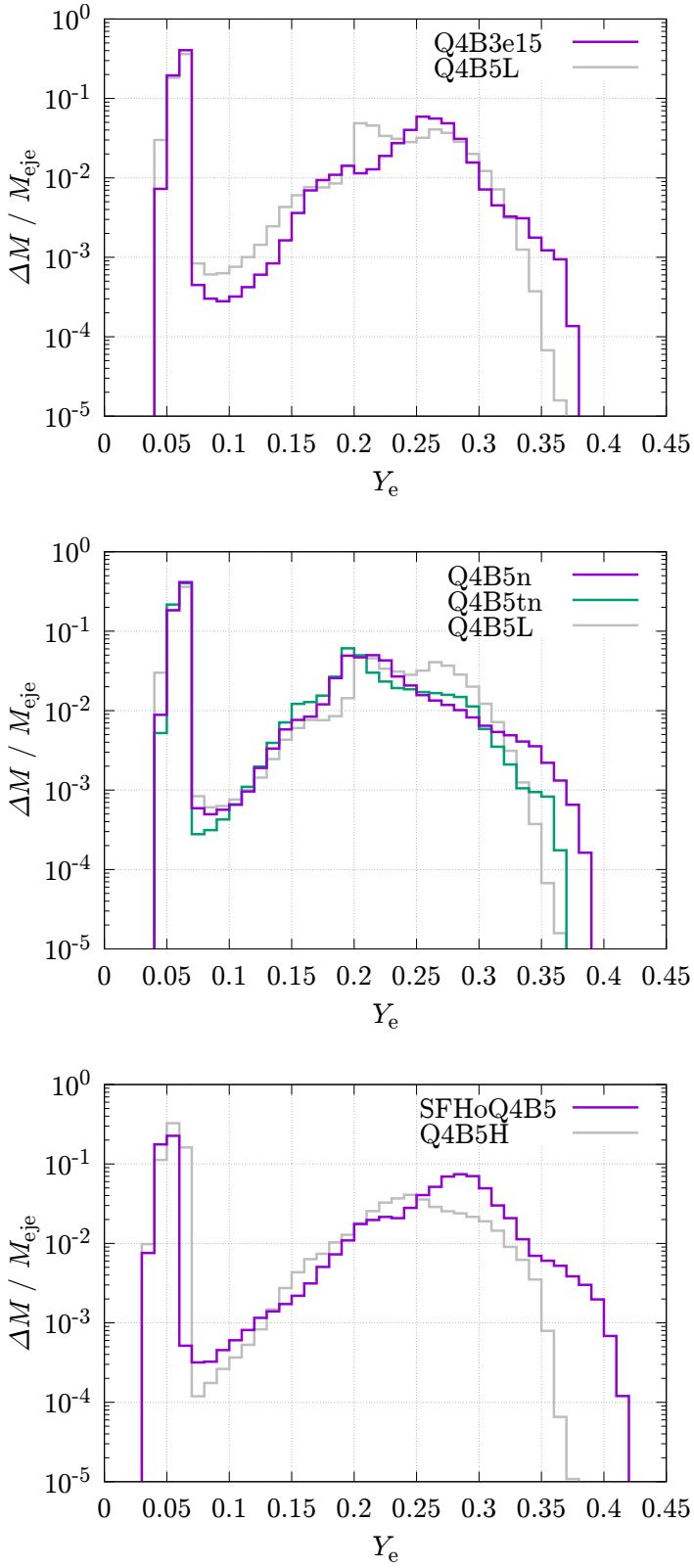

Figure 5.11: Mass histogram as a function of the electron fraction of the ejecta for models Q4B3e15 (top panel), Q4B5n and Q4B5tn (middle panel), and SFHoQ4B5 (bottom panel). The results for models Q4B5L and Q4B5H of the previous chapter are also shown for comparison. Note that the vertical axis is normalized by the total ejecta mass.

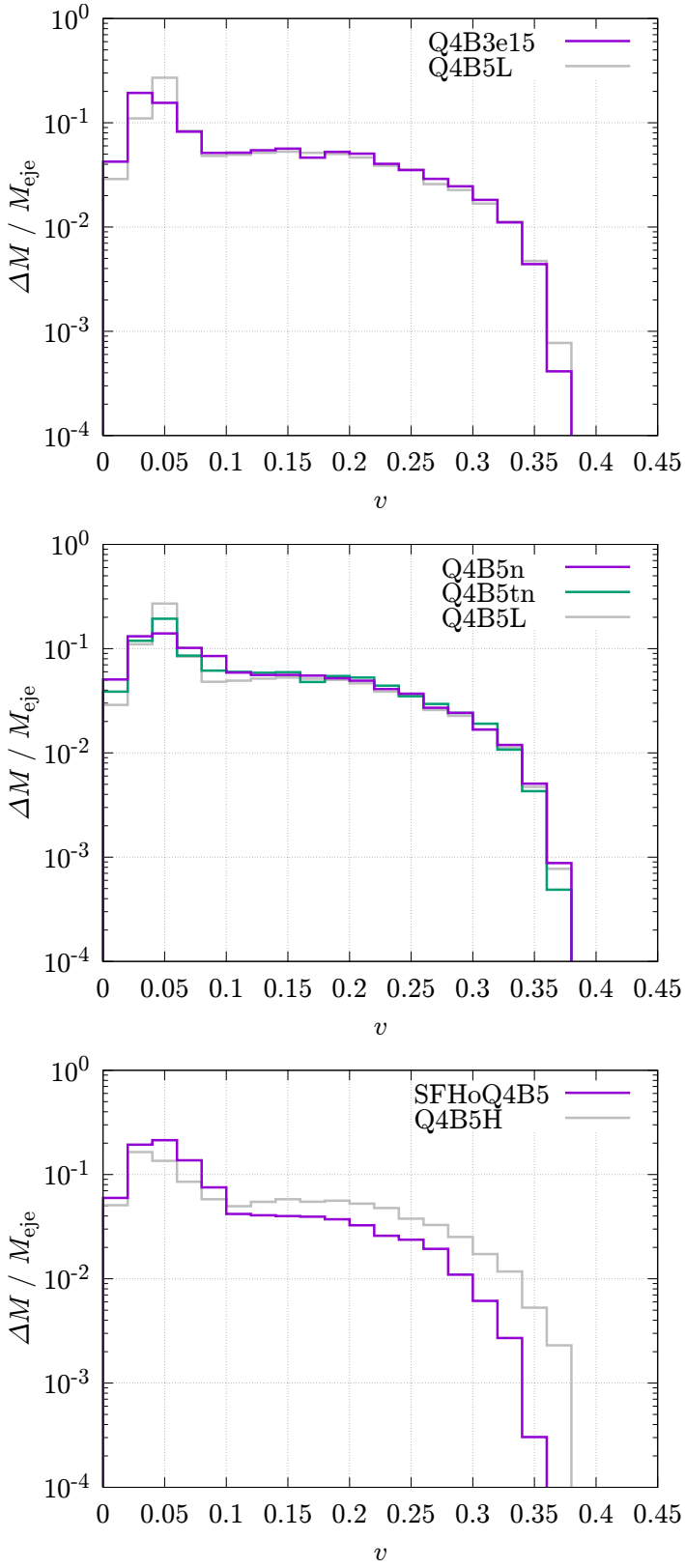

Figure 5.12: The same as Fig. 5.11 but for the mass histogram as a function of the velocity of the ejecta.

There are two distinctive Y_e components for the ejecta as found in previous chapter. One is the dynamical ejecta for which $Y_e \approx 0.03$–0.07 irrespective of the simulation setups. However, the range of Y_e for the dynamical ejecta depends slightly on the EOS: For model SFHoQ4B5, $Y_e \approx 0.03$–0.06, while for model Q4B5H with DD2 EOS, $Y_e \approx 0.03$–0.07 [45]. The electron fraction of the dynamical ejecta directly reflects the neutron richness of the neutron star because the dynamical ejecta is affected only weakly by the thermal and weak-interaction process in the merger and post-merger stages. Thus, the difference in the distribution of Y_e for the dynamical ejecta between models SFHoQ4B5 and Q4B5H comes directly from the difference in the neutron star EOSs.

For the post-merger ejecta, the electron fraction is higher as $0.1 \lesssim Y_e \lesssim 0.4$ and has a peak at $Y_e \sim 0.25$ for the models with the DD2 EOS and $Y_e \sim 0.3$ for the model with the SFHo EOS. We note that irrespective of the initial magnetic-field setups and equatorial-plane symmetry, approximately the same distribution is found for the DD2 models. However, the difference in the EOS makes a quantitative difference. Comparing the high-resolution models SFHoQ4B5 and Q4B5H, we find that model SFHoQ4B5 has a distribution with higher Y_e values. In our interpretation, this is due to the fact that the neutron star modeled by the SFHo EOS is tidally disrupted at an orbit closer to the black hole because it has a smaller neutron-star radius. Then the matter that forms the one-armed structure right after the merger and subsequently forms an accretion disk experiences stronger compression and shock heating between the inner and the outer spiral arms. As a result, the disk temperature is enhanced right after the tidal disruption and the value of Y_e is also enhanced (see also Ref. [45]).

There are also two components in the mass histogram as a function of the velocity of the ejecta (see Fig. 5.12). The high-velocity component with $v/c \gtrsim 0.1$ stems primarily from the dynamical ejecta, while the low-velocity component stems primarily from the post-merger ejecta. For the DD2 models, the velocity histogram has approximately identical distributions irrespective of the setups, and it also agrees with the result of the previous chapter. For the SFHo model, the low-velocity component has a higher fraction than that for the DD2 models, because the dynamical ejecta mass is smaller while the post-merger ejecta mass is comparable with that of the DD2 models.

5.2 Magnetic field in the funnel region and the relation to the short-hard gamma-ray burst

5.2.1 Poynting luminosity and magnetic field in the funnel

Figure 5.13 shows the time evolution of $L_{\rm iso}$,which is defined by Eqs. (4.14), and (4.15). For models Q4B5n, and Q4B5tn, the typical maximum value of $L_{\rm iso}$ is $O(10^{50})$ erg/s. The high-Poynting luminosity stage, which is designated by $L_{\rm iso} \gtrsim 3\times10^{49}$ erg/s in this chapter, is identified for $t \approx 300$–2500ms for model Q4B5n. For model Q4B5tn, the high-Poynting luminosity stage for the upper and lower hemispheres is identified for $t \sim 500$–1500 ms and ~ 1000–1600 ms, respectively. During the high-Poynting luminosity stage, $L_{\rm iso}$ varies with time by more than an order of magnitude for these models, reflecting the variation of the magnetic-field strength and configuration. The reason for this variability is that the magnetic fields with high field strengths are often provided from the disk to the black hole by the MRI dynamo activity. Figure 5.14 shows the average value of the toroidal field $b_{\bar{\varphi},\rm ave}$ as a function of time and polar angle θ for models Q4B3e15, Q4B5n, and Q4B5tn. Here, x, y, and z are defined with respect to the black-hole center (the location of the puncture). The toroidal field is defined by $b_{\bar{\varphi}} = (xb_y - yb_x)/\sqrt{x^2+y^2}$. The average is

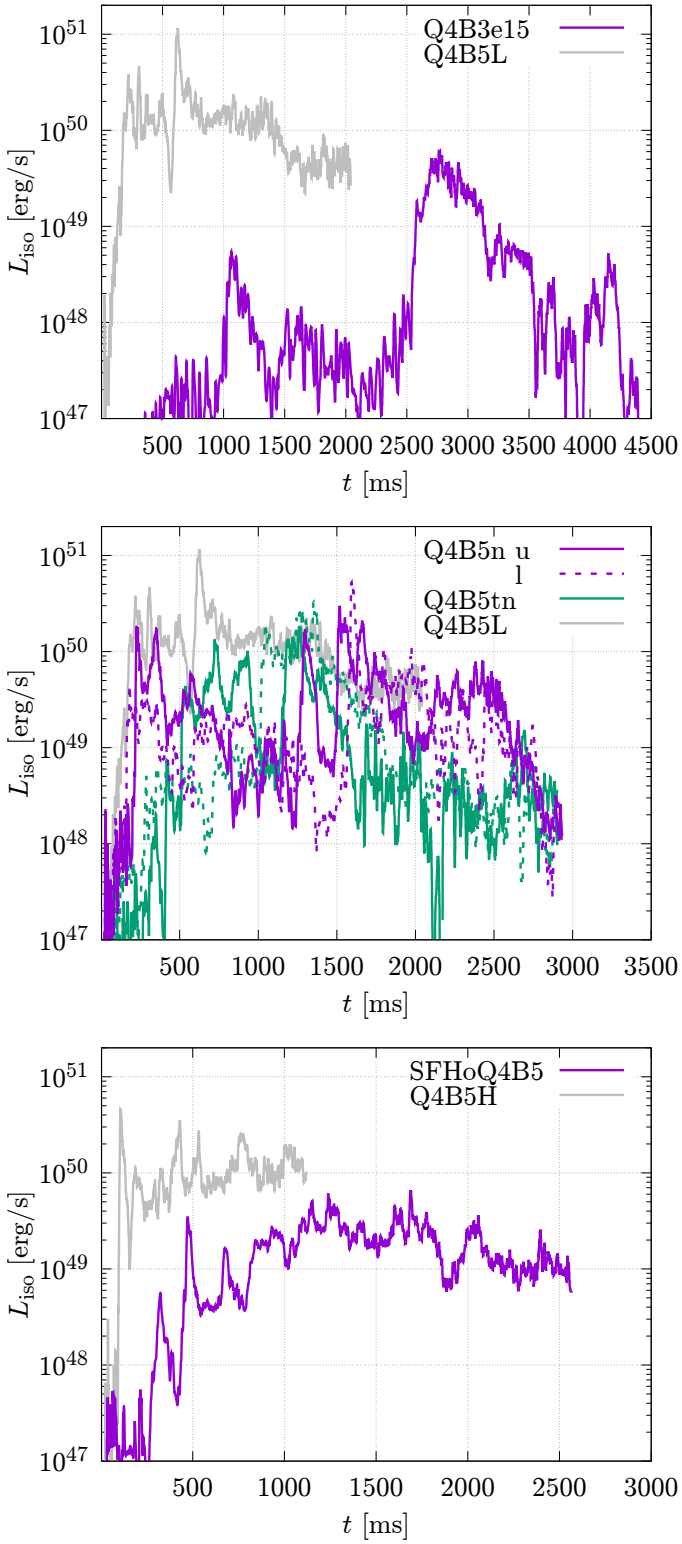

Figure 5.13: The time evolution of isotropic-equivalent Poynting luminosity $L_{\rm iso}$ for models Q4B3e15 (top panel), Q4B5n and Q4B5tn (middle panel), and SFHoQ4B5 (bottom panel). The results for models Q4B5L and Q4B5H of the previous chapter is also shown for comparison. The characters "u" and "l" denote the upper and lower hemispheres, respectively.

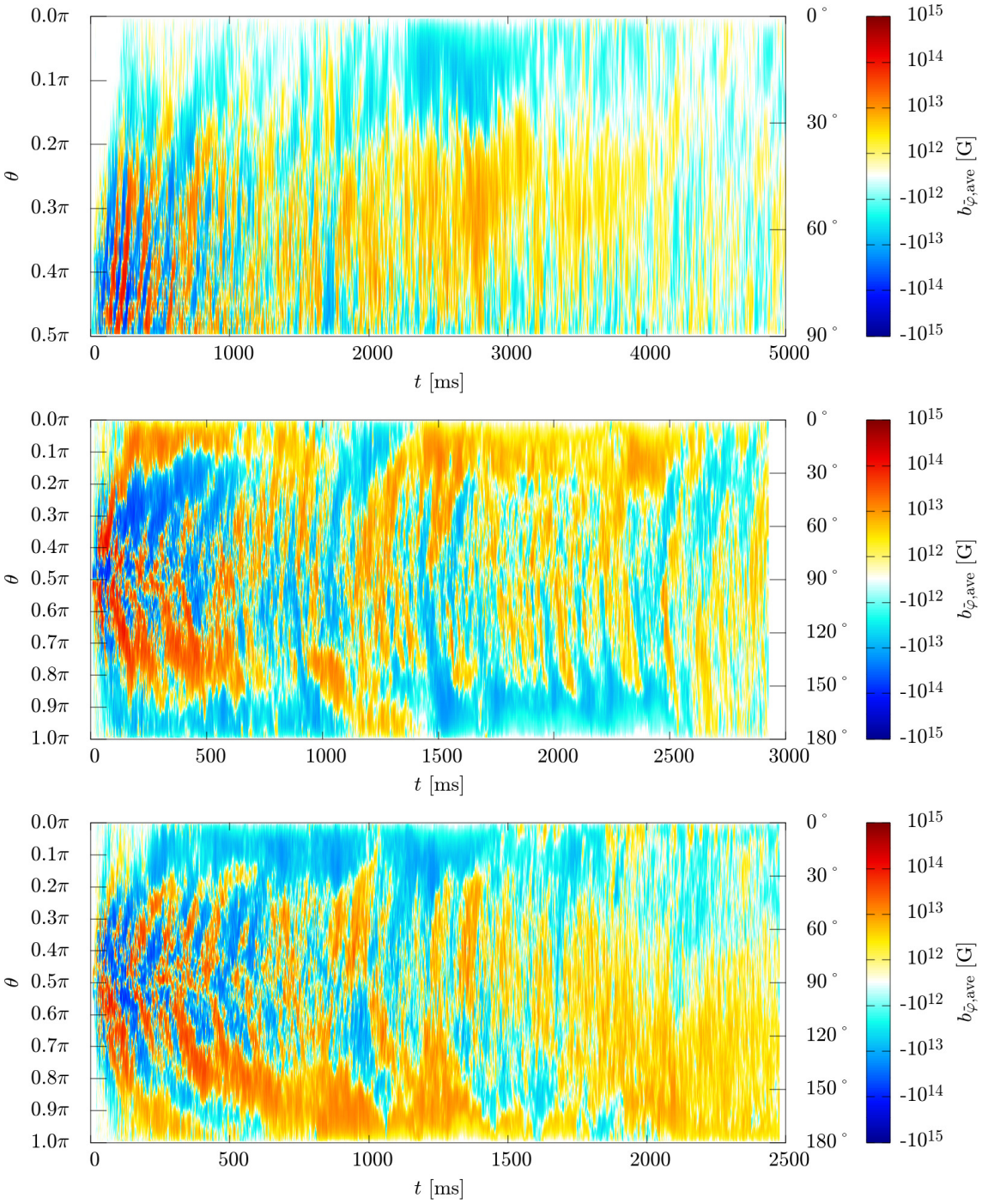

Figure 5.14: The profile of the average toroidal magnetic field along the polar direction (θ) at $r \approx 150$ km as a function of time for models Q4B3e15 (top panel), Q4B5n (middle), and Q4B5tn (bottom).

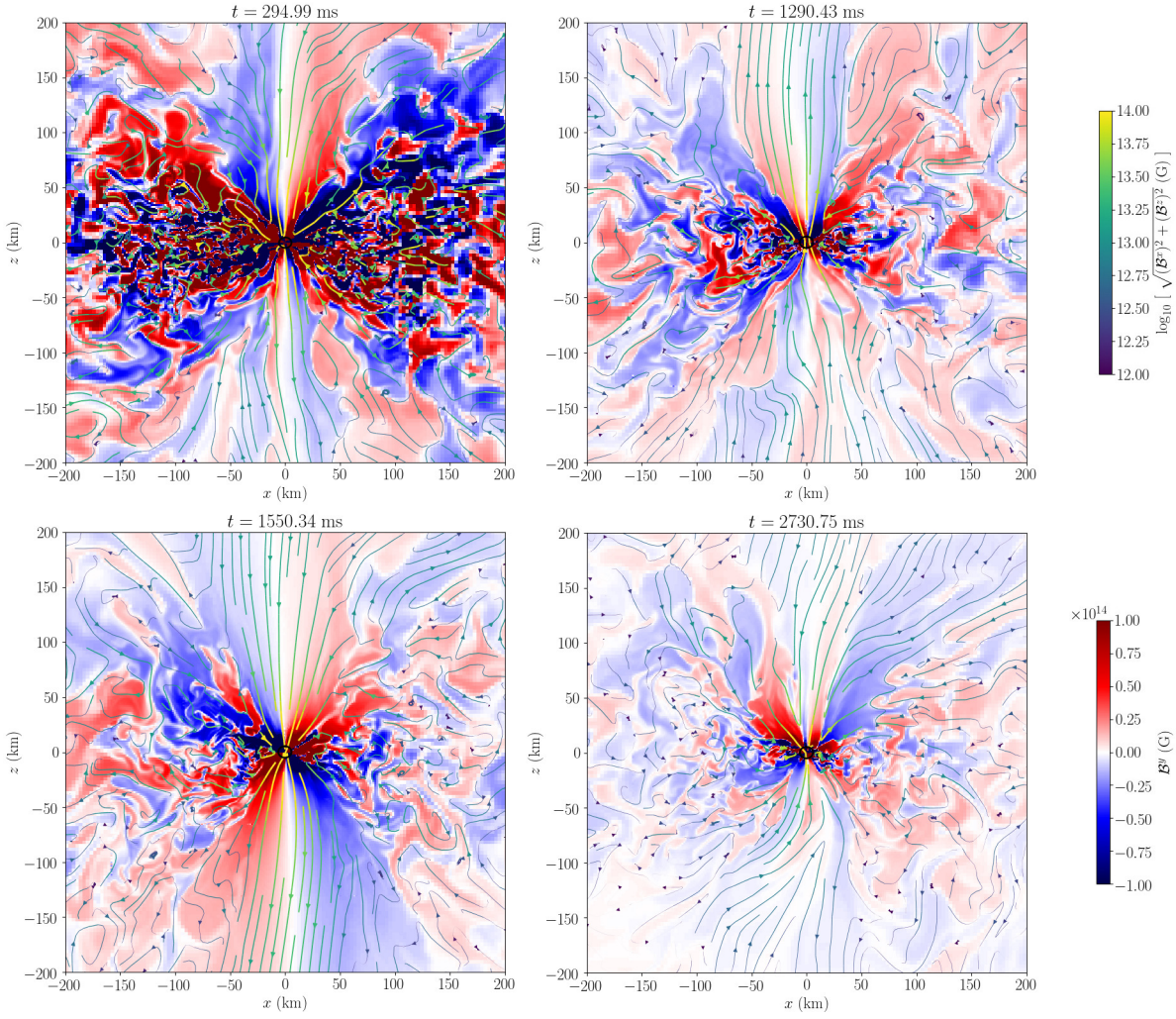

Figure 5.15: The snapshot of the toroidal magnetic field (color profile) together with the poloidal magnetic-field lines (curves) on the x-z plane at selected time slices for model Q4B5n. See also the following link for an animation: `https://www2.yukawa.kyoto-u.ac.jp/~kota.hayashi/Q4B5n-mf.mp4`.

performed with respect to the azimuthal angle $\varphi = \tan^{-1}(y/x)$ at the selected radius of $r := \sqrt{x^2+y^2+z^2} \approx 150\,\mathrm{km}$. Figure 5.14 displays the butterfly structure [118]; the polarity of the toroidal magnetic field flips in a quasi-periodic manner with the period of ~ 20 local orbital periods. Also, the strong magnetic-field fluxes continuously ascend from the equatorial plane to the surface of the accretion disk.

Although this butterfly structure induced by the MRI dynamo was already found in the models of the previous chapter, we find an interesting new feature in our current model; the MRI dynamo activity in the accretion disk determines the magnetic-field structure in the magnetosphere. In the dynamo activity, the magnetic fields often ascend from the disk to the vertical and polar regions. For most of the cases, they do not cancel out or alternate the fields originally stayed there, and thus, the polarity of the magnetosphere is unchanged. However, for exceptional cases, the inversion of the polarity is achieved. For model Q4B5n, this occurs at $t \sim 1.1\,\mathrm{s}$ and $1.4\,\mathrm{s}$ (see the middle panel of Fig. 5.14). For $t \lesssim 1.1\,\mathrm{s}$, the polarity of $b_{\bar{\varphi},\mathrm{ave}}$ is positive in the polar region of the upper hemisphere. Then at $t \sim 1.1\,\mathrm{s}$, the polarity flips to negative, following the polarity flip at an inner region of the accretion disk. Subsequently, at $t \sim 1.4\,\mathrm{s}$, the polarity flips back to positive. For L_{iso} of this model, there are three characteristic peaks at $t \sim 0.3\,\mathrm{s}$, $1.3\,\mathrm{s}$, and $1.5\,\mathrm{s}$. These peaks reflect the variation of the butterfly structure at the polar region: During the polarity flips in progress, the intensity of the outgoing Poynting flux and L_{iso} naturally drop, because the magnetic field in the polar region is not aligned and the magnetosphere loses a coherency with respect to the magnetic-fields lines.

This polarity flip in the magnetosphere is also found in the snapshots of the magnetic-field structure. Figure 5.15 shows the toroidal and poloidal magnetic field structures on the x-z plane at $t \sim 0.3\,\mathrm{s}$, $1.3\,\mathrm{s}$, $1.5\,\mathrm{s}$, and $2.7\,\mathrm{s}$ for model Q4B5n. The first three panels correspond to the snapshots at which L_{iso} is at local peaks. The figure clearly shows the polarity flip of both poloidal and toroidal magnetic fields in the magnetosphere. The magnetic fields ascending from the disk reconnect the originally-existing fields in the magnetosphere, and subsequently, the polarity is changed.

The middle and bottom panels of Fig. 5.14 also show the magnetic-field polarity flip near the polar region for $t > 2.5\,\mathrm{s}$ of model Q4B5n and for $t \sim 1.0\,\mathrm{s}$ on the upper hemisphere of model Q4B5tn. However, for these stages, no peak in L_{iso} is found and its typical value is lower than $\sim 10^{49}\,\mathrm{erg/s}$, which is an order of magnitude lower than the peak luminosity. Our interpretation for this is that the magnetic fields ascending from the disk due to the MRI dynamo activity disturb or deform the magnetosphere, but are not strong enough or aligned enough to replace the polarity of the field completely and reform the magnetosphere that can launch a high-intensity Poyting flux with $L_{\mathrm{iso}} \sim 10^{50}\,\mathrm{erg/s}$.

We note that the polarity flip was already reported in magnetohydrodynamics simulations for the accretion disks around a spinning black hole [64, 79]. For these simulations, the authors also found a turbulent state of the accretion disks. Thus, the polarity flip is likely to occur often, if magnetic fluxes with high field strengths are ejected from the inner region of the disks in a turbulent state.

For both models Q4B3e15 and SFHoQ4B5, the maximum value of L_{iso} is $\sim 5 \times 10^{49}\,\mathrm{erg/s}$, which is slightly lower than those of other models for which typically $L_{\mathrm{iso}} \sim 10^{50}\,\mathrm{erg/s}$ in the bright stages. Our interpretation is that this is due to the lower magnetic-field strength in the magnetosphere. For these models, the rest-mass density in the disk at the time when the magnetosphere is formed is lower. The reason for model Q4B3e15 is that it takes a longer time to form the magnetosphere than for the other DD2 models and the reason for model SFHoQ4B5, the disk mass is smaller than for the DD2 models. As we already mentioned, the field strength in the magnetosphere is determined by

the field strength of the disk at which the equipartition state is achieved. For model Q4B3e15, the equipartition is achieved in the relatively late stage, at which the rest-mass density and internal energy of the disk are relatively low. This leads to a lower magnetic-field strength in the magnetosphere for these two models. As a result of the lower field strength, the Poynting luminosity, which is powered by the Blandford-Znajek mechanism, becomes lower. The lower maximum value of $L_{\rm iso}$ for model SFHoQ4B5 is understood as the physical result, while that for model Q4B3e15 could be the numerical artifact due to the insufficient grid resolution.

The high-Poynting luminosity stage for model Q4B3e15 starts at ~ 2600 ms and lasts for ~ 400 ms, entering the fading stage at ~ 3000 ms. For model SFHoQ4B5, the high-Poynting luminosity stage starts at ~ 1100 ms. We do not find a clear fading stage for this model, but $L_{\rm iso}$ appears to gradually decrease to $\sim 10^{49}$ erg/s at the termination of the simulation. We indeed find for this model that the opening angle increases with a timescale of a few seconds, and thus, we expect that $L_{\rm iso}$ will eventually drop in this timescale.

The isotropic-equivalent Poynting luminosity of $L_{\rm iso} \sim 10^{50}$ erg/s together with the opening angle of $\theta \sim 10^\circ$ (cf. Fig. 5.1) fairly agrees with those for short-hard gamma-ray bursts (or at least for low-luminosity short-hard gamma-ray bursts) in the assumption that the conversion efficiency of the Poynting flux to the gamma-ray radiation is sufficiently high (i.e., close to unity) [14, 15].

5.2.2 MADness parameter

Figure 5.16 shows the time evolution of the so-called MADness parameter which is defined by [78]

$$\phi_{\rm AH} := \frac{\Phi_{\rm AH}}{\sqrt{\dot{M}_{\rm AH} 4\pi r_{\rm AH}^2 c}}, \tag{5.5}$$

where

$$\begin{aligned} \dot{M}_{\rm AH} &:= \oint_{\rm AH} \rho\sqrt{-g} u^i dS_i \\ &\approx \oint_{r=\max(r_{\rm AH})} \rho_* v^r r^2 \sin\theta d\theta d\varphi, \end{aligned} \tag{5.6}$$

and

$$\begin{aligned} \Phi_{\rm AH} &:= \oint_{\rm AH} B^i \sqrt{\gamma} dS_i \\ &\approx \oint_{r=\max(r_{\rm AH})} \mathcal{B}^r r^2 \sin\theta d\theta d\varphi. \end{aligned} \tag{5.7}$$

It is found that for all the models $\phi_{\rm AH} < 10$ within the simulation time. Thus, the accretion disks in our simulations do not satisfy the often-referred condition for the magnetically-arrested disk (MAD), $\phi_{\rm AH} \gtrsim 50$ [78]. However, as we have already described, a high-intensity Poynting flux is generated even if the condition for the MAD is not satisfied. Thus, the MADness parameter $\phi_{\rm AH}$ may not be suitable for assessing whether the jet is launched in the context of neutron-star mergers.

Figure 5.17 shows the time evolution of $\Phi_{\rm AH}$: the magnetic flux penetrating the apparent horizon. For models Q4B5n and Q4B5tn, the magnetic fluxes penetrating the upper

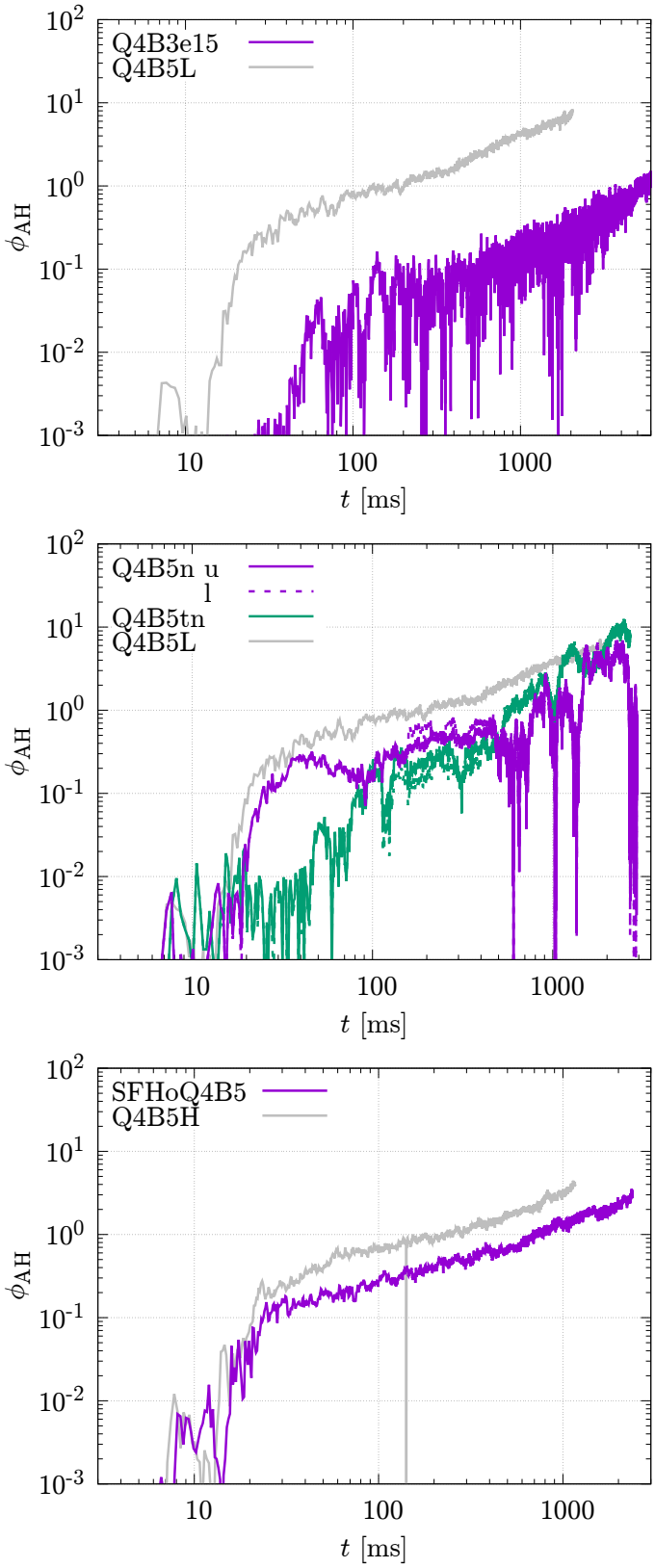

Figure 5.16: The time evolution of the MADness parameter for models Q4B3e15 (top panel), Q4B5n and Q4B5tn (middle panel), and SFHoQ4B5 (bottom panel). The results for models Q4B5L and Q4B5H of the previous chapter is also shown for comparison. The characters "u" and "l" represent the upper and lower hemispheres, respectively.

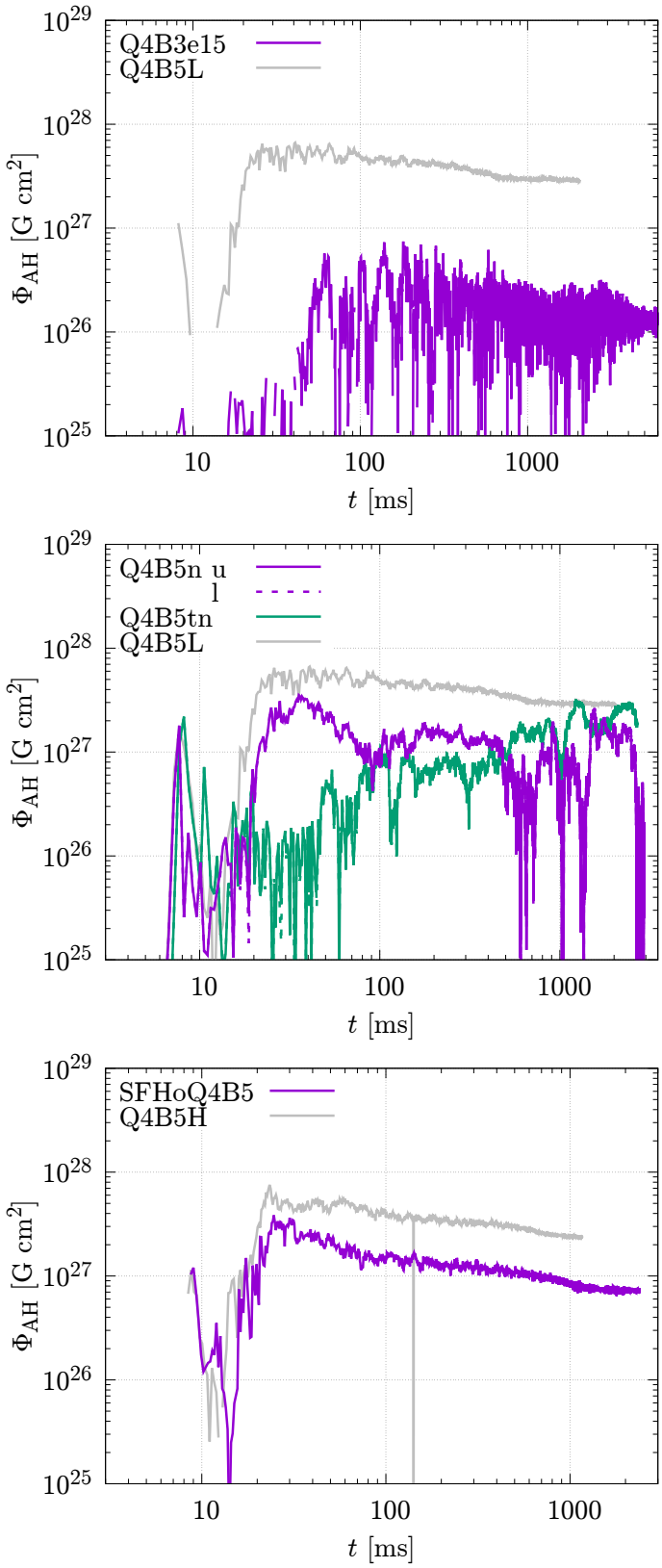

Figure 5.17: The same as Fig. 5.16 but for the time evolution of the magnetic flux evaluated on the apparent horizon.

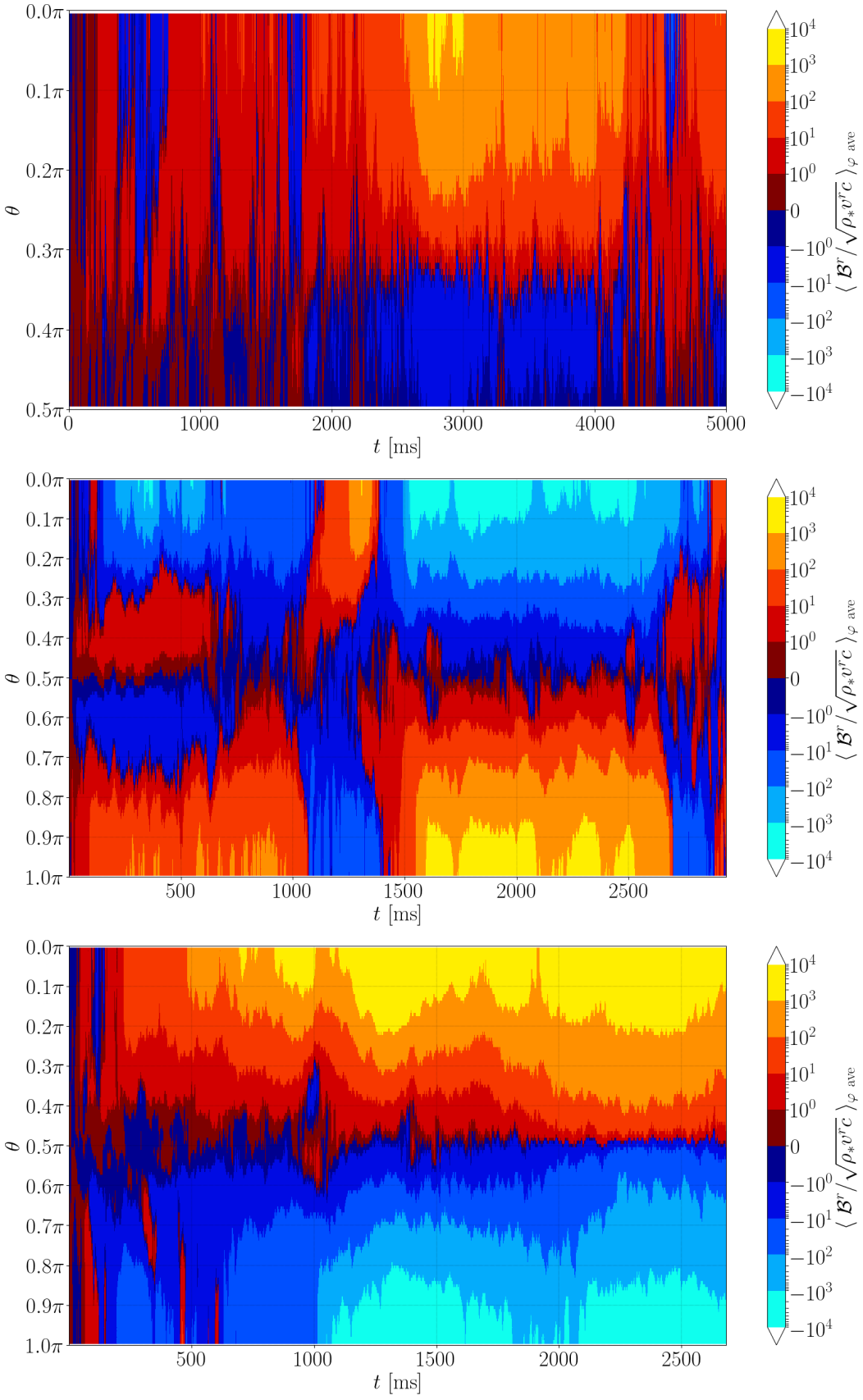

Figure 5.18: The profile of the local MADness parameter $\phi_{\rm AH,local}$ along the polar direction (θ) as a function of time for models Q4B3e15 (top panel), Q4B5n (middle), and Q4B5tn (bottom).

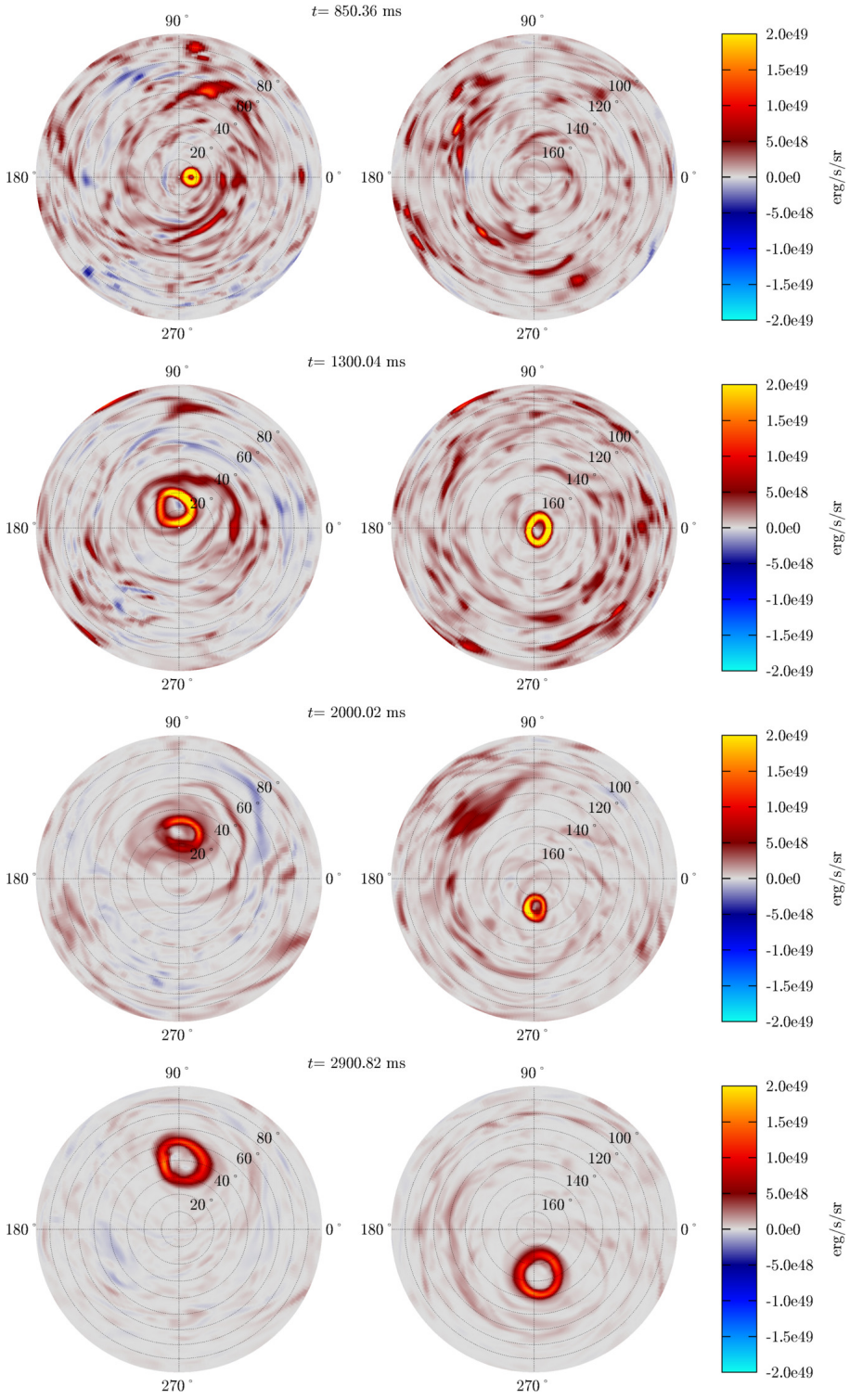

Figure 5.19: The angular distribution of the Poynting flux per steradian on a sphere of $r \approx 1500\,\mathrm{km}$ for model Q4B5tn at selected time slices. The left and right panels display the upper and lower hemispheres, respectively. The bright color displayed in the polar region stems from the Blandford-Znajek effect, while for other regions, the magnetic field accompanied by the outflowing matter contributes mainly to the Poynting flux. The region for which the Poynting flux is intense moves in the direction of the y-axis from the vicinity of the pole. At the same time, the opening angle of the Poynting flux gradually increases. See also the following link for the animation: `https://www2.yukawa.kyoto-u.ac.jp/~kota.hayashi/Q4B5tn-pf.mp4`.

and lower hemisphere of the apparent horizon are shown separately, although these two components approximately agree with each other. For most of the models, the magnetic flux on the apparent horizon reaches its peak in the timescale similar to that for achieving the equipartition in the accretion disk. Since $\Phi_{\rm AH}$ does not increase after the peak, the decrease of the accretion rate is the only path for the increase of the MADness parameter for such models. For model Q4B5tn, which initially has the toroidal magnetic field in the neutron star, $\Phi_{\rm AH}$ is low for the early post-merger stage ($t \lesssim 50$ ms) and it increases gradually in the entire simulation time. For this case, field lines starting from a point in each hemisphere always end in the same hemisphere for the early stage. However, due to the MRI turbulence and dynamo, the poloidal field is developed and subsequently penetrates the black-hole horizon, resulting in the increase of $\Phi_{\rm AH}$. By contrast, for the pure poloidal initial field, the black hole horizon is penetrated by the poloidal field from the early stage.

Because the MADness parameter defined on the entire horizon surface might not be a good indicator for assessing the launch of the strong Poynting flux, instead of it, we propose another parameter based on the local quantities. The point is that the magnetic-field lines that generate the strong Poynting flux do not penetrate the black-hole horizon in the vicinity of the equator, at which dense matter infalling from the accretion disk is always present and the (low-beta) magnetosphere is not formed. This suggests that focusing on the polar region on the apparent horizon for evaluating the MADness-like quantity would be a better strategy. Thus, we introduce a "local MADness parameter $\phi_{\rm AH,local}$", which is defined by

$$\phi_{\rm AH,local} := \frac{\mathcal{B}^r}{\sqrt{\rho_* v^r c}}. \tag{5.8}$$

Figure 5.18 shows the azimuthal-average value of the local MADness parameter $\phi_{\rm AH,local}$ as a function of time and polar angle θ for models Q4B3e15, Q4B5n, and Q4B5tn. For all the models, we find time intervals with $L_{\rm iso} \gtrsim 3 \times 10^{49}$ erg/s, and for such time intervals we always find $\phi_{\rm AH,local} \gtrsim 100$ at polar region of the apparent horizon. This suggests that the black hole has the ability to form a magnetosphere and launch a jet if the value of $\phi_{\rm AH,local}$ at the polar region exceeds 100, even if the value of $\phi_{\rm AH}$ is smaller than 50.

We note here that $\phi_{\rm AH,local}$ only gives us the necessary condition for the launch of a jet with high-Poynting luminosity. The disturbance or the deformation of the magnetosphere far from the horizon associated with the evolution of the accretion disk could result in a low value of $L_{\rm iso}$. For example the local MADness parameter exceeds 100 at $t \gtrsim 1700$ ms but $L_{\rm iso}$ falls below 10^{49} erg/s for Q4B5tn model. This is due to the deformation (tilt) of the magnetosphere induced by the post-merger mass ejection. The details of this behavior are given in the next subsection.

Focusing on the polarity, the local MADness parameter for model Q4B5n shows interesting behavior. As we already pointed out in this subsection, this model shows a clear butterfly structure of $b_{\bar{\varphi},\rm ave}$ extending to the polar region due to the flip of the magnetic-field polarity, and this flip occurs at the peaks of $L_{\rm iso}$. A similar flip is also observed for the local MADness parameter for $t = 1000$–1500 ms (see Fig. 5.18). Thus, we conclude that the complete flip of the magnetic-field polarity in the magnetosphere is the result of this polarity flip on the apparent horizon. Just like in the MRI dynamo and butterfly structure of $b_{\bar{\varphi},\rm ave}$ in the accretion disk, the polarity flip starts in the vicinity of the equatorial plane and propagates to the polar region. This is because the value of $\phi_{\rm AH,local}$ is lower than 10 near the equatorial plane and the fluid dynamics dominates over the magnetic-field dynamics. This feature enables the matter accretion from the disk to occasionally carry the magnetic field with opposite polarity. Then, the magnetic tower effect enhances the

magnetic-field strength along the polar direction. In this process, the preexisting magnetic field near the pole is dissipated away due to the reconnection by the magnetic field with opposite polarity ascending from the equatorial region, which replaces the polarity of the field penetrating the polar region of the horizon. Once the magnetic tower effect is in action, the magnetic field is amplified by the winding (associated with the black-hole spin) and the matter is pushed outward. As a result, a high-$\phi_{\rm AH,local}$ region is realized near the pole, where the magnetic-field strength is high and the rest-mass accretion rate is low. In the high-$\phi_{\rm AH,local}$ region, the magnetic-field dynamics dominates the fluid dynamics, and hence, the polarity flip cannot start in the polar region.

5.2.3 Time duration for high Poynting luminosity

The stage with a high value of $L_{\rm iso}$ continues for $\sim$ 400–2200 ms and subsequently start decreasing. This is particularly clear for models Q4B3e15, Q4B5n, and Q4B5tn. For these models, we confirmed that the value of $L_{\rm iso}$ decreases by nearly two orders of magnitude in the fading stage. This is consistent with the duration of the short-hard gamma-ray bursts, whose typical duration is ~ 1 s [14].

In the previous chapter, we discussed that the decrease of $L_{\rm iso}$ is due to the increase in the opening angle of the funnel region and the decrease of the magnetic-flux density in the magnetosphere. The opening angle of the strong Poynting-flux region increases from $\lesssim 10^\circ$ to $\sim 20^\circ$ and the intensity of the Poynting flux becomes low with time. This is directly related to the accretion disk evolution. The location of the funnel wall is determined by the balance between the gas pressure of the thick torus and the magnetic pressure at the funnel wall. In the seconds-long evolution of the torus (disk), the rest-mass density and the gas pressure at the funnel wall gradually decrease due to the post-merger mass ejection and matter accretion onto the black hole. On the other hand, the magnetic pressure in the magnetosphere and at the funnel wall does not decrease significantly, in particular for the late stage of the evolution. Thus the magnetic pressure can eventually exceed the gas pressure at the original position of the funnel wall, resulting in the gradual expansion of the funnel region. As discussed previously, this mechanism could be one of the ingredients that determine the time duration of short-hard gamma-ray bursts.

For the SFHoQ4B5 model, the opening angle also increases with time but with a longer timescale. As a result, we do not find the clear fading stage of $L_{\rm iso}$ for this model in our simulation time. Due to the high computational cost, we terminated the simulation at $t \sim 2500$ ms, but if we evolve the system longer, the fading stage is likely to be present.

From the results for models Q4B3e15, Q4B5n, and Q4B5tn, we find two additionally possible mechanisms for the fade-away of the Poynting luminosity, which could also explain the short time duration of short-hard gamma-ray bursts. For both mechanisms, the non-trivial evolution of the magnetosphere associated with the evolution of the accretion disk is essential.

For models Q4B3e15 and Q4B5n, in the very late stage of our simulation, the aligned magnetic field is dissipated away, and as a result, the magnetosphere with aligned magnetic fields disappears. Figure 5.15 shows that for $t \lesssim 1550$ ms the poloidal magnetic-field lines in the polar region are aligned and approximately directed to the direction of the black-hole spin axis (z-axis); i.e., a magnetosphere is present. In the magnetosphere, the magnetic-field lines are clearly helical and maintain the high-intensity Poynting flux. However, it is found that at $t \approx 2730$ ms the magnetic field in the polar region is not aligned anymore. Moreover, the magnetic-field dynamics cannot govern the fluid dynamics and the clear magnetosphere disappears. In the absence of the well-ordered magnetic field, the system cannot maintain the high-intensity Poynting flux.

Figure 5.14 shows that for model Q4B5n with $t \sim 1500$–2500 ms for which the high Poynting luminosity is maintained (see Fig. 5.13), the polarity of the poloidal magnetic field at the polar region remains to be preserved and does not reverse. However, for $t \gtrsim 2500$ ms, the Poynting luminosity decreases. For this late stage, the polarity in the polar region frequently reverses in response to the polarity reversal in the disk near the equatorial plane. The local MADness parameter in Fig. 5.18 also shows similar behavior. We interpret that the disappearance of the magnetosphere and the decrease of the Poynting flux stem from the MRI dynamo activity in the accretion disk. Due to the MRI dynamo activity, the polarity of the magnetic field in the accretion disk is reversed quasi-periodically and the magnetic flux continuously ascends toward the polar region from the equatorial region. If the magnetic field ascending from the disk has the polarity different from that in the magnetosphere and its field strength is high enough, the magnetic field that is originally located in the magnetosphere could be dissipated away by the magnetic-field reconnection. This is what is observed for $t \gtrsim 2500$ ms of model Q4B5n, and for $t \gtrsim 3000$ ms of Q4B3e15 model. If the strength of the ascending magnetic field is even stronger, then it could replace the polarity completely and reform the magnetosphere again. This is what is observed for $t \approx 1000$–1500 ms of model Q4B5n. However, we expect that the magnetosphere formation will not occur again after the disappearance of the strong magnetic fields for models Q4B3e15 and Q4B5n because as already discussed, the magnetic-field strength in the disk is determined by the rest-mass density (and thus internal energy density) achieved for the equipartition relation. Since the rest-mass density decreases as a result of the disk expansion, the post-merger mass ejection, and the mass accretion onto the black hole, the magnetic-field strength in the disk also decreases. Therefore, the revival of a magnetosphere with strong magnetic fields is not possible in the late stage of the disk. In the absence of strong magnetic fields, the Poynting luminosity is low because the Blandford-Znajek Poynting luminosity is proportional to the square of the magnetic-field strength [72].

Model Q4B5tn shows the second mechanism. In this mechanism, the magnetosphere still exists, but the Poynting luminosity becomes apparently low if we measure along a particular direction. The mechanism of this is the tilt of the accretion disk and magnetosphere. Figure 5.19 shows the angular distribution of the Poynting flux per steradian defined by $-T^r_t\sqrt{-g}/\sin\theta$ on a sphere of $r \approx 1500$ km for model Q4B5tn. For $t \lesssim 1300$ ms the strong Poynting-flux region is approximately aligned with the polar direction (z-axis direction). However, at $t \sim 2000$ ms the strong Poynting-flux region starts deviating from the polar region clearly, and at $t \approx 2900$ ms it is tilted by 25°–40° from the z-axis direction in the y-z plane. The isotropic-equivalent luminosity is defined by the integration for $0° < \theta < 10°$ and $170° < \theta < 180°$ on the upper and lower hemispheres, respectively, and thus, it decreases significantly by the tilt. We note here that the black-hole spin axis is aligned with the z-axis during the entire simulation time. As Fig. 5.2 shows, the system approximately has the equatorial-plane symmetry in the early stage of the post-merger evolution. However, later, the system loses the symmetry; the accretion disk misaligns with the equatorial plane and the major axis of the magnetosphere also deviates from the z-axis direction. This is due to the asymmetric nature of the post-merger mass ejection resulting from the turbulent state of the accretion disk. Specifically, in this model, the post-merger ejecta carries a large amount of the y-component of the angular momentum and this breaks the symmetry of the accretion disk. Indeed, the remnant accretion disk has the y-component of the angular momentum, and as a result, the system tilts in the y-z plane. [3]

[3] We note that the system is still capable of launching a jet to an off-axis direction. Indeed we still find

We find not only the tilt of the high Poynting-flux region, but also the widening of the opening angle in Fig. 5.19 like in the models of the previous chapter. For model Q4B5tn in Fig. 5.19, at $t \approx 850\,\mathrm{ms}$, the opening angle is $\lesssim 10^\circ$ but it increases to $\sim 30^\circ$ at $t \approx 2900\,\mathrm{ms}$. Thus, the intensity of the Poynting flux decreases simultaneously with tilting. This widening of the opening angle results from the decrease of the gas pressure at the funnel wall due to the post-merger mass ejection and matter accretion onto the black hole, as we already described.

We have found the two possible mechanisms for the decrease of the Poynting luminosity in addition to one mechanism that we already found in the previous chapter. For all the three mechanisms, the evolution of the accretion disk and the post-merger mass ejection are critical processes. Our results show that irrespective of the mechanisms, the timescale of $\sim 1\,\mathrm{s}$ for the high Poynting-luminosity stage is determined by the evolution timescale of the accretion disk, which is determined by the neutrino cooling and magnetohydrodynamics turbulence that control the post-merger mass ejection.

A word of caution is appropriate here. The system, specifically the accretion disk, is in a turbulent state by the MRI. That is, the evolution of the disk and MRI dynamo activity are determined by a stochastic process. This implies that we cannot precisely predict the strength of the magnetic field that penetrates the black hole and forms the magnetosphere and the angular momentum that is carried away by the post-merger ejecta. It is also not easy to predict whether the black hole will always be penetrated by the magnetic field strong enough to form a magnetosphere and launch the Poynting flux that can explain typical short-hard gamma-ray bursts. It is also not easy to predict by which mechanisms the high Poynting-luminosity stage is terminated. However, our simulation results show that once the magnetosphere is formed, its subsequent evolution is determined by the global properties of the post-merger ejecta and the accretion disk.

the strong Poynting-flux region even after $L_{\rm iso}$ (in our definition) drops.

Chapter 6

Summary

In this thesis, we summerise the entire evolution process of the black hole-neutron star merger starting from the inspiral stage, the merger stage through the post-merger stage. We performed general-relativistic neutrino-radiation magnetohydrodynamics simulations and evolved the black hole-accretion disk system remaining after the tidal disruption for $\sim$ 1–6 s in order to self-consistently explore the dynamical mass ejection, remnant disk evolution, post-merger mass ejection, and generation of collimated Poynting flux in the magnetosphere which may drive a short-hard gamma-ray burst. The mass of the black hole and the neutron star were chosen to be plausible values ($M_{\rm BH,0} = 5.4$ or $8.1 M_\odot$ and $M_{\rm NS} = 1.35 M_\odot$; cf. Ref [7]), and we prepare a rapidly spinning black hole ($\chi_{\rm BH} = 0.75$) to consider the case that the neutron star is tidally disrupted. Also, we preformed simulations in various setups focusing on the following five points: (1) Two different initial black hole mass $M_{\rm BH,0} = 5.4$ and $8.1 M_\odot$, which correspond to the mass ratio $Q = 4$ and 6, were adopted. (2) Three different initial maximum magnetic-field strengths ranging from 3×10^{15} G to 5×10^{16} G were assumed. (3) The poloidal and the toroidal magnetic fields were assumed for the initial magnetic-field configurations in the neutron star. (4) The simulations were performed with and without imposing the equatorial-plane symmetry. (5) DD2 EOS and the SFHo EOS were employed to model the neutron star.

We found, irrespective of the difference in the setups listed above, that the essential part of the merger and post-merger processes is qualitatively universal. First, dynamical mass ejection takes place right after the tidal disruption of the neutron star in the timescale of a few ms. Then the accretion disk is formed around the remnant black hole. In the accretion disk, the magnetic field is amplified by magnetohydrodynamics effects such as the MRI, winding, and Kelvin-Helmholtz instability. The MRI turbulence induces effective viscosity that enhances the angular-momentum transport. As a result, the mass accretion and the expansion of the disk are induced. The MRI dynamo is also activated and the polarity of the magnetic field is reversed quasi-periodically. In addition, a portion of the matter with the strong magnetic fields is outflowed vertically from the disk. This plays a role in the disk expansion to the vertical direction. In the turbulent process, thermal energy is generated, but in the first several hundred ms, the generated heat is dissipated primarily by the neutrino emission and it does not have a significant effect on the post-merger mass ejection.

We analyzed the ratio of the anisotropic stress to the pressure to evaluate the alpha viscous tensor, α_{ij}. It is found that all the components of α_{ij} have a value between 10^{-2} and 10^{-1} after the magnetic field amplification saturates and the disk settles into the equipartition state. However, the value of the $r\varphi$ or xy components of this tensor is larger than the other components. This reflects that not only the effective viscous effect but

also intrinsic magnetohydrodynamics effects play a role in the momentum transport. The large value of $\alpha_{r\varphi}$ suggests that a magnetohydrodynamics effect associated with global magnetic fields such as the magneto-centrifugal effects [119] play an important role in the angular momentum transport.

The disk expands gradually due to the angular momentum transport effects. As a result, the maximum temperature of the disk drops, and the neutrino luminosity drops. Then the neutrino emission cannot carry away an appreciable fraction of the thermal energy generated by the turbulent process from the disk, and the generated thermal energy induces the convective motion in the disk, which carries the thermal energy generated around the inner edge of the disk to the outer region. This convective motion contributes to the heating of the outer part of the disk, and eventually, induces the post-merger mass ejection.

There are two components in the electron fraction distribution for the ejected matter. One is a low-electron fraction component ($Y_{\rm e} < 0.1$) produced by the dynamical ejecta and the other is a mildly neutron-rich component ($0.1 \lesssim Y_{\rm e} \lesssim 0.4$) produced by the post-merger ejecta. Also, there are two components in the velocity distribution. One is a fast component (up to $v \sim 0.4c$) produced by the dynamical ejecta and the other is a relatively slow component ($v < 0.1c$) produced by the post-merger ejecta. These distributions are suitable for reproducing an elemental abundance pattern similar to the solar abundance and those of the metal-poor stars [127].

We found quantitative differences between the results for the models with low and high initial magnetic-field strengths. Because it takes a longer time to amplify the magnetic field up to saturation and to achieve an equipartition state in the disk from the low initial field strength (with a limited grid resolution), the evolution of the accretion disk and post-merger mass ejection are delayed. However, essentially no differences are found in the properties of the ejected matter.

Accompanying the turbulent disk formation, a funnel-shaped magnetosphere with the low rest-mass density and the aligned helical magnetic-field lines are formed near the rotation axis of the black hole. This magnetosphere is a magnetically dominated region and is in an approximate force-free state. The magnetic field lines that form the magnetosphere penetrate the black hole and it extracts the rotational kinetic energy of the rapidly spinning black hole by the Blandford-Znajeck mechanism [72]. Then, the collimated outgoing Poynting flux is generated with the opening angle of $\sim 10^\circ$, and its isotropic-equivalent luminosity is $\sim 10^{50}\,{\rm erg/s}$. The high Poynting luminosity stage continues for ~ 0.5–$2\,{\rm s}$, and the luminosity subsequently decreases. This timescale is determined mainly by the evolution of the accretion disk. These properties are consistent with typical short-hard gamma-ray bursts [14, 15].

We found three possible processes that could determine the time scale for the high Poynting luminosity stage. First, the Poynting luminosity is likely to drop due to the spreading of the funnel wall and the decrease of the magnetic-field strength. The spreading of the funnel wall is caused by the decrease of the gas pressure from the torus at the funnel wall which takes place due to the post-merger mass ejection. As the funnel wall spreads, the magnetosphere, the Poynting flux, and the magnetically driven outflow become less-collimated. Second, for the model with a low initial magnetic-field strength and the model with no equatorial-plane symmetry, the Poynting luminosity for a given observer drops due to the disappearance of the magnetosphere stemming from the reconnection of the magnetic-field lines. This is caused by the MRI dynamo activity in the accretion disk, which enforces the magnetic flux with a variety of the polarity to be ejected quasi-periodically from the disk to the polar region. When strong magnetic fields with the

polarity opposite to that in the magnetosphere emerge from the disk, they pair-annihilate by the reconnection, and the magnetosphere temporarily disappears. If the magnetic field emerging from the disk is strong enough by any chance, it replaces the magnetic field in the magnetosphere. However, this replacement is only found in the model with no equatorial-plane symmetry, and the disappearance occurs for the models with low initial magnetic-field strength and the model with no equatorial-plane symmetry. Third, for the model with the initially toroidal magnetic field in the neutron star, the Poynting luminosity drops due to the tilt of the magnetosphere. Because the post-merger ejecta occasionally carries the angular momentum component not parallel to the black hole spin axis, the accretion disk is enforced to tilt, in particular in the late-time evolution. Then, it results in the tilt of the magnetosphere because the funnel structure of the magnetosphere is determined by the gas pressure from the disk (torus). Irrespective of these mechanisms, the evolution process of the accretion disk does determine the evolution process of the magnetosphere. These three mechanisms all include stochastic processes, and it is not feasible to precisely predict which mechanisms determine the evolution process of the magnetosphere. However, these three could be plausible mechanisms to make short-hard gamma-ray bursts as short as ~ 0.5–$2\,$s.

From a quantitative point of view, the dynamical ejecta mass for present models were $\approx 0.046 M_\odot$ (DD2 $Q = 4$ models), $\approx 0.038 M_\odot$ (DD2 $Q = 6$ models), and $\approx 0.014 M_\odot$ (SFHo $Q = 4$ model). The disk mass right after its formation was $M_{\rm disk,0} \approx 0.28 M_\odot$ (DD2 $Q = 4$ models), $\approx 0.18 M_\odot$ (DD2 $Q = 6$ models), and $\approx 0.22 M_\odot$ (SFHo $Q = 4$ model). The post-merger mass ejection sets in as the maximum disk temperature and neutrino luminosity drop below $\sim 3\,$Mev, and $\sim 10^{51}$–$10^{51.5}\,$erg/s, respectively. The mass of the post-merger ejecta was $\gtrsim 0.030 M_\odot$ (DD2 $Q = 4$ model), $\gtrsim 0.020 M_\odot$ (DD2 $Q = 4$ model), and $\gtrsim 0.018 M_\odot$ (SFHo $Q = 4$ model), which are $\sim 10\%$ of $M_{\rm disk,0}$. We note, however, that we have only done simulations for the three physical models. The quantitative dependence of the evolution, especially of the post-merger evolution, on the binary mass, the black-hole spin, and the neutron star EOS is yet to be discovered. If the remnant disk mass is larger, the post-merger ejecta mass could be larger. Also, the Poynting luminosity could be higher because the magnetic field could be amplified stronger in the equipartition state with higher rest-mass density. In contrast, Poynting luminosity would become lower or even the magnetosphere may not be formed if the spin of the black hole is smaller. The quantitative aspects is an issue to be explored in future studies.

Acknowledgements

First, I would like to express my deepest gratitude to my supervisor Professor Masaru Shibata for fruitful discussions and continuous support throughout my Ph.D. journey. I am also grateful to him for providing me with plentiful computational resources. I also would like to thank Professor Kenta Kiuchi and Professor Yuichiro Sekiguchi for developing the code used in this work and for teaching the physical and numerical aspects of numerical-relativity simulations in detail. I am grateful to Professor Koutaro Kyutoku for computing the initial data simulations and for discussions. I am grateful to Dr. Sho Fujibayashi and Dr. Kyohei Kawaguchi for discussions and collaboration. I thank former and current members of Yukawa Institute of Theoretical Physics and Theoretical Astrophysics group at Kyoto University, especially Professor Kunihito Ioka, Dr. Wataru Ishizaki, Dr. Kazuya Takahashi, Dr. Hamid Hamidani, and Dr. Tomoki Wada for discussions on high-energy astrophysics. I also thank Mr. Kazutaka Kimura, Mr. Hidetoshi Omiya, and Mr. Taisuke Matsuda for daily discussions on a wide range of astrophysics.

Bibliography

[1] B. P. Abbott et al., Phys. Rev. Lett. **116**, 061102 (2016).

[2] R. Abbott et al., Phys. Rev. X **11**, 021053 (2021).

[3] R. Abbott et al., (2021), arXiv:2111.03606 [gr-qc].

[4] B. P. Abbott et al., Phys. Rev. Lett. **119**, 161101 (2017).

[5] B. P. Abbott et al., Astrophys. J. **848**, L12 (2017).

[6] B. P. Abbott et al., Astrophys. J. **848**, L13 (2017).

[7] R. Abbott et al., Astrophys. J. **915**, L5 (2021).

[8] M. Shibata, *Numerical relativity*, Vol. 1 (World Scientific, 2015).

[9] K. Kyutoku, M. Shibata, and K. Taniguchi, Living Rev. Rel. **24**, 5 (2021).

[10] J. M. Lattimer and D. N. Schramm, Astrophys. J. Lett. **192**, L145 (1974).

[11] D. Eichler, M. Livio, T. Piran, and D. N. Schramm, **340**, 126 (1989).

[12] L.-X. Li and B. Paczyński, Astrophys. J. **507**, L59 (1998).

[13] B. D. Metzger, G. Martínez-Pinedo, S. Darbha, E. Quataert, A. Arcones, D. Kasen, R. Thomas, P. Nugent, I. V. Panov, and N. T. Zinner, Mon. Not. R. Astron. Soc. **406**, 2650 (2010).

[14] E. Nakar, Phys. Rep. **442**, The Hans Bethe Centennial Volume 1906-2006, 166 (2007).

[15] E. Berger, Annu. Rev. Astron. Astrophys. **52**, 43 (2014).

[16] B. Paczynski, Acra Astron. **41**, 257 (1991).

[17] B. P. Abbott et al., Living Rev. Rel. **23**, 3 (2020).

[18] J. P. Gardner et al., Space Sci. Rev. **123**, 485 (2006).

[19] Ž. Ivezić et al., Astrophys. J. **873**, 111, 111 (2019).

[20] M. Shibata and K. Uryū, Phys. Rev. D **74**, 121503 (2006).

[21] M. Shibata and K. Uryū, Classical Quantum Gravity **24**, S125 (2007).

[22] M. Shibata and K. Taniguchi, Phys. Rev. D **77**, 084015 (2008).

[23] Z. B. Etienne, J. A. Faber, Y. T. Liu, S. L. Shapiro, K. Taniguchi, and T. W. Baumgarte, Phys. Rev. D **77**, 084002 (2008).

[24] M. D. Duez, F. Foucart, L. E. Kidder, H. P. Pfeiffer, M. A. Scheel, and S. A. Teukolsky, Phys. Rev. D **78**, 104015 (2008).

[25] M. Shibata, K. Kyutoku, T. Yamamoto, and K. Taniguchi, Phys. Rev. D **79**, 044030 (2009).

[26] Z. B. Etienne, Y. T. Liu, S. L. Shapiro, and T. W. Baumgarte, Phys. Rev. D **79**, 044024 (2009).

[27] S. Chawla, M. Anderson, M. Besselman, L. Lehner, S. L. Liebling, P. M. Motl, and D. Neilsen, Phys. Rev. Lett. **105**, 111101 (2010).

[28] M. D. Duez, F. Foucart, L. E. Kidder, C. D. Ott, and S. A. Teukolsky, Classical Quantum Gravity **27**, 114106 (2010).

[29] K. Kyutoku, M. Shibata, and K. Taniguchi, Phys. Rev. D **82**, 044049 (2010).

[30] K. Kyutoku, H. Okawa, M. Shibata, and K. Taniguchi, Phys. Rev. D **84**, 064018 (2011).

[31] F. Foucart, M. D. Duez, L. E. Kidder, and S. A. Teukolsky, Phys. Rev. D **83**, 024005 (2011).

[32] F. Foucart, M. D. Duez, L. E. Kidder, M. A. Scheel, B. Szilagyi, and S. A. Teukolsky, Phys. Rev. D **85**, 044015 (2012).

[33] Z. B. Etienne, Y. T. Liu, V. Paschalidis, and S. L. Shapiro, Phys. Rev. D **85**, 064029 (2012).

[34] Z. B. Etienne, V. Paschalidis, and S. L. Shapiro, Phys. Rev. D **86**, 084026 (2012).

[35] K. Kyutoku, K. Ioka, and M. Shibata, Phys. Rev. D **88**, 041503 (2013).

[36] K. Kyutoku, K. Ioka, H. Okawa, M. Shibata, and K. Taniguchi, Phys. Rev. D **92**, 044028 (2015).

[37] F. Foucart, M. B. Deaton, M. D. Duez, L. E. Kidder, I. MacDonald, C. D. Ott, H. P. Pfeiffer, M. A. Scheel, B. Szilagyi, and S. A. Teukolsky, Phys. Rev. D **87**, 084006 (2013).

[38] G. Lovelace, M. D. Duez, F. Foucart, L. E. Kidder, H. P. Pfeiffer, M. A. Scheel, and B. Szilágyi, Classical Quantum Gravity **30**, 135004 (2013).

[39] M. B. Deaton, M. D. Duez, F. Foucart, E. O'Connor, C. D. Ott, L. E. Kidder, C. D. Muhlberger, M. A. Scheel, and B. Szilagyi, Astrophys. J. **776**, 47 (2013).

[40] F. Foucart, M. B. Deaton, M. D. Duez, E. O'Connor, C. D. Ott, R. Haas, L. E. Kidder, H. P. Pfeiffer, M. A. Scheel, and B. Szilagyi, Phys. Rev. D **90**, 024026 (2014).

[41] V. Paschalidis, M. Ruiz, and S. L. Shapiro, Astrophys. J. **806**, L14 (2015).

[42] K. Kawaguchi, K. Kyutoku, H. Nakano, H. Okawa, M. Shibata, and K. Taniguchi, Phys. Rev. D **92**, 024014 (2015).

[43] K. Kiuchi, Y. Sekiguchi, K. Kyutoku, M. Shibata, K. Taniguchi, and T. Wada, Phys. Rev. D **92**, 064034 (2015).

[44] F Foucart, D Desai, W Brege, M. D. Duez, D Kasen, D. A. Hemberger, L. E. Kidder, H. P. Pfeiffer, and M. A. Scheel, Classical Quantum Gravity **34**, 044002 (2017).

[45] K. Kyutoku, K. Kiuchi, Y. Sekiguchi, M. Shibata, and K. Taniguchi, Phys. Rev. D **97**, 023009 (2018).

[46] W. Brege, M. D. Duez, F. Foucart, M. B. Deaton, J. Caro, D. A. Hemberger, L. E. Kidder, E. O'Connor, H. P. Pfeiffer, and M. A. Scheel, Phys. Rev. D **98**, 063009 (2018).

[47] M. Ruiz, S. L. Shapiro, and A. Tsokaros, Phys. Rev. D **98**, 123017 (2018).

[48] F. Foucart, M. D. Duez, T. Hinderer, J. Caro, A. R. Williamson, M. Boyle, A. Buonanno, R. Haas, D. A. Hemberger, L. E. Kidder, H. P. Pfeiffer, and M. A. Scheel, Phys. Rev. D **99**, 044008 (2019).

[49] F. Foucart, M. D. Duez, L. E. Kidder, S. M. Nissanke, H. P. Pfeiffer, and M. A. Scheel, Phys. Rev. D **99**, 103025 (2019).

[50] T. Hinderer, S. Nissanke, F. Foucart, K. Hotokezaka, T. Vincent, M. Kasliwal, P. Schmidt, A. R. Williamson, D. A. Nichols, M. D. Duez, L. E. Kidder, H. P. Pfeiffer, and M. A. Scheel, Phys. Rev. D **100**, 063021 (2019).

[51] K. Hayashi, K. Kawaguchi, K. Kiuchi, K. Kyutoku, and M. Shibata, Phys. Rev. D **103**, 043007 (2021).

[52] F. Foucart, A. Chernoglazov, M. Boyle, T. Hinderer, M. Miller, J. Moxon, M. A. Scheel, N. Deppe, M. D. Duez, F. Hébert, L. E. Kidder, W. Throwe, and H. P. Pfeiffer, Phys. Rev. D **103**, 064007 (2021).

[53] E. R. Most, L. J. Papenfort, S. D. Tootle, and L. Rezzolla, Astrophys. J. **912**, 80, 80 (2021).

[54] S. V. Chaurasia, T. Dietrich, and S. Rosswog, Phys. Rev. D **104**, 084010 (2021).

[55] E. R. Most, L. J. Papenfort, S. D. Tootle, and L. Rezzolla, Mon. Not. R. Astron. Soc. **506**, 3511 (2021).

[56] R. Fernández and B. D. Metzger, Mon. Not. R. Astron. Soc. **435**, 502 (2013).

[57] B. D. Metzger and R. Fernández, Mon. Not. R. Astron. Soc. **441**, 3444 (2014).

[58] O. Just, A. Bauswein, R. A. Pulpillo, S. Goriely, and H.-T. Janka, Mon. Not. R. Astron. Soc. **448**, 541 (2015).

[59] R. Fernández, E. Quataert, J. Schwab, D. Kasen, and S. Rosswog, Mon. Not. R. Astron. Soc. **449**, 390 (2015).

[60] R. Fernández, F. Foucart, D. Kasen, J. Lippuner, D. Desai, and L. F. Roberts, Classical Quantum Gravity **34**, 154001 (2017).

[61] D. M. Siegel and B. D. Metzger, Astrophys. J. **858**, 52 (2018).

[62] R. Fernández, A. Tchekhovskoy, E. Quataert, F. Foucart, and D. Kasen, Mon. Not. R. Astron. Soc. **482**, 3373 (2019).

[63] A. Janiuk, Astrophys. J. **882**, 163 (2019).

[64] I. M. Christie, A Lalakos, A Tchekhovskoy, R Fernández, F Foucart, E Quataert, and D Kasen, Mon. Not. R. Astron. Soc. **490**, 4811 (2019).

[65] J. M. Miller, B. R. Ryan, J. C. Dolence, A. Burrows, C. J. Fontes, C. L. Fryer, O. Korobkin, J. Lippuner, M. R. Mumpower, and R. T. Wollaeger, Phys. Rev. D **100**, 023008 (2019).

[66] S. Fujibayashi, M. Shibata, S. Wanajo, K. Kiuchi, K. Kyutoku, and Y. Sekiguchi, Phys. Rev. D **101**, 083029 (2020).

[67] S. Fujibayashi, M. Shibata, S. Wanajo, K. Kiuchi, K. Kyutoku, and Y. Sekiguchi, Phys. Rev. D **102**, 123014 (2020).

[68] X. Li and D. M. Siegel, Phys. Rev. Lett. **126**, 251101 (2021).

[69] R. Fernández, F. Foucart, and J. Lippuner, Mon. Not. R. Astron. Soc. **497**, 3221 (2020).

[70] O. Just, S. Goriely, H. T. Janka, S. Nagataki, and A. Bauswein, Mon. Not. R. Astron. Soc. **509**, 1377 (2022).

[71] M. Shibata, S. Fujibayashi, and Y. Sekiguchi, Phys. Rev. D **104**, 063026 (2021).

[72] R. D. Blandford and R. L. Znajek, Mon. Not. R. Astron. Soc. **179**, 433 (1977).

[73] M. Shibata and K. Taniguchi, Living Rev. Relativity **14**, 6 (2011).

[74] K. Taniguchi, T. W. Baumgarte, J. A. Faber, and S. L. Shapiro, Physical Review D **77**, `10.1103/physrevd.77.044003` (2008).

[75] S. A. Balbus and J. F. Hawley, Astrophys. J. **376**, 214 (1991).

[76] S. A. Balbus and J. F. Hawley, Rev. Mod. Phys. **70**, 1 (1998).

[77] N. Shakura and R. Sunyaev, Astron. Astrophys. **24**, 337 (1973).

[78] A. Tchekhovskoy, R. Narayan, and J. C. McKinney, Mon. Not. R. Astron. Soc. **418**, L79 (2011).

[79] M Liska, A Tchekhovskoy, and E Quataert, Mon. Not. R. Astron. Soc. **494**, 3656 (2020).

[80] M. Shibata and T. Nakamura, Phys. Rev. D **52**, 5428 (1995).

[81] T. W. Baumgarte and S. L. Shapiro, Phys. Rev. D **59**, 024007 (1998).

[82] M. Campanelli, C. O. Lousto, P. Marronetti, and Y. Zlochower, Phys. Rev. Lett. **96**, 111101 (2006).

[83] J. G. Baker, J. Centrella, D.-I. Choi, M. Koppitz, and J. van Meter, Phys. Rev. Lett. **96**, 111102 (2006).

[84] P. Marronetti, W. Tichy, B. Brügmann, J. González, and U. Sperhake, Phys. Rev. D **77**, 064010 (2008).

[85] D. Hilditch, S. Bernuzzi, M. Thierfelder, Z. Cao, W. Tichy, and B. Brügmann, Phys. Rev. D **88**, 084057 (2013).

[86] C. Bona, J. Massó, E. Seidel, and J. Stela, Phys. Rev. Lett. **75**, 600 (1995).

[87] M. Alcubierre and B. Brügmann, Phys. Rev. D **63**, 104006, 104006 (2001).

[88] M. Shibata, Astrophys. J. **595**, 992 (2003).

[89] M. Shibata and Y.-i. Sekiguchi, Phys. Rev. D **72**, 044014 (2005).

[90] M. Shibata, Y.-i. Sekiguchi, and R. Takahashi, Prog. Theor. Phys. **118**, 257 (2007).

[91] K. Kiuchi, K. Kyutoku, and M. Shibata, Phys. Rev. D **86**, 064008 (2012).

[92] C. R. Evans and J. F. Hawley, Astrophys. J. **332**, 659 (1988).

[93] D. S. Balsara, J. Comput. Phys. **228**, 5040 (2009).

[94] A. Kurganov and E. Tadmor, Journal of Computational Physics **160**, 241 (2000).

[95] A. M. Anile, *Relativistic Fluids and Magneto-fluids* (1990).

[96] C. F. Gammie, J. C. McKinney, and G. Tóth, Astrophys. J. **589**, 444 (2003).

[97] L. Del Zanna, N. Bucciantini, and P. Londrillo, Astron. Astrophys. **400**, 397 (2003).

[98] Y. Sekiguchi, K. Kiuchi, K. Kyutoku, and M. Shibata, Prog. Theor. Exp. Phys. **2012**, 01A304 (2012).

[99] K. S. Thorne, Mon. Not. R. Astron. Soc. **194**, 439 (1981).

[100] M. Shibata, K. Kiuchi, Y.-i. Sekiguchi, and Y. Suwa, Prog. Theor. Phys. **125**, 1255 (2011).

[101] S. Fujibayashi, S. Wanajo, K. Kiuchi, K. Kyutoku, Y. Sekiguchi, and M. Shibata, Astrophys. J. **901**, 122 (2020).

[102] C. D. Levermore, **31**, 149 (1984).

[103] M. González, E. Audit, and P. Huynh, Astron. Astrophys. **464**, 429 (2007).

[104] S. Banik, M. Hempel, and D. Bandyopadhyay, Astrophys. J. **214**, 22 (2014).

[105] A. W. Steiner, M. Hempel, and T. Fischer, Astrophys. J. **774**, 17, 17 (2013).

[106] F. X. Timmes and F. D. Swesty, Astrophys. J. **126**, 501 (2000).

[107] M. C. Miller, F. K. Lamb, A. J. Dittmann, S. Bogdanov, Z. Arzoumanian, K. C. Gendreau, S. Guillot, A. K. Harding, W. C. G. Ho, J. M. Lattimer, R. M. Ludlam, S. Mahmoodifar, S. M. Morsink, P. S. Ray, T. E. Strohmayer, K. S. Wood, T. Enoto, R. Foster, T. Okajima, G. Prigozhin, and Y. Soong, Astrophys. J. Lett. **887**, L24, L24 (2019).

[108] S. Rosswog and M. Liebendörfer, Mon. Not. R. Astron. Soc. **342**, 673 (2003).

[109] G. M. Fuller, W. A. Fowler, and M. J. Newman, Astrophys. J. **293**, 1 (1985).

[110] J. Cooperstein, L. J. van den Horn, and E. A. Baron, Astrophys. J. **309**, 653 (1986).

[111] M. Ruffert, H. T. Janka, and G. Schaefer, Astron. Astrophys. **311**, 532 (1996).

[112] M. Ruffert and H. T. Janka, Astron. Astrophys. **380**, 544 (2001).

[113] A. Burrows, S. Reddy, and T. A. Thompson, Nucl. Phys. A **777**, 356 (2006).

[114] S. Fujibayashi, Y. Sekiguchi, K. Kiuchi, and M. Shibata, Astrophys. J. **846**, 114, 114 (2017).

[115] Y. Sekiguchi, Classical and Quantum Gravity **27**, 114107, 114107 (2010).

[116] Y. Masada and T. Sano, Astrophys. J. **689**, 1234 (2008).

[117] J. Guilet, A. Bauswein, O. Just, and H.-T. Janka, Mon. Not. R. Astron. Soc. **471**, 1879 (2017).

[118] A. Brandenburg and K. Subramanian, Phys. Rep. **417**, 1 (2005).

[119] R. D. Blandford and D. G. Payne, Mon. Not. R. Astron. Soc. **199**, 883 (1982).

[120] B. D. Metzger, A. L. Piro, and E. Quataert, Mon. Not. R. Astron. Soc. **390**, 781 (2008).

[121] K. Kyutoku, M. Shibata, and K. Taniguchi, Living Rev. Relativity **24**, 5, 5 (2021).

[122] M. Shibata, Y. T. Liu, S. L. Shapiro, and B. C. Stephens, Phys. Rev. D **74**, 104026 (2006).

[123] J. M. Bardeen, W. H. Press, and S. A. Teukolsky, Astrophys. J. **178**, 347 (1972).

[124] A. M. Beloborodov, Astrophys. J. **588**, 931 (2003).

[125] K. Hotokezaka, K. Kiuchi, K. Kyutoku, H. Okawa, Y.-i. Sekiguchi, M. Shibata, and K. Taniguchi, Phys. Rev. D **87**, 024001 (2013).

[126] S. Fujibayashi, K. Kiuchi, S. Wanajo, K. Kyutoku, Y. Sekiguchi, and M. Shibata, arXiv:2205.05557 [astro-ph.HE].

[127] S. Wanajo, S. Fujibayashi, K. Hayashi, K. Kiuchi, Y. Sekiguchi, and M. Shibata, arXiv:2212.04507 [astro-ph.HE].

[128] K. Kawaguchi, M. Shibata, and M. Tanaka, Astrophys. J. **889**, 171 (2020).